Aalto University
School of Chemical
Engineering

Juho Heiska

ORGANIC LITHIUM SALTS DEPOSITED WITH ALD FOR SUSTAINABLE MICROBATTERIES

Master´s Programme in Chemical, Biochemical and Materials Engineering

Major in Chemistry

Master's thesis for the degree of Master of Science in Technology submitted for inspection, Espoo, 10 May, 2017.

Supervisor Academy Professor Maarit Karppinen

Instructor M.Sc. (Tech.) Mikko Nisula

Aalto University
School of Chemical
Engineering

Aalto University, P.O. BOX 11000, 00076 AALTO
www.aalto.fi

Abstract of master's thesis

Author Juho Heiska

Title of thesis Organic Lithium Salts Deposited with ALD for Sustainable Microbatteries

Department Department of Chemistry

Major Chemistry

Thesis supervisor Professor Maarit Karppinen

Thesis advisor(s) / Thesis examiner(s) M.Sc. (Tech.) Mikko Nisula

Date 10.05.2017 **Number of pages** 100 **Language** English

Lithium ion batteries are already an established technology and is widely used in microbatteries. The dimensions of the devices that utilize microbatteries have shrunk, while the power requirement has remained constant. Moving from 2D to 3D architectures is a viable way of increasing the capacity per area. A major problem with 3D architectures is the fabrication of pinhole free and uniform layers of active material. One solution is to use precise deposition techniques such as atomic layer deposition (ALD).

Organic electrode materials are an interesting alternative to the inorganic electrode materials due to their high gravimetric and power density values. They can also be produced from abundant and sustainable resources. The structural diversity of the organic materials is immense and even small modifications change their chemical and electrochemical properties. The redox potential of organic electrode materials can be affected by adding an electron donating or withdrawing functional group.

In this work, five different organic precursors 2-aminoterephtalic acid (TPA2A), 2-bromoterephtalic acid (TPABr), 2,5-dihydroxylterephtalic acid (TPA25OH), 2,5-pyridinecaboxylic acid (PDC25), and 3,5-pyridinecaboxylic acid (PDC35) were employed as the organic ALD precursors. The inorganic precursor was LiTHD (THD = 2,2,6,6-tetramethyl-3,5-heptanedione). The deposited thin films were characterized with X-ray reflectivity (XRR), grazing incidence X-ray diffraction (GIXRD), and Fourier transform infrared spectroscopy (FTIR). The electrochemical properties of the thin films were evaluated with cyclic voltammetry (CV) and galvanostactic cycling from a half cell containing metallic lithium counter electrode.

Out of the deposited materials, the films Li_2TP2A, Li_2TP25OH, and Li_2PDC35, were crystalline, while Li_2PDC25, and Li_2TPBr were amorphous as confirmed by GIXRD. The saturation of the growth was confirmed for Li_2TP2A with XRR, while the growth linearity and ALD temperature window was examined quantitatively. The functional groups present in the molecules are not lithiated during the deposition. The electrochemical measurements revealed that the average redox potential was increased for electron withdrawing groups and decreased for electron donating groups. The change in potential was fairly moderate. The Li_2TPBr films out performed other films to some extent, in respect to cycling capabilities and the effect on the redox potential.

Keywords ALD, MLD, lithium ion battery, microbattery, organic electrode, organic lithium salt

Aalto-yliopisto
Kemian tekniikan
korkeakoulu

Aalto-yliopisto, PL 11000, 00076 AALTO
www.aalto.fi
Diplomityön tiivistelmä

Tekijä Juho Heiska

Työn nimi Orgaanisten litium suolojen atomikerroskasvatus ja niiden käyttö mikroakuissa

Laitos Kemian laitos

Pääaine Kemia

Työn valvoja Professori Maarit Karppinen

Työn ohjaaja(t)/Työn tarkastaja(t) DI Mikko Nisula

Päivämäärä 10.05.2017 **Sivumäärä** 100 **Kieli** Englanti

Litiumioniakku on jo pitkään käytössä ollut teknologia ja se on yleisesti käytössä mikroakuissa. Laitteiden mitat ovat kuitenkin pienentyneet nopeasti, vaikka niiden virrankulutus onkin pysynyt lähes vakiona. Kun 2D-arkkitehtuureista vaihdetaan kolmiulotteisiin arkkitehtuureihin, akkujen kapasiteetti kasvaa jokaista pinta-alayksikköä kohden. 3D-arkkitehtuurien suurin ongelma on tasaisten ja reiättömien akkukomponentti kerrosten valmistaminen. Eräs vaihtoehto on käyttää kalvojen kasvatusmenetelmiä kuten atomikerroskasvatusta (ALD).

Orgaaniset elektrodimateriaalit ovat mielenkiintoinen vaihtoehto epäorgaanisille elektrodimateriaaleille, koska niiden gravimetrinen kapasiteetti ja tehon tiheys ovat teoriassa hyvin korkeat. Lisäksi ne voidaan valmistaa uusiutuvista ja ekologisesti kestävistä materiaaleista. Orgaanisten elektrodimateriaalien rakenteellinen monimuotoisuus on valtava ja jopa pienet muutokset vaikuttavat kemiallisiin ja sähkökemiallisiin ominaisuuksiin merkittävästi. Näiden materiaalien hapetus-pelkistyspotentiaalia (redoxpotentiaali) voidaan kasvattaa tai pienentää lisäämällä molekyyliin funktionaalinen ryhmä, joka on elektroneja luovuttava tai vastaanottava ryhmä.

Tässä työssä viittä erilaista orgaanista lähtöainetta 2-amino tereftalaattihappo (TPA2A), 2-bromi tereftalaattihappo (TPABr), 2,5-dihydroxi tereftalaattihappo (TPA25OH) ja 2,5-pyridiinikarboksyylihappo (PDC25) ja 3,5-pyridiinikarboksyylihappo (PDC35), käytettiin lähtöaineina ALD-reaktorissa LiTHD:n (THD = 2,2,6,6-tetrametyyli-3,5-heptadioni) kanssa. Kasvatettuja ohutkalvoja tutkittiin röntgenheijastuksen (XRR), alhaisen tulokulman röntgendiffraktion (GIXRD) ja Fourier-muunnos infrapunaspektrometrian avulla. Kalvojen sähkökemiallisia ominaisuuksia tutkittiin syklisen voltammetrian ja purku-lataussyklien avulla.

GIXRD mittauksista selvisi, että ohut kalvoista Li_2TP2A, Li_2TP25OH ja Li_2PDC35 olivat kiteisiä ja Li_2PDC25 ja Li_2TPBr amorfisia. Kasvun saturoituminen Li_2TP2A:n kohdalla todistettiin XRR-laitteella. Kasvun lineaarisuutta ja lämpötilariippuvuutta tutkittiin kvalitatiivisesti. Litiumin ja karboksyylihapon muodostama kompleksi todettiin olevan silloittunut. Funktionaaliset ryhmät eivät myöskään reagoineet litiumin kanssa ALD-reaktorissa. Sähkökemiallisista mittauksista nähtiin, että elektroneja luovuttavat ryhmät laskevat redoxpotentiaalia, kun taas vastaanottavat ryhmät kasvattavat redoxpotentiaalia. Potentiaalin muutos oli kuitenkin hillitty. Tutkimusten perusteella bromia sisältäneet kalvot olivat näistä materiaaleista lupaavimpia, sillä niiden syklinen kestävyys ja bromin vaikutus redoxpotentiaaliin oli suurin.

Avainsanat ALD, MLD, litiumioniakku, mikroakku, orgaaninen elektrodi, orgaaninen litiumsuola

PREFACE

The experimental research of this thesis was carried out at the Laboratory of Inorganic Chemistry at Aalto University School of Chemical Technology between June 2016 and December 2016.

In the first instance, I want to express my gratitude for my supervisor Academy Professor Maarit Karppinen for giving me this opportunity and trusting in me. In addition, I want to thank my instructor M.Sc. Mikko Nisula, for the guidance along my long journey, and every time I had any trouble brewing. I am grateful to Taneli Tiittanen for helping me with UV-VIS spectroscopy and OriginLab. I also wish to acknowledge Professor Antti Karttunen for the USPEX calculations and Dr. Chris Thomas for the help with the FTIR sample preparation. Moreover, I wish to praise the whole group of Inorganic Chemistry for the overall positive work environment, for the events, and for the definitely not the pea soup Thursday.

Furthermore, I want to thank my lovely wife Maaria for standing beside me, believing in me, understanding my late and early hours, and keeping me hydrated and fed. A special bit of gratitude goes to my parents and family, for always being there for me. Finally, a well-deserved gratitude also goes to my friends for the continuous support during my studies.

Do. Or do not. There is no try.

Espoo 10th of May, 2017

Juho Heiska

TABLE OF CONTENTS

Symbols and Abbreviations

List of symbols

α	Adsorption coefficient
A	Area
Z	Atomic number
N_A	Avogadro constant
θ_c	Critical angle
I	Current
r_e	Electron radius
T_g	Glass transition temperature
σ	Ionic conductivity
P_m	Mass density
P_e	Mean electron density
n	Molar ratio
P	Power
R	Reflectance
$D_{seperator}$	Separator thickness
λ	Wavelength
V	Voltage

List of Abbreviations

AFM	Atomic force microscope
ALD	Atomic layer deposition
AQ	Anthraquinone
BMMI	1-N-butyl-2,3-dimethylimidazolium
C-rate	Charge discharge rate capability
CV	Cyclic voltammetry
CVD	Chemical vapor deposition
DANQ	2,3-Diamino-1,4-naphthoquinone
DFT	Density functional theory
DMC	Dimethyl carbonate
EC	Ethylene carbonate
EMI-Tf	1-Ethyl-3-methylimidazolium trifluoromethanesufonate
FTIR	Fourier transform infrared spectroscopy
GIXRD	Grazing incidence X-ray diffraction
GPC	Growth per cycle
GPE	Gel polymer electrolyte
HFP	Hexafluoropropylene
HOMO	Highest occupied molecular orbital
IL	Ionic liquid
LAB	Lead-acid battery
LAGPO	$Li_{1.4}Al_{0.4}Ge_{1.6}(PO_4)_3$
LGPS	$Li_{10}GeP_2S_{12}$
Li2TP	Lithium terephthalate
LIB	Lithium ion battery
LIC	Lithium ion conductor
LiHMDS	Lithium bis(trimethylsilyl)amide
LiPON	Lithium phosphorus oxynitride
LISICON	Li super-ionic conductor
LiSiPSCl	$Li_{9.54}Si_{1.74}P_{1.44}S_{11.7}Cl_{0.3}$
LiTHD	2,2,6,6-Tetramethyl-3,5-heptanedione

LUMO	Lowest unoccupied molecular orbital
MLD	Molecular layer deposition
NaTP	Sodium terephthalate
NTCDA	1,4,5,8-Naphthalenetetracarboxylic dianhydride
OCV	Open circuit voltage
PAA	Polyacrylic acid
PAN	Polyacronitrile
PC	Propylene carbonate
PDC25	2,5-Pyridinedicarboxylic acid
PDC35	3,5-Pyridinedicarboxylic acid
PEO	Polyethylene oxide
PMAA	Polymethacryclic acid
PMMA	Polymethylmethacrylta
PVdF	Polyvinylidene fluoride
QOCV	Quasi open-circuit voltage
SEI	Solid electrolyte interphase
SN	Succinonitrile
SPE	Solid polymer electrolyte
TFSI	Bistrifluoromethanesulfonylimide
TPA25OH	2,5-Dihydroxylterephtalic acid
TPA2A	2-Aminoterephtalic acid
TPABr	2-Bromoterephtalic acid
USPEX	Universal structure predictor: evolutionary xtallography
XRD	X-ray diffraction spectroscopy
XRR	X-ray reflectivity

1 INTRODUCTION

The current trend in the microelectronics industry is to shrink down the dimensions of every component, system and (bio)sensor, which makes it possible to cram more functionalities into smaller space. These devices often need a rechargeable power source which possesses a high-energy density, while occupying the smallest space possible. Lithium-ion batteries are by far the most efficient solution, since they offer the highest energy densities out of all commercial battery designs. Lithium thin film microbatteries have dominated the field for decades. They are based on a design, where the microbattery is directly integrated on the excess surface area of the device [1]. Currently, a commercial microbattery is up to 3 mm thick including packaging and delivers around 1 $mWcm^{-2}$ and $mAhcm^{-2}$ of power and capacity, respectively [2].

The energy requirement of microdevices has remained constant while the dimensions have shrunk faster than the power available per area has increased. The capacity of the microbatteries cannot simply be increased by increasing the thickness of the active battery materials, because increasing the thickness reduces the power density. The traditional methods of increasing the area by folding the active materials of the battery is not applicable for microbatteries, since the active materials are too brittle and the form factor would be altered. Therefore, alternative methods need to be considered. [1]

Surface area of a given substrate can be increased with numerous different approaches, but the general idea is to introduce nano/microsized interdigitated architectures to the substrate. The increase in the capacity per area is usually at least one order of magnitude when moving from 2D to 3D architectures [3]. A major difficulty with the 3D architectures is the deposition of uniform and pinhole free electrode layers on the substrate. This problem can be overcome by novel deposition techniques such as atomic layer deposition (ALD), which is an excellent but slow deposition method for creating uniform coatings on a substrate. The ALD technique is based on self-saturated surface reactions, where gaseous precursors react with each other in pulsed cycles. Various inorganic materials can be deposited with ALD and even organic compounds with molecular layer deposition (MLD).

The components of the battery have at least as much importance as the architecture. Organic electrode materials are a promising technology for battery applications because of their high theoretical capacities, fast reaction kinetics, and a possibility of undergoing multiple redox reactions per molecule. In addition, the redox properties of organic molecules can be tuned by modifying the conjugation of the carbon skeleton or by adding electron withdrawing or donating functional groups or heteroatoms. Additional benefits for microbattery applications is that the organic films are often flexible and transparent. The utilization of organics in the batteries makes the recycling process considerably easier and cheaper, since organic electrode materials can be synthetized from natural products. This makes it possible to design a fully closed loop for the lifespan of the battery. All these properties could be highly valuable for the next generation of microbatteries. One problem with the organic electrode materials is their tendency to dissolve in to the liquid electrolytes [4]. However, in microbatteries a solid electrolyte can be used instead, which removes the dissolution problem, is safer, and allows more flexibility in battery architectures.

The literature part of this thesis focuses on the 3D microbattery architectures and fabrication, followed by a short review on the current state of different solid electrolytes with their pros and cons. This is followed by a discussion on the electrochemical properties of the carbonyls (an organic electrode material) and especially what happens during the redox reactions and how they can be affected. The literature part concludes with the examination on sustainability of the current battery technologies and discussion about possible future trends of the battery development.

In the experimental part of this thesis, ALD and MLD are combined to fabricate novel lithium-organic hybrid thin films. With the ALD/MLD technique uniform and pinhole free layers can be fabricated, which are vital to high quality electrode materials. These hybrid materials are analogous to previously reported organic anode material lithium terephthalate (Li_2TP) [5,6]. The hybrid materials in this study have an additional functional group or heteroatom in respect to Li_2TP. The groups are either electron donating or withdrawing and therefore they alter the redox properties. The goal is to develop new ALD/MLD processes for lithium-organic hybrid thin films and to see which functional group is the most effective at tuning of electrochemical properties.

LITERATURE PART

2 MICROBATTERIES

Microelectromechanical systems, microscale devices *e.g.* biomedical devices [7], and self-powered microelectronics [8] require power sources that have high power and energy densities at a microscale. Lithium-ion batteries (LIBs) are currently the best option for battery miniaturization, since LIBs provide a high gravimetric and volumetric power and energy densities and are already a well-known technology [9]. In this chapter, the working principle, components, fabrication and other important factors of microbatteries are discussed.

2.1 Battery Basics

Most of the hand held and portable devices uses LIBs as their power source. Lithium metal is light and the lithium ion has exceptionally high charge to radius ratio, which is important for efficient charge carrier. The small size of the ion allows it to diffuse through the electrolyte with relative ease compared with some other ions such as Na^+ or Mg^{2+} [10]. The self-discharge rate of the LIBs is also low [9]. Each LIB is built from a negative (anode) and a positive (cathode) electrode and the electrolyte. A typical anode material in bulk LIBs is graphite and a typical cathode material is $LiCoO_2$, which works by intercalating the lithium between layers of $[CoO_2]^-$. Common electrolyte is $LiPF_6$, and other organic lithium salts, dissolved in ethylene carbonate (EC) and/or dimethyl carbonate (DMC). [9] The components of LIBs can ideally be tuned to fit the requirements of the application, but further improvements are still needed. Working principle of conventional LIB during the discharge is presented in Figure 1.

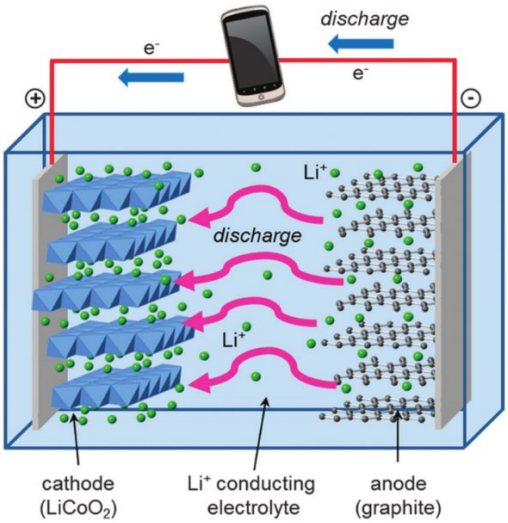

Figure 1. A schematic representation of the conventional LIB during the discharge cycle. During the discharge lithium ions move from anode to cathode through the electrolyte, while the electrons flow through the external circuit and the current can be drawn from the cell to power up devices. Opposite is true for charging. [11]

Naturally, the basic components of microbatteries are the same as in bulk LIBs. However, at smaller scales the use of liquid electrolyte and conventional electrode materials is rather difficult, because the preparation of the microbatteries requires precise microfabrication processes. Thus, the bulk battery research focuses on optimizing and finding new electrode and electrolyte materials while microbattery research focuses on the ingenious fabrication methods and architectures of electrodes. [9]

2.2 2D Architectures

Microbatteries can roughly be categorized into two groups two- and three-dimensional designs. The two-dimensional designs mean the planar designs that are common in traditional batteries. A conventional 2D microbattery is schematically shown in Figure 2.

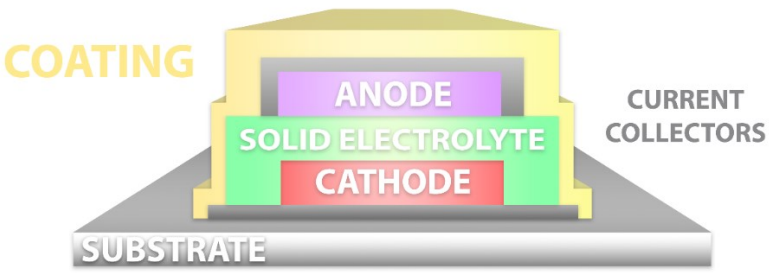

Figure 2. A schematic representation of traditional 2D all-solid-state lithium-ion battery [12].

The operating principle of microbattery does not differentiate from a normal battery. However, the electrodes are only composed of active material and the electrolyte is usually solid. The thickness of the cell usually is < 20 µm, where the contribution of the electrolyte layer is 1-5 µm [1]. Since the applied layers are thin, the resistance for lithium ion diffusion is low and the use of a solid electrolyte is possible [13]. Solid electrolytes are more mechanically, thermally and electrochemically stable [9]. Power density is an important factor in microbatteries since the space is often limited. However, increasing the thickness of the thin film layers does not increase the power density of the battery, since the current path length would also be increased. This is why in microbatteries capacities are often measured in units of capacity per area. [1]

Increasing the thickness of the 2D battery does not increase the power per area due to the ohmic drop in the electrolyte layer. Maximum power per area with some simplifications, can be estimated with Equations I and II. [1]

$$R \cdot A = \frac{D_{seperator}}{\sigma_i}. \tag{I}$$

$$P_A \approx \frac{V_{OCV}}{2} \cdot \frac{V_{OCV}}{2RA} = \frac{\sigma_i (V_{OCV})^2}{4D_{seperator}}. \tag{II}$$

In the equation, R is the resistance, A is the footprint area, $D_{seperator}$ is the thickness of the separator, σ_i is the ionic conductivity, V_{OCV} is the open circuit voltage (OCV) and P_A the power available per area. The maximum power that can be drawn from the cell is at the half point between the short circuit voltage and the open circuit voltage. [1]

The power density of the 2D batteries can be increased by rolling the films to create a high surface area in as small as possible volume. However, this approach is usually not the optimal one, since many electrode materials are brittle and end up cracking during the process causing short circuits [1]. Alternative approach is to construct small rods, holes, or any other interdigitated structures on to the 2D substrate. This way the surface area of the substrate is increased substantially. In addition, if the material possesses a low resistance, it can directly be used as a current collector in the battery. One order of magnitude increase in the capacity per area, when moving from 2D to 3D architectures, was reported by Cheah *et al.* [3] In the research, Al nanorods and flat Al substrate were coated with TiO_2. The result can be seen in Figure 3.

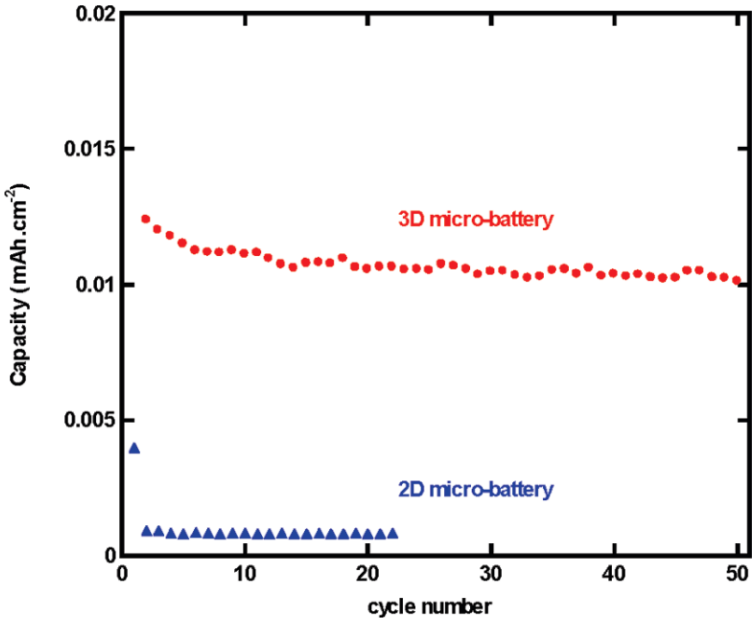

Figure 3. Capacity for 2D and 3D architectures. In both architectures the positive electrode is TiO_2 and the negative electrode is lithium metal. [3]

The planar designs of microbatteries (Figure 2) are by far the most popular in micro applications. The 2D batteries can be prepared basically with any thin film fabrication technology *e.g.* chemical vapor deposition (CVD), RF magnetron, sputtering and sol-gel [9]. Companies such as Panasonic [14] and VARTA [15] already offer commercial 2D microbatteries. Recently a Belgian research institute Imec developed a novel way to deposit a solid electrolyte for LIBs on a 3D substrate, using an atomic layer deposition (ALD) apparatus provided by the Finnish company Picosun [16]. The following chapter discusses about the various 3D architectures.

2.3 3D Architectures

Three-dimensional architectures can be created artificially by folding the flat substrate in to multiple layers. However, these structures do not possess high aspect ratios. The 3D architectures with high aspect ratios are a novel way of increasing the capacity per area. These architectures were roughly divided into 4 groups by Long *et al.* [17] in Figure 4.

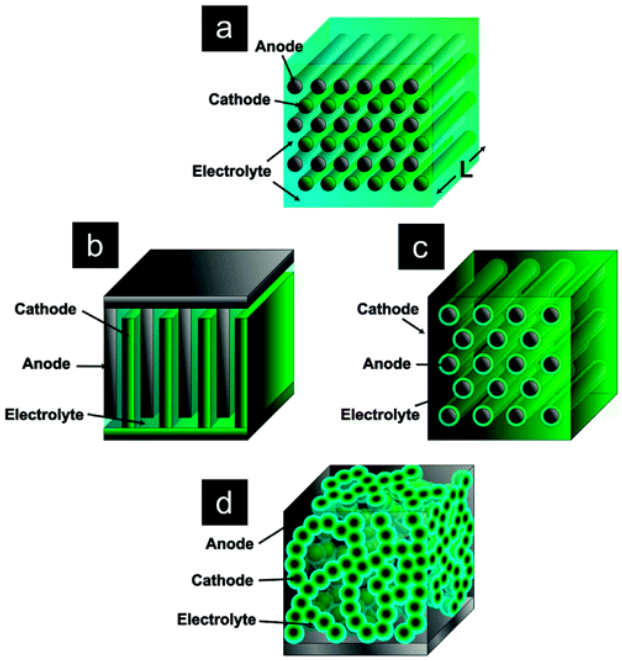

Figure 4. A schematic representation of various 3D microbattery designs. In *a* the rods are electrodes separated by the electrolyte. In *b* each plate is an electrode separated by electrolyte. In *c* each rod is an electrode coated with a thin layer of electrolyte and rest of the free space is occupied by the counter electrode. In *d* there is a sponge like configuration where each small particles of electrode are coated with electrolyte, while rest of the free space is coated with counter electrode. [17]

The general idea with 3D architectures is to reconfigure the positions of the electrodes in a way, which minimizes the diffusion distances of the lithium ions. The transport pathway should also be kept one-dimensional between the electrodes. A very common way is to create interdigitated architectures, which means that the electrodes are interlocked. These modifications significantly increase energy density of the batteries [17]. However, few problems arise from the 3D design. The electrode arrays are experiencing stress due to the uniform current density and limited conductivity. This is why the size, shape and spacing of the electrodes need to be controlled to achieve the maximal capacity and durability of the battery. [18]

Many slight derivations from the architectures presented in Figure 4 can be found in literature. Methods already developed for nanoarchitectures [19], micro machining [20], or even 3D printing [21] can be applied to achieve high surface area substrates and electrodes.

2.3.1 Template based Morphology

A template is used to selectively deposit certain areas to create a 3D morphology. The advantage of using the template is that it can usually be removed by etching or dissolving, leaving only the active material behind. The deposited materials usually act as a current collector for the electrode. [12]

In the work reported by Perre *et al*. [22] porous alumina membranes acted as a template for the electrochemical deposition of aluminum. Alumina was chosen as a template, because its pore diameter and occurrence were easily modifiable. After the deposition and dissolving the template, free-standing aluminum rods are received, which can be utilized as a template for further depositions or straight as a cathode current collector. Similar free-standing rods of Cu/Cu_2O were fabricated with electrodeposition by Leopold *et al.* [23]. In their work, the template was an ion tracked polycarbonate membrane, which could be used to precisely control the size of the pores. The similarity of the structures can be seen in scanning electron microscope images in Figure 5.

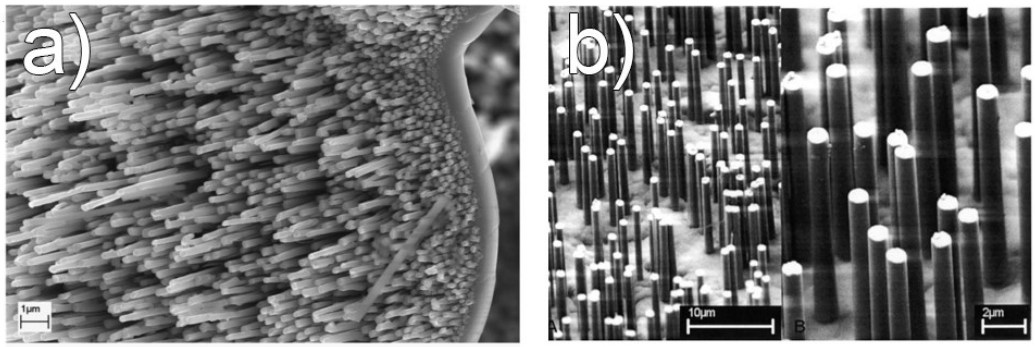

Figure 5. Free-standing Al rods from ref. [22] and Cu/Cu_2O rods from ref. [23] are presented in *a* and *b*, respectively. Al rods grew more frequently, but the density of rods is wholly dictated by the template. [22,23]

2.3.2 Interdigitated Structures

Interdigitated structure describes an architecture, where the electrodes are folded together, as when the fingers of one hand are crossed with another. The basic template for the interdigitated structures is often made with photolithography. Photolithography is commonly used in semiconductor industry and can also be applied to the design of microbatteries. In photolithography, the substrate is coated with a photoresist and then exposed to light. Photoresist decomposes in areas that are exposed to the light, while

the masked areas stay unharmed. Exposed areas of the substrate can then be chemically etched and the rest of the photoresist removed. All what is left is the substrate that was protected by photoresist during the etching. Rather sophisticated photolithography methods have been developed, since the whole integrated circuit industry depends on it. [24]

Ning *et al.* [25] reported a 3D microbattery with $LiMnO_2$ cathode and NiSn anode. The microbattery utilized 3D holographic lithography in addition to conventional photolithography. Their method is presented in Figure 6.

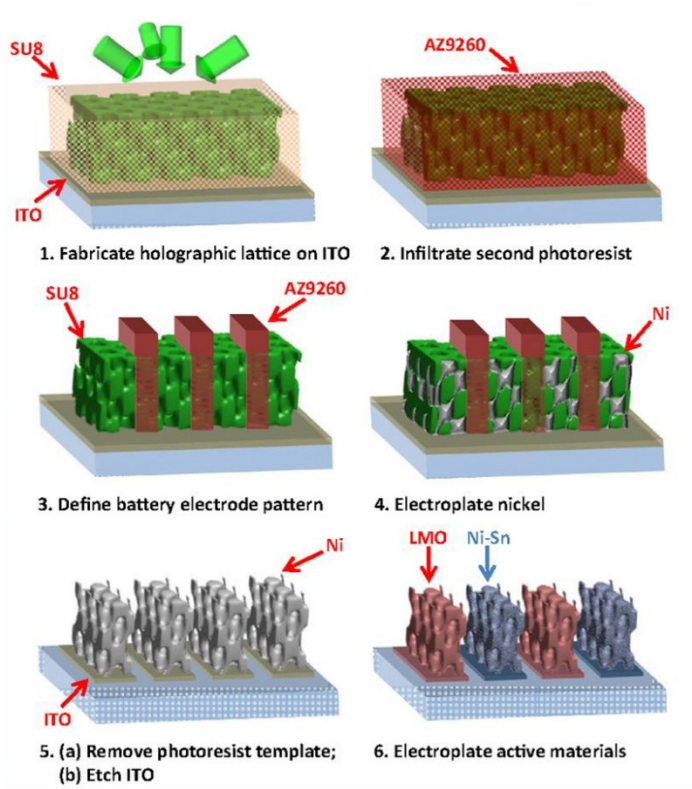

Figure 6. A schematic illustration of the fabricated 3D microbattery with interdigitated electrodes. In (1) the 3D lattice is formed on indium tin oxide (ITO) from photoresist SU8 with holographic lithography. In (2) the lattice is coated with another photoresists AZ9260 and 2D photolithography is used to selectively remove the AZ9260. In (3) the pattern of electrodes is defined. In (4) nickel is electrodeposited, which creates an inverted lattice from nickel. In (5) all of the photoresists is removed and ITO between the electrodes is etched, electrically separating the electrodes. In (6) nickel lattice is electrodeposited sequentially with Ni-Sn and MnO_2. [25]

Pikul *et al.* [26] recently reported a microbattery utilizing nanoarchitectures, with a bicontinous interdigitated microelectrodes, which in theory are highly scalable. The template for electrodeposition was made with photolithography to achieve the

interdigitated structures of the electrodes. Some of their results are presented in Figure 7.

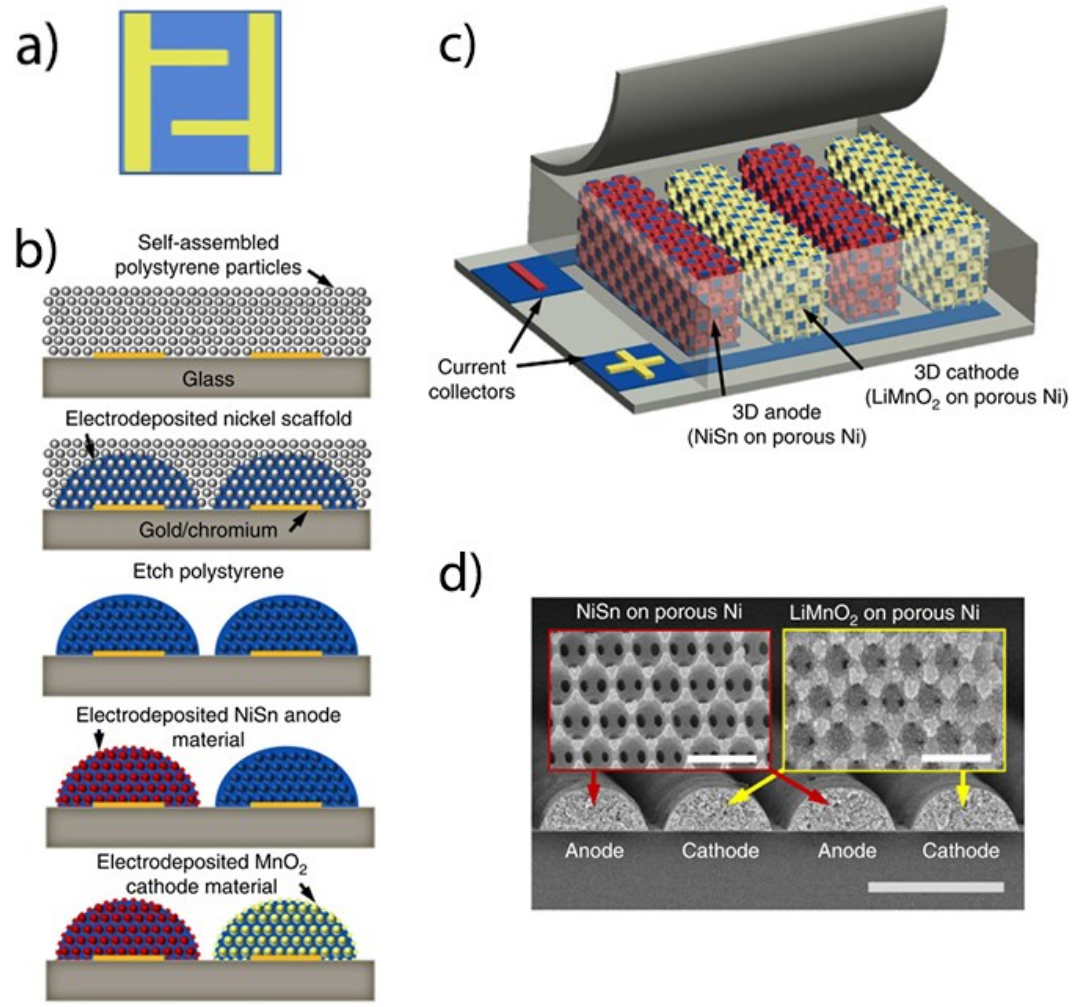

Figure 7. Different phases during the fabrication process of the porous electrodes. Where *a* is the substrate viewed from the top. In *b* is the basic schematic of the fabrication. In *c* is the completed design of the battery. In *d* is the SEM image of the cross section of the electrodes. [26]

The base of the electrodes utilized a gold or chromium electrode template that was fabricated by traditional photolithography methods (Figure 7a). Fabrication of the electrodes began with self-assembly of polystyrene on the substrate. This was followed by the electrodeposition of nickel, which grew only on the metal template. Finally the polystyrene layer was etched. Nickel current collectors could be sequentially electrodeposited with the desired electrode materials (Figure 7b). The deposited nickel current collectors are extremely porous, the pore diameter varies from 330 to 500 nm, and thus, the deposited electrodes are also highly porous. This microarchitecture is an example of design that provides short electron and ion pathways and provides high

power density. According to Pikul *et al.* [27] the battery provides two thousand times greater power density than any other microbattery. However, the battery loses around 5 % of its total energy after each cycle at 1 C, which may be due to the formation of the solid electrolyte interphase (SEI) layer. Furthermore, their study suggests that focusing on architecture rather than the materials is a very important aspects in the design of the microbatteries.

Recent developments in 3D printing technology may give rise to a whole new kind of method to fabricate microstructures. Sun *et al.* [21] reported the first 3D printed microbattery, with a high aspect ratio on a glass substrate. The battery's interdigitated electrodes were printed from inks containing $Li_4Ti_5O_{12}$ and $LiFePO_4$ nanoparticles. The battery utilized a liquid electrolyte, but the dimension could be further shrunk by printing a gel or a solid electrolyte during the fabrication process. Figure 8 summarizes the architecture and the printing procedure.

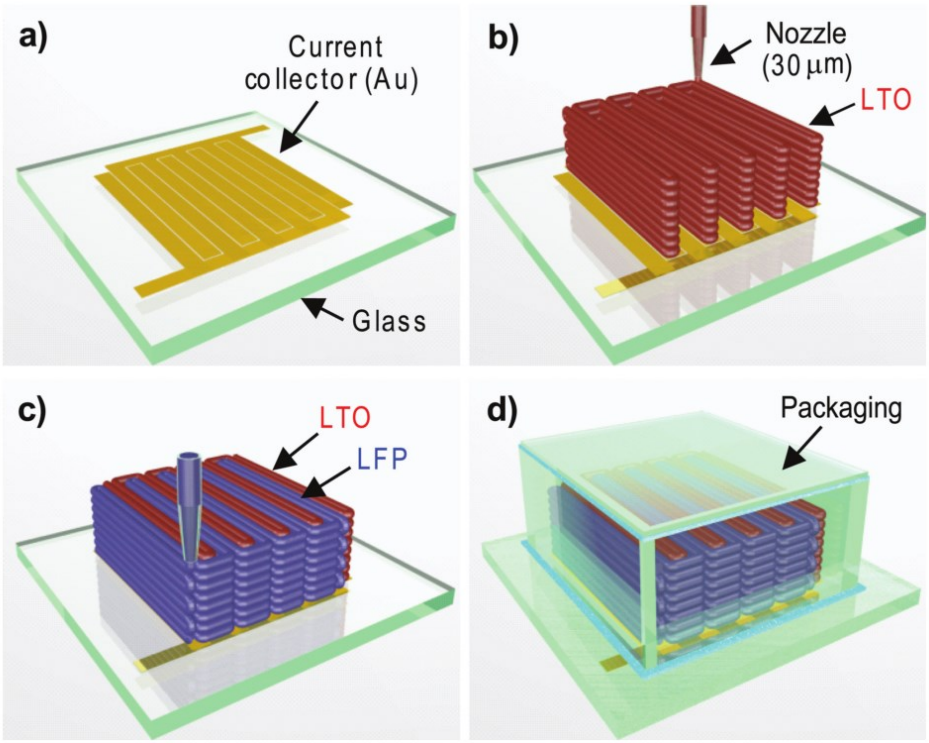

Figure 8. A schematic representation of the 3D printed microbattery fabrication process and the architecture. In *a* the printed gold on glass substrate gives a template of the interdigitated structure. In *b* and *c* the lithium titanate (Li_2TiO_3) and lithium iron phosphate ($LiFePO_4$) ink is printed with a very tiny nozzle, respectively. In *d* the cell is wrapped in packaging and the liquid electrolyte is added. Figure is adapted from ref. [21].

Yet another interdigitated design can be achieved with a honeycomb architecture. Kotobuki *et al.* [28] reported a solid electrolyte $Li_{0.35}La_{0.55}TiO_3$ with a honeycomb

structure. Pores of the solid electrolyte were impregnated with $LiCoO_2$ and $Li_4Mn_5O_{12}$ particles, prepared with sol-gel. They managed to fabricate a fully functioning battery, but further optimization on the impregnation of the holes and the 3D design are still needed, since the discharge capacity was lower than expected. A cross-sectional SEM image of the battery can be seen in Figure 9.

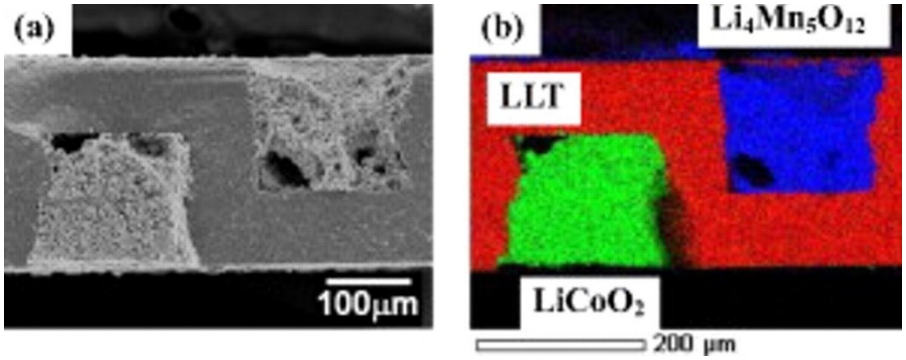

Figure 9. Cross-sectional SEM images of the honeycomb structured $LiCoO_2$ | $Li_{0.35}La_{0.55}TiO_3$ | $Li_4Mn_5O_{12}$ battery [28].

2.3.3 Surface Etching

Another approach is to utilize etching to create a metal or a silicon plate that is punctured with microchannels or holes to increase the active area of the battery [12]. Etching is a process, where part of the substrate is selectively removed with aqueous chemicals (wet etching) or with vapor or plasma (dry etching). The selectivity of etching in micro and nano dimensions is usually achieved when etching is combined with photolithography. With it, an etching mask can be fabricated on the surface that enables the selective etching. [20]

Nathan *et al.* [29] demonstrated a battery architecture based on a punctured silicon plate. In the study, silicon substrate was first coated with nickel, functioning as a current collector. Nickel layer was followed by a molybdenum sulfide cathode and a commercial hybrid electrolyte. The cell was finished with a carbon anode and the whole apparatus was assembled into a button cell. The advantage of this design is that substrate can function as one of the current collectors while the channels provide a higher active area. Because deposition occurs on both sides of the substrate, the management and integration of the battery could prove to be difficult. The integration problem could be solved with a method proposed by Notten *et al.* [30] where high aspect ratio crevices could be integrated straight in to the silicon substrate to increase

the active area. Crevices could then be fabricated with battery components with electrodeposition or ALD. [30] A schematic representation of these designs is shown in Figure 10.

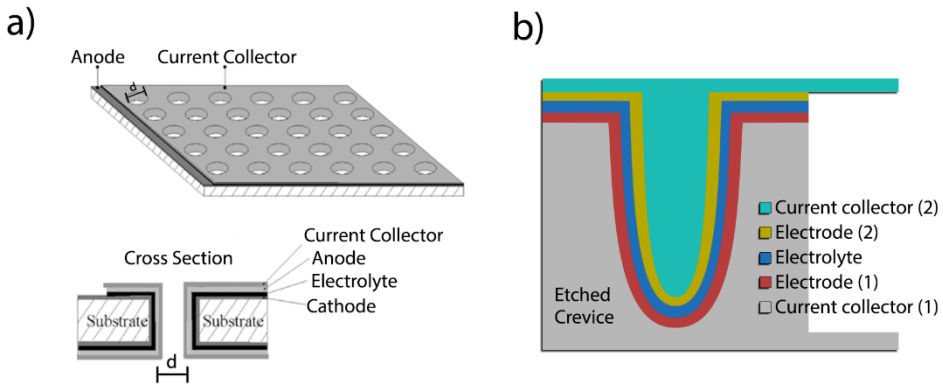

Figure 10. A schematic representation a) and b) of the architectures by Nathan *et al.* and Notten *et al.*, respectively. In a) the whole architecture is shown in upper image, while the bottom one shows a cross section of one hole. Figure is adapted from refs. [29] and [30].

2.3.4 Aerogel based Structures

Aerogels are randomly orientated structures that possesses a high free volume up to 75-99 %. Aerogels are usually prepared with sol-gel synthesis [19]. If aerogels are coated with electrodeposition or ALD, the resulting electrode will have a high area with current collector build inside. However, it is difficult to deposit uniform surfaces on random structures, such as aerogels. Additionally, to make a fully functional battery the electrolyte and the counter electrode need to be included in the design. The electrolyte needs to be deposited cautiously, since if the coating is not uniform, short circuits will occur. Connecting the anode to the current collector is also problematic. One solution is to use nanoparticle islands that are each separately connected to the current collector. [12]

2.4 Deposition Methods

Multiple deposition methods have been used to coat the substrate, basically all the thin-film techniques. However, the most important factor is how well that particular technique can penetrate into the substrate's 3D structure. This is why the focus in this chapter will be on electrochemical deposition and on atomic layer deposition, since they offer the best penetration into the 3D structures. [12]

2.4.1 Electrochemical Deposition

Electrochemical deposition or electroplating is a low temperature technique. It can be used to coat substrates, even with complex 3D architectures. The low temperature is a significant advantage over other methods since high temperatures are often undesirable in the manufacturing process of the 3D microbatteries. Electrochemical deposition can be used to fabricate negative and positive electrodes, solid electrolytes, and current collectors. Also, it can simply function as a template for further depositions. [27]

The amount of deposited material can be precisely controlled by the applied current. Moreover, the deposition can occur in a layer-by-layer fashion, by pulsing or limiting the current so the concentration profile has time to reach the equilibrium in between the cycles. The only requirement for electrodeposition is: the deposited material and the substrate need to be conductive. Although in principle, if the deposited material is not conductive, the electrodeposition becomes a self-limiting reaction, which can be used as an advantage when depositing homogeneous surfaces. These non-conducting homogeneous surfaces could be highly effective solid electrolytes in all-solid-state LIBs. Figure 11 is an example process of electrodeposition where it can be utilized in deposition of 3D morphologies. [12]

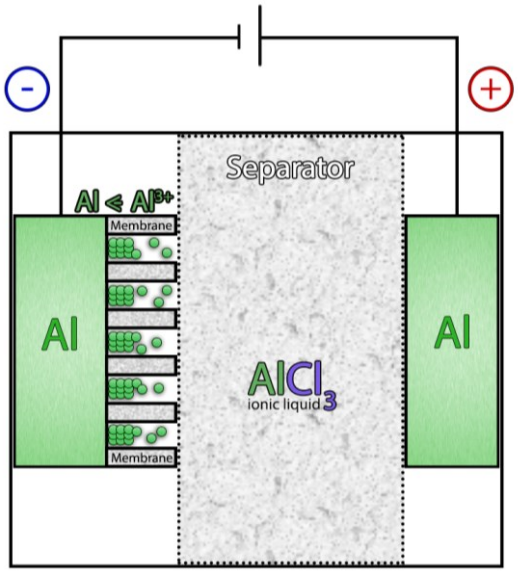

Figure 11. A schematic representation of electrodeposition of aluminum nanorods from $AlCl_3$ ionic liquid. The membrane can be selectively etched, leaving only the aluminum nanorods on the surface of the aluminum electrode. [22]

Electrochemical deposition is often applied on metals and their oxides, which makes it a good deposition method for fabricating electrodes, but the deposition of organic molecules, to form a solid electrolyte for microbatteries is more challenging. Deposition of organic molecules is possible with a process called electropolymerization. The process is fairly similar to electrochemical deposition, but upon the oxidation or reduction of the monomer, it forms a new covalent bond with another monomer chaining them together. Many electrode surfaces are suitable for electropolymerization, but quality of the films will decrease upon an increase in the size of the electrode [31]. Films deposited with electropolymerization, can function as a hybrid/gel electrolyte when for example soaked with liquid $LiPF_6$ [32].

2.4.2 Atomic Layer Deposition

The ALD method is a layer-by-layer deposition technique, which is based on self-limiting surface reactions. It is closely related with chemical vapor deposition where layer formation is based on chemical reaction in gas phase rather than physical condensation as in physical vapor deposition. All of these techniques can be used in the deposition of microbattery architectures. However, the ALD method is the best method for creating uniform pinhole free layers. These properties are vital especially when depositing solid electrolytes onto 3D architectures. [12]

In each ALD cycle, a sublimated precursor is pulsed into a reaction chamber, where it reacts with the surface and forms a monolayer. This is followed by purging the reaction chamber with nitrogen or other inert gas to flush away the unreacted precursors or the reaction byproducts. Now the second precursor can be pulsed into the reaction chamber, where it reacts with the first precursor and forms a second monolayer and one layer of the reaction product. First cycle comes to the end with another purge and the process can start from the beginning. This was an example of a binary process, but ternary systems are also possible. Each of the precursors pulses are called half-cycle reactions, which are vastly different from electrochemical half reactions, where reactions occur simultaneously on the respective electrode. A schematic representation of the ALD method is drawn in Figure 12. [33]

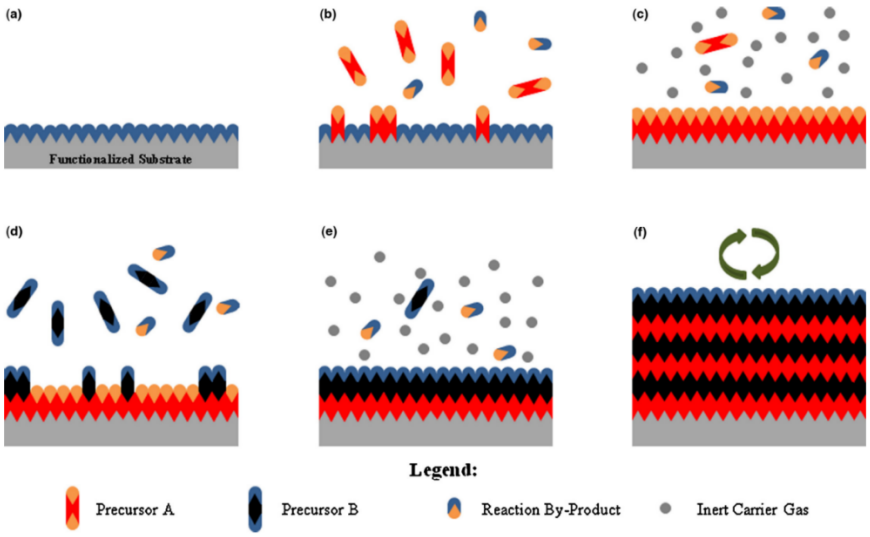

Figure 12. An overview of the ALD process. Where in (a) the free surface sites of the substrate are visible. In (b) the precursors A is pulsed into the reaction chamber, where it reacts with the surface, whereas in (c) all the free surface sites have reacted, and excess precursor A and any reaction side products are purged away with an inert carrier gas. In (d) the precursor B is pulsed into the reaction chamber, where it reacts with the layer formed by precursor A, and in (e) precursor B is purged away with any reaction by products. Steps (b) to (e) can now be cycled as shown in (f). [33]

The ALD deposition usually occurs at relatively low temperatures (< 350 °C) and at low pressure (around 2 mbar). The temperature range where the growth rate is linear, is called the ALD temperature window. In this temperature range, increasing the pulse time will have no effect on the growth rate, because all of the surface sites have already reacted. Within this window, the thickness of the films can easily and precisely be controlled, simply by modifying the number of ALD cycles. The thickness and the composition control and the ability to fabricate 3D structures are important factors when looking at the depositions of battery components. The tradeoff is that the ALD is rather slow technique. Moreover, as the aspect ratios and the surface area of the substrate increase so does the time needed for pulsing and purging. However, time needed for these operations is highly dependent on the type of the reactor. [33]

Vast amounts of different elements, oxides, and sulfides have been fabricated with ALD in both amorphous and crystalline forms. Especially, the deposition of lithium thin films is an important aspect when looking at the battery components. Nilsen *et al.* [34] have written a review on the "Atomic layer deposition of functional films for Li-ion microbatteries", which lists many of the inorganic anode and cathode materials already deposited with the ALD method. In addition, the deposition of whole

molecules is also possible with molecular layer deposition (MLD). The only difference between the ALD and the MLD method is that during MLD a whole molecule is deposited on the substrate. The deposition of hybrid thin films is possible, when the ALD and MLD methods are combined. This broadens the range of possible electrode materials, which can be deposited with ALD/MLD. More specifically, the ALD/MLD method allows the depositions of organic materials in their fully lithiated state [35]. For example in the article written by Nisula *et al.* [5] ALD/MLD technique is used in depositions organic anode material (lithium terephthalate, Li_2TP). Additionally, these Li_2TP films were coated with lithium phosphorus oxynitride (LiPON), to mimic the electrode–solid electrolyte interphase.

2.4.3 All-Solid-State Battery with ALD

Just recently Pearse *et al.* [36] reported a functional all-solid-state battery deposited with ALD. The battery used V_2O_5 cathode, Si anode, and solid electrolyte LiPON. The capacity of this devices was too small to be practically useful. However, the article demonstrates that fabricating microbatteries with only the ALD method is possible. They also presented the penetration capabilities of their solid electrolyte process, on punctured silicon substrate and the results were promising. ALD will be at its prime, when surface modifications are either holes or pillars on the structure, since in practice they are the only surface modifications, which can be used to fabricate all solid-state batteries with ALD. The ALD method is also predicted to be the best method to deposit thin electric insulators, however the study of the electrolytes and the solid-solid interfaces is still an important aspect when looking at all-solid-state microbatteries. The different types of solid electrolytes are discussed in the following chapter.

3 SOLID ELECTROLYTES

Replacing the liquid electrolyte with the all-solid-state electrolyte will increase the overall safety of the battery and allows more flexibility in the battery design, because there is no liquid that needs to be contained. Safety problems with liquid electrolytes arise from the decomposition of the electrolyte during the cycling of the battery. These reactions are usually rather exothermic and often include gaseous by-products, which may increase the pressure inside the cell. In addition, the liquid electrolyte usually reacts with the electrode forming a SEI layer, causing an irreversible capacity loss. The liquid electrolyte may also undergo deterioration, caused by irreversible reactions with the electrodes. The deterioration also introduces additional safety problems. These phenomena may lead to the formation of metallic lithium dendrites and/or exfoliation and degradation of the electrodes. These problems with the liquid electrolyte have motivated researchers to find the alternative solutions. [37]

The challenge of the solid electrolytes is to bring the lithium ion conductivity on a par with liquid electrolytes [38]. For the solid electrolyte to be considered viable, the ionic conductivity should be in the order of $1 \cdot 10^{-4}$ S cm^{-1} at room temperature. A common liquid electrolyte $LiPF_6$ may exhibit conductivity of $1 \cdot 10^{-3}$ S cm^{-1} for example [37]. In addition, the electrolyte layer needs to be pinhole free and have negligible electric conductivity to avoid self-discharge [8]. Naturally thicker electrolyte layers are less prone to possess pinholes, but as seen in equation II, fabricating thicker electrolyte layers decreases the power available per area. Furthermore, the electrolyte interphase with the electrode needs to be electrochemically stable and the interfacial resistance low as possible. The lithium ion transport number, which needs to be close to unity, and the thermal and mechanical stability of the electrolyte are also important properites of the electrolyte [37]. The development of the batteries usually relies as much in improvements made on electrolytes as in electrode materials [8].

Currently the market leading solid electrolytes are polymer based, even if many of them are in reality hybrid or gel electrolytes [39]. Solid electrolytes can roughly be divided into three different subgroups: inorganic, ceramic or polymer based solid electrolytes [40].

3.1 Polymers

Polymer based electrolytes can be further divided in five classes originally proposed by Scrosati *et al.* [41]. 1st class is the polymer/salt complexes, 2nd is the plasticized electrolytes, 3rd is the gel electrolytes, 4th is the polymer in salt, and 5th is the nanocomposite electrolytes. These classes can be further compressed into solid polymer electrolytes (SPEs), classes 1 and 5, and gel polymer electrolytes (GPEs), classes 2 and 3 as proposed by Quartarone *et al.* [37]. The polymer in a salt electrolyte is left out of this definition, because it has not yet been as successful as other approaches.

3.1.1 Solid Polymers

SPEs are systems based on polymer-salt complexes, which are ion-conducting. SPEs do not include any liquid components. The most applied polymer as a matrix for SPEs is polyethylene oxide (PEO) and its copolymers. PEO itself is a semi crystalline polymer in room temperature (glass transition temperature, T_g is around -60 °C) and it is able to dissolve lithium salts, because of its high dielectric constant. The first SPEs were modifications of PEO_n-LiX system, where X is the anion from the lithium salts and the *n* is the molar ratio of PEO and Lithium. Naturally, the applied lithium salt affects the conductivity, with a general trend being that larger and more electrically delocalized anions demonstrate higher lithium transport numbers. The Li-ions conduct in the PEO matrix with oxygen assisted hopping mechanism, which takes place in the amorphous regions of the polymer. At the temperatures near the melting point (65 °C), the conductivity of the PEO reaches maximum, due to the amount of crystalline regions being at minimum. [37]

Since the conductivity is proportional to the crystallinity, some approaches use plasticizers that decrease the degree of crystallinity of the polymers [42]. This way the conducting mechanism stays intact, while conductivity is increased. Some of the common plasticizers include: succinonitrile (SN) [43], polyacrylic acid (PAA) [44], polymethacryclic acid (PMAA) [44], ethylene carbonate (EC) [45], and propylene carbonate (PC) [45]. Overall, adding the plasticizers increases the ionic conductivity of the electrolyte in the room temperature when compared with PEO. A study concluded by Pitawala *et al.* [45] on EC and PC plasticizers revealed an increase in

the conductivity from 7.8 $\cdot 10^{-6}$ S cm^{-1} to 1.2 $\cdot 10^{-4}$ S cm^{-1}. Decreasing the degree of crystallinity in the polymer weakens the mechanical properties and in addition the amorphous phases are metastable, which means that the polymers slowly recrystallize [37].

This problem can be partly solved by adding a nanosized ceramic filler to the PEO matrix, which improves the mechanical properties of the polymer. Furthermore, adding the ceramic particles can increases the ionic conductivity of the polymer by up to two orders of magnitude in ambient pressure and temperature. Ceramics increases the conductivity by decreasing the crystallinity of the PEO, but since the conductivity of the polymer increases even in elevated (> 70 °C, polymer in the amorphous state) temperatures when ceramic filler is present, some other effects must also apply. It has been suggested that the added ceramic acts as a cross linking center between anions species of the lithium salt and the PEO polymer chains. These beneficial ceramic induced structure modifications increase the amount of free Li^+ in the structure allowing the Li-ions to diffuse more freely over the ceramic extended surface. The interaction between ceramic and the anionic species of the electrolyte is also a Lewis acid-base reaction which disturbs the ionic coupling of lithium salt, again making the Li^+-ions more accessible. Both of these effects contribute positively to the lithium transference number [46]. Common nanosized ceramic fillers include, but are not limited to Al_2O_3 [46], MgO [47], SiO_2 [48], many other oxides and their mixtures [42], and a few perovskites [49]. The optimal amount for the filler is depended on the substance, but for example optimal content for Al_2O_3 is around 10-20 wt. %, and many other fillers fall in the same range [48,50]. Al_2O_3 and SiO_2 are typically categorized as inert fillers, because they do not provide extra lithium for the polymer matrix. Active ceramic fillers like $Li_{1.3}Al_{0.3}Ti_{1.7}(PO_4)_3$ provide extra lithium in to the polymer matrix and may further contribute to increased conductivity [51]. Figure 13 shows the enhanced durability of the SPE over time achieved by using ceramics.

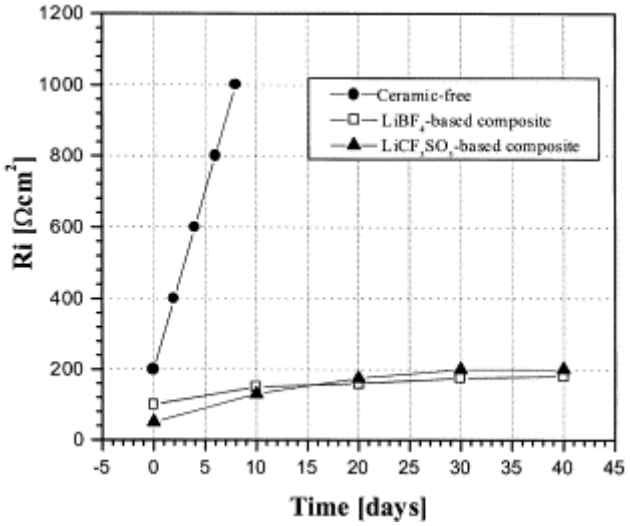

Figure 13. Ceramics enhanced durability over time reported by Croce *et al.* of SPE PEO with LiBF and $LiCF_3SO_3$ salts [52].

So far only the various materials have been discussed, but morphology also has a huge effect on ionic conductivity. Recently Liu *et al.* [53] reported an increase in ionic conductivity, when ceramic $Li_{0.33}La_{0.557}TiO_3$ nanoparticles were replaced with ceramic nanowires. At the same wt. % and similar grain size, improvements over three orders of magnitude were reported. This enhanced conductivity was probably due to the longer Li^+ transport channels over the wires and from minimizing the particle-particle junctions, which Li^+ must travel across. Additionally nanowires compared with nanoparticles are not that prone to aggregation, which decreases conductivity over time.

Comparing the conductivities of the electrolytes from different sources is somewhat difficult because they use different plasticizers, ceramic fillers, and lithium salts. Recently the combined effect of plasticizers and ceramic fillers has been looked into more carefully. Furthermore, SPEs still need improvements, but with the combinations of nanostructured ceramic fillers and efficient plasticizers yet enhanced conductivities are reachable. [45]

3.1.2 Gel Polymers

A second approach is to add the liquid electrolyte to the solid polymer to create a gel polymer electrolyte (GPE). GPEs can also be classified as hybrid polymer electrolytes, because their properties are inherited from both liquid and solid systems. GPEs often

exhibit liquid style conductive phenomenon while also retaining the shape flexibility and safety aspects of solid materials. Preparation of the GPEs often includes a swelling of the pores inside of the polymer matrix with the electrolyte. This is followed by further trapping the electrolyte with carbonate esters. Polymer matrices with high mechanical and chemical stability and with strong electron-withdrawing groups, to introduce dipole moments, are highly desired properties for the polymer matrix. [37]

The most utilized GPE is poly(vinylidene fluoride) (PVdF) swelled with hexafluoropropylene (HFP), but many other polymers have also been reported functioning as the polymer matrices *e.g.* polyacronitrile (PAN) [54] or poly(methyl methacrylate) (PMMA) [55]. A schematic illustration of preparation of the PVdF-HFP is presented in Figure 14.

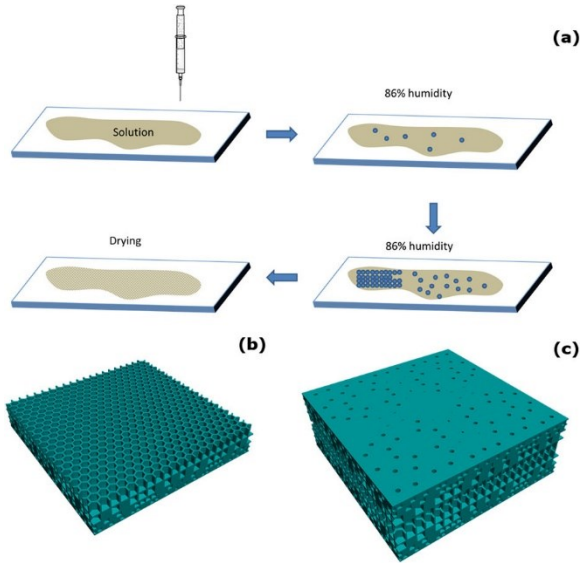

Figure 14. A schematic illustration of preparation and morphology of the PVdF-HFP GPE. [56]

GPEs consists of three different phases, polymer's crystalline and amorphous phases and the added liquid phase, which starts to form liquid cavities at higher wt.% concentrations (> 50%). The amount of amorphous phase in the polymer increases with the wt. % of the liquid electrolyte. The conductivities with GPEs with liquid electrolytes are higher than in SPEs, around $1.0 \cdot 10^{-3}$ to $1 \cdot 10^{-4}$ S cm^{-1}, respectively [57]. The conductivity of the GPEs can be increased by adding ceramic nanoparticles, similarly as in SPEs, they also increase the mechanical properties [37]. The polymer matrix can also be made more robust, by cross-linking the polymer chain [54], or by introducing a nanosponge morphology [58].

The biggest challenge with GPEs is the liquid electrolyte, which struggles with the same aspects as conventional LIB electrolytes, *e.g.* the evaporation of the electrolyte at elevated temperatures, the thermal runaway, and the high vapor pressure of organic carbonates. These obstacles can be overcome with the use of ionic liquids (ILs). ILs are organic salts that are in liquid form under 100 °C, preferably even at room temperature. ILs have considered being rather environmental friendly, compared with the solvents which cause a lot of emissions when used in the industrial scale. ILs possess good solvating potential, are thermally stable, and they are highly tunable, since cations and anions can be chosen to fit each application. ILs can be classified in four different types, which can be seen in Figure 15. [59]

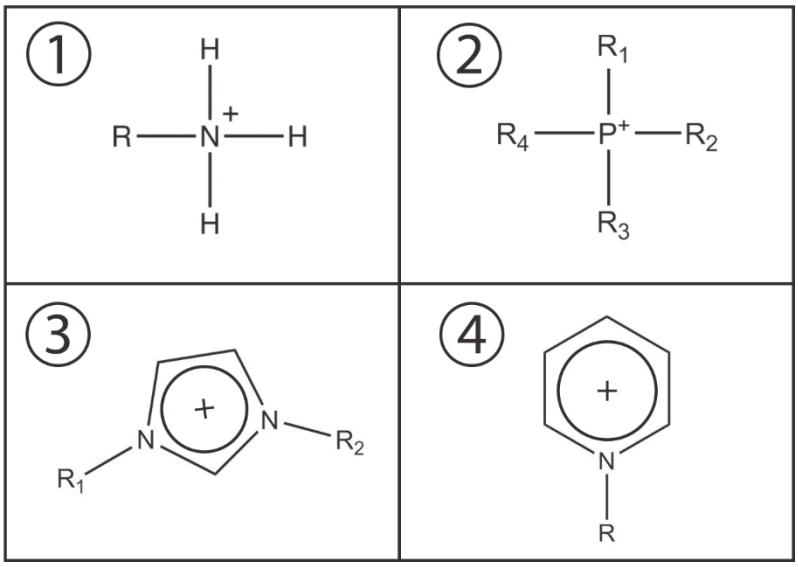

Figure 15. Four different base cations of ionic liquids. Where 1 is Alkylammonium, 2 is phosphonium, 3 is dialkylimidazolium and *N*-alkylpyridinium cations. Most ILs used in literature are derivations of these molecules. [59]

The conductivity of ILs are higher than SPEs or GPEs utilizing the common electrolyte liquids. For example, GPEs with IL electrolyte exhibit conductivity of $2 \cdot 10^{-3}$ S cm^{-1} and $2.34 \cdot 10^{-3}$ S cm^{-1} in room temperature as reported by Liao *et al.* [58] and Zhang *et al.* [60], respectively. Lia *et al.* used 1-n-butyl-2,3-dimethylimidazolium bistrifluoromethanesulfonylimide ($BMMI^+$ $TFSI^-$) and Zhang *et al.* 1-ethyl-3-methylimidazolium trifluoromethanesufonate (EMI-Tf) as the ILs. Lithium is added into the electrolyte by adding separate lithium salt and dissolving it [60], or as a cation with the anionic species of IL [58]. These electrolytes are on the level of commercial and best available GPEs. [58]

The difficulties of ILs include the high reactivity with the electrode, but this effect is reduced because the host matrix already forms a stable SEI layer with the electrode. Additionally, small amounts of EC, PC, or mesoporous fillers have been reported improving the mechanical and electrochemical properties of GPEs with ILs [37]. ILs are not only suitable for electrolytes, but they have also been tested in electronic devices such as, electronic double layer capacitors, dye-sensitized solar cells, and actuators [61].

3.2 Inorganic Solids

Inorganic solid electrolytes are often called lithium ion conductors (LICs) and they can be either single- or polycrystalline. The conducting phenomena of LICs is based on disorder in the crystal lattice, where an atom is missing from its lattice site, or an atom is at the wrong or interstitial lattice site. The requirements for a feasible LICs are the same as every other solid electrolyte. The common problem with the reported inorganic materials is that the compound either possess high electrochemical stability window or high Li-ion conductivity, but not both. Luckily, inorganic solid electrolytes often possess Li transference numbers close to unity, which makes the study of these materials worthwhile. [62]

3.2.1 Perovskites

A common LIC is an A-site deficient perovskite (ABO_3) *e.g.* $Li_xLa_yTiO_3$. Perovskites often exhibit decent conductivities, because the A-site vacancies offer a good pathway to Li-ions. However, the disordering of the lithium, lanthanum, and the vacancies along the c-axis limit the conductivity. The ratio of lithium and vacancies affects the conductivity of these materials greatly, optimal value being around 0.44 – 0.45. This particular perovskite however, suffers from high reactivity towards metallic lithium, which reduces the Ti^{4+} cations and increases the electrical conductivity of the perovskite [63], thus the self-discharge rate of the cell. [62]

3.2.2 Superionic conductors

The second group of LICs is the Li super-ionic conductor (LISICON) type phosphates, for example simple $LiTi_2(PO_4)_3$ and $LiZr_2(PO_4)_3$. Initial interest towards these compounds arises from high conductivity in the bulk phase. However, these electrolytes also suffer from low electrochemical stability and from low grain boundary conductivity [62]. The $LiTi_2(PO_4)_3$ exhibits conductivity of 10^{-5} S cm^{-1} [64], but some more substituted LISICON type materials such as $Li_{1.4}Al_{0.4}Ge_{1.6}(PO_4)_3$ (LAGPO) exhibit the conductivity of $1.22 \cdot 10^{-3}$ S cm^{-1} at room temperature [65]. Neither of these electrolytes are stable towards lithium since in the presence of metallic lithium, the Ti^{4+} cation reduces to Ti^{3+}, causing the electric conductivity of the electrolyte to increase. However, LAGPO could be used with some other negative electrode such as lithium titanate, which has higher working potential.

3.2.3 Garnet structures

The third group of LICs are the garnet like structures (ideal composition $A_3B_2(XO_4)_3$, where A, B and X are eight, six and four oxygen coordinated cations, respectively). The amount of lithium per chemical formula varies greatly. The garnet structures can host either 3, 5, 6 or 7 Li-ions per unit cell. There has been plenty of discussion as to how the lithium is actually coordinated in the garnet structure, but nevertheless general trend is that higher lithium content up to 7 in chemical formula is preferable for the optimal conductivity [66]. One of the highest room temperature conductivities for the garnet structures is $Li_{6.5}La_3Nb_{1.25}Y_{0.75}O_{12}$, synthetized by Deviannaporaani *et al.* [67], which exhibited conductivity of $1.02 \cdot 10^{-3}$ S cm^{-1} at room temperature. The optimal lithium content in formula was also studied and it was find to be around 6.5 - 6.7 per chemical formula [67], which is in correlation with other garnet structures varying from 6.5 to 7 formula units [66].

3.2.4 Sulfide based Conductors

Recently a new group of sulfide based lithium superionic conductors have emerged. They exhibit extraordinary high conductivities well over the limit of $1 \cdot 10^{-4}$ S cm^{-1} and large potential windows. Kamaya *et al.* [68] were 1st to report $Li_{10}GeP_2S_{12}$ (LGPS), with high conductivity of $0.012 \cdot 10^{-3}$ S cm^{-1} and wide potential window (0 - 5 V).

Other reported materials are $Li_7P_2S_8I$ [69], germanium doped Li_3AsS_4 [70], glassy - ceramic P_2S_5 – Li_2S [71], and $Li_{9.54}Si_{1.74}P_{1.44}S_{11.7}Cl_{0.3}$ (LiSiPSCl) [72], with conductivities of 0.63, 1.12, 17, and 25.3 $\cdot 10^{-3}$ S cm^{-1}, respectively. The LiSiPSCl synthetized by Kato *et al.* [72] exhibits the highest Li conductivity of all reported solid electrolytes and in addition displays excellent cycling performance even if the cell is cycled with high current densities (18 C, in the $LiCoO_2$ | LiSiPSCl | Li_2TiO_3 cell, with 100 % Coulombic efficiency). The conductivity phenomenon arises from 1D and 3D pathways in the crystal structure (Figure 16). In addition, replacing the germanium in $Li_{10}GeP_2S_{12}$ makes this material substantially cheaper to manufacture. [72]

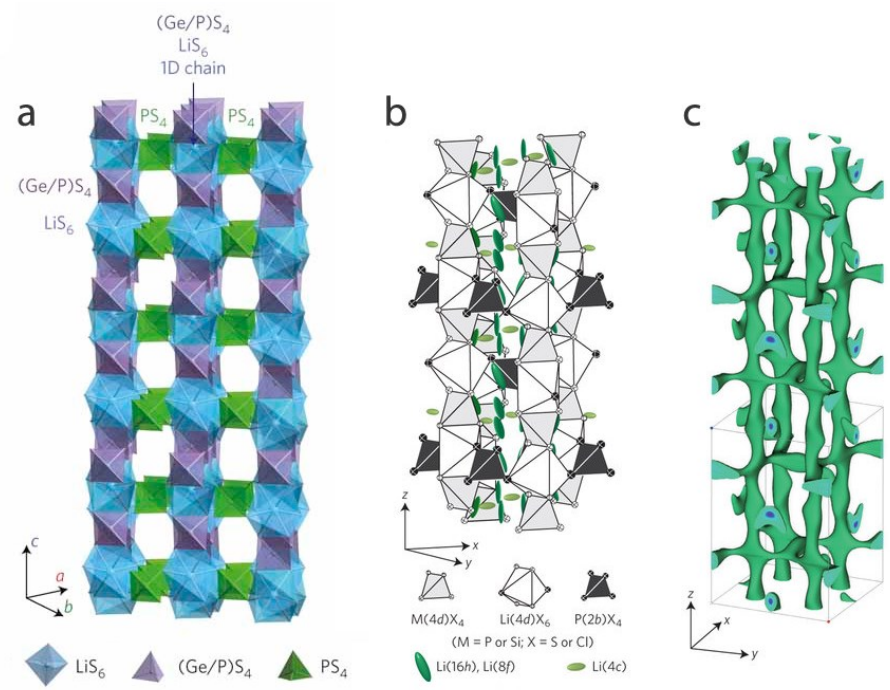

Figure 16. Crystal structures of the LGPS (a) and LiSiPSCl (b) and the calculated nuclear distribution of Li atoms in LiSiPSCl (c). The conductivity in LGPS occurs along c-axis 1D channels in zig-zag fashion. In LiSiPSCl 3D conductivity arises from three interstitial lithium sites, where sites Li(*16h*) and Li(*8f*) are responsible for 1D conductivity along c-axis and Li(4c) for the 2D ab-plane conductivity. [68,72]

However, the LiSiPSCl was not stable against lithium, since Coulombic efficiency during the first cycle was only 39 %, which indicates the formation of surface layers. Additionally the energy densities of tested battery devices ($LiCoO_2$ | LiSiPSCl | Li_2TiO_3) is fairly low (17.6 Wh kg^{-1}), because of the use of very thick separator and filler materials. Energy density could in theory be increased by fabricating a thin separator and creating a uniform electrode surface. Kato *et al.* [72] propose that if a

thin separator layer of 25 μm could be fabricated it would increase the energy density drastically.

3.2.5 Lithium Phosphorous Oxynitride

Lithium phosphorous oxynitride (LiPON) is a glassy amorphous solid-state electrolyte developed by Oak Ridge National Labs and it is the most common solid electrolyte. It was originally deposited by sputtering Li_3PO_4 in N_2, but LiPON has also been deposited by pulsed laser deposition [73], metal-organic chemical vapor deposition [74], and with ALD [36,75–77]. Naturally, ALD is the best at creating pinhole free films out of these techniques. The composition of LiPON varies from $Li_{3-x}PO_{4-y}N_y$, which is greatly affected by the deposition method. Additionally, the nitrogen doping improves the conductivity of the Li-ions relative to Li_3PO_4. Also small amounts of boron have been proven to enhance the chemical properties [78]. The conductivity of LiPON in room temperature is around 10^{-6} S cm^{-1}, which could use an improvement. Additional advantage of LiPON is its negligible reactivity with lithium metal, since its electrochemical stability range is from 0 to 5.5 V [79]. LiPON has also been successfully used as a passivation layer for organic electrodes to improve their stability in presence of liquid electrolyte [5]. Other amorphous glass electrolytes also exists *e.g.* Li_3N, Li_2S, or Li_2S-SiS_2-P_2S_5, but they are limited by low electrochemical stability and/or by their conductivity compared with LiPON [37].

3.3 Comparison

When looking solely at thin film or microbattery applications all of these solid electrolytes are not that suitable, because the layers need to be extra thin and pinhole free. In addition adhesion and contact between solid-solid interfaces may be difficult to achieve, in non-laboratory scale cells. However, because the electrolyte layer can be very thin, lower lithium ionic conductivities can be feasible. For example a 1 μm thick electrolyte layer with the conductivity of 10^{-5} S cm^{-1} exhibits resistance of 10 Ω cm^{-2}, which is acceptable for thin film microbattery applications [37]. Another interesting parameter in solid electrolytes is the activation energy of the cell. Activation energy arises from the energy needed that ion needs to hop from an occupied site to unoccupied one. A lower activation energy provides the most stable

ionic conductivity in different temperatures. High activation energy causes the localization of carrier ions, thus lower conductivity [70]. One last parameter is the transference number, which gives information about the high-rate performance and the power output of the battery [80]. Low transference number may also induce the growth of dendrites in Li-metal cells [81]. Conductivity, transference number, the electrochemical stability window, and the activation energy of several solid electrolytes are presented in Table 1.

Table 1. Comparison between SPE, GPE, inorganic and liquid electrolytes. * = The transference number of inorganic solids is close to unity, while organic liquid electrolytes usually exhibit t_+ values from 0.2 to 0.5 [63].

Electrolyte	Type	Conductivity in RT (S cm^{-1})	Li transference number (t_+)	Activation energy (eV)	Stability window vs. Li (V)	Ref.
$LiPF_6$	Liquid	$1 \cdot 10^{-2}$	0.40	0.145	4	[82]
PEO based	SPE	$1.1 \cdot 10^{-4}$	0.55	0.045	> 5	[81]
PVDF-HFP	GPE	$1.03 \cdot 10^{-3}$	N/A	0.12	5	[56]
PVDF-HFP / LiTFSI	ILGPE	$1.11 \cdot 10^{-3}$	0.44	$4.8 \cdot 10^{-5}$	5	[83]
$La_{0.5}Li_{0.34}TIO_{2.94}$	Perovskite	$0.7 \cdot 10^{-3}$	N/A*	0.35	Unstable	[84]
$Li_7La_3Zr_2O_{12}$	Garnet	$1.02 \cdot 10^{-3}$	N/A*	0.31	5	[67]
$LiAlGe_2(PO_4)_3$	LISICON	$1.22 \cdot 10^{-3}$	N/A*	0.32	Unstable	[65]
$Li_{10}GeP_2S_{12}$	Sulfur	$12 \cdot 10^{-3}$	N/A*	0.25	5	[68]
LiSiPSCl	Sulfur	$25 \cdot 10^{-3}$	N/A*	0.24	Unstable	[72]
$Li_{2.4}PO_{2.2}N_{0.61}$	LiPON	$1.0 \cdot 10^{-6}$	N/A*	0.55	> 5	[85]

Many of the pros and cons of these materials are already discussed in their respective chapters. The overall trend is that inorganic crystalline materials offer the highest conductivities, but they are rather brittle and adhesion with the electrode is often a problem. When the solid electrolyte decomposes, the side products will stay at the interphase, usually blocking the reactions, which might be fatal for already poor surface kinetics. In addition, some may suffer from weak thermodynamic stability. [86]

During the cycling of the battery, the electrolyte needs to be stable towards both electrodes, thus the voltage limit of 5 V vs Li/Li^+ arises from currently the best cathode materials utilized [37]. Only with high voltages, high energy densities are achievable. Even if the electrolytes such as LiSiPSCl, can be considered unstable vs. lithium, many

of these inorganic materials are still feasible in batteries using alternative anode materials such as lithium titanate, where the cell operates at lower voltages [72].

When designing a new electrolyte, the impact on the environment should always be considered. All the new materials should be cheap, sustainable, and recyclable. However, the electrolyte is only one of the components in the battery. The environmental factors need to be considered with every component. Currently, electrode materials are dominated by inorganic oxides. They are made of rare metals and the purification of them is often energy intensive, therefore harmful for the environment. The following chapter will discuss the new emerging organic electrode materials, which are often abundant, relatively affordable, and their synthesis is far less energy intensive. [87]

4 ORGANIC ELECTRODE MATERIALS

The first report of organic electrode material dichloroisocyanuric acid was in 1969 by Williams *et al.* [88] Organic electrode materials were largely forgotten for many decades since the inorganic electrode materials developed more rapidly. Mainly because the organic compounds exhibit much poorer electrochemical performance and cyclic stability, but many improvements have been made since [89]. Currently organic electrode materials are seen as a viable option to inorganic materials, due to their abundance, price (no expensive metals), high capacities, safety, and recyclability [6]. The organic electrode materials can fit both the positive and negative electrode sides and their electrochemical properties are highly tunable. Functionalization of the molecules allows the tuning of redox potential, thus the cell voltage. In addition the capacity, solubility, crystal structure, electron transfer rates, ionic conductivity, and the mechanical properties of the organic materials are tunable. The organic electrodes can be in theory cycled with high current densities, because the redox reactions of these materials are based on conversion reactions rather than intercalation reactions [90]. The organics are also applicable to the microbatteries, since they have a strong film forming ability, are flexible, printable, and even transparent [4]. Furthermore, organic electrode materials are not ion specific, which allows the design of sodium, magnesium, multivalent and dual-ion batteries in addition to conventional LIBs [87].

There are a number of excellent reviews that report on a wide variety of different organic electrode materials [87,90–92]. Thus, this chapter will not focus on introducing the different organic electrode materials but rather on the underlying redox and lithium storage mechanisms of carbonyl compounds and how the electrochemical properties can be altered by the functionalization of the molecules. Carbonyl compounds are believed to be most promising out of all organics since they simultaneously have chance to achieve high potential, energy and power density, and good cycling stability. Sulfur and nitroxyl radical based organic compounds are also a rather established branch of organic electrode materials, but they are not discussed in this chapter.

4.1 Redox Mechanism

The redox mechanism of inorganic compounds is based on the change of valence state of the active transition-metal, but for organics the redox mechanism is based on the change in the charge state of the carbon, nitrogen, oxygen, or other heteroatom in the structure [4]. During the lithiation reaction, the Li-ion is bound to the lone pair of electrons of the oxygen, nitrogen, or sulfur, resulting in charge transfer between lithium and the organic electrode. The lone electron pair is highly active, which results in relatively high potential for Li-ion insertion/extraction [93]. The system usually remains stable through conjugation or aromaticity. Häupler *et al.* [90] divided carbonyl based organic electrode materials into three groups based on the stabilization mechanism of the anion (Figure 17).

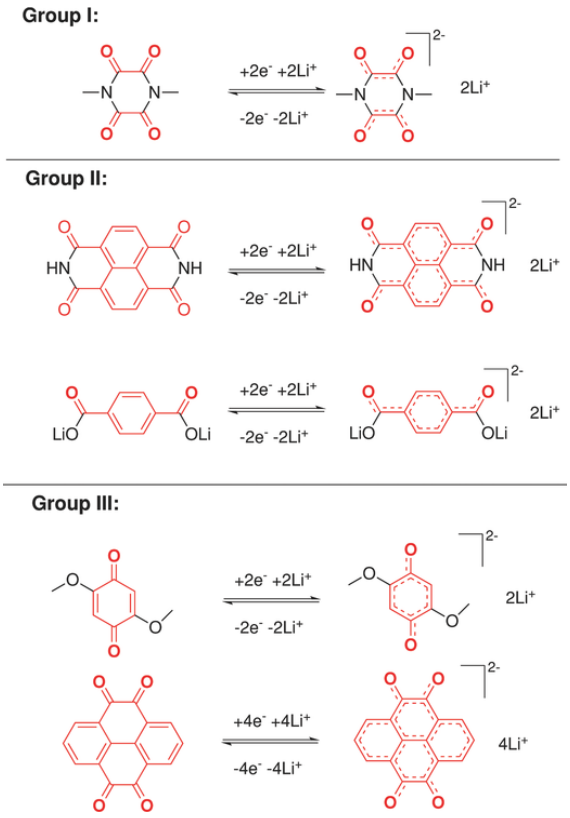

Figure 17. Carbonyl based organic active materials, categorized based on the anion stabilization mechanism. In group I, the molecules form stable enolates after reduction. Group II comprises the compounds that are derived from aromatic carbonyls. Group III is a mixture of groups I and II, but an additional aromatic stabilizing structure is formed upon reduction. [90]

As seen from Figure 17 the molecules can exist in both their normal and negatively charged state and they go through multiple-electron reactions. The storage mechanism is discussed later on. Organic electrodes can be classified to n-, p-, or b-type organics.

The n-type arises from the most typical case where the neutral state (N) is reduced to negatively charged state (N^-), whereas the p-type materials transform between the positively charged state (P^+) and the neutral state (P). The b-type (bifunctional) organic material is the mix between both of these which means it can go undergo reactions from neutral (B) to B^+ or B^-. The b-type organics can function as both the cathode and the anode in the cell [92]. For example Chen *et al.* [94] reported tetralithium salt 2,3,5,6-tetrahydroxy-1,4-benzoquinone ($Li_4C_6O_6$) that can be both reduced to $Li_2C_6O_6$ and oxidized to $Li_6C_6O_6$, which allows the construction of the whole battery based on a single material. However, the working potential of this battery is still rather low (1.8 V) and unacceptable for any serious application. The n-type materials are more appropriate for actual applications since they do not consume the electrolyte during the redox reactions. [4]

Whether the molecule is suitable for anode or cathode (negative or positive electrode, respectively) is decided by its Li-ion insertion/extraction potential vs. Li/Li^+. Usually, materials exhibiting voltages above 2.0 V can be considered cathodes and below the 2.0 V function as anodes. Carbonyls as already seen before, exhibit wide range of potentials, which make them feasible for both anodes and cathodes [93]. However, the electrochemical properties can be altered by modifying the aromaticity, conjugation, and by adding heteroatoms into the structure.

4.2 Aromaticity and Conjugation

Hückel's rule (4n + 2) of aromaticity is the basic rule for aromaticity in the field of organic chemistry. Clar's theory is an expansion of Hückel's rule of aromaticity, better known as aromatic π-sextet rule. The theory explains aromaticity in more complex cyclic molecules. It states that the structure with the most Clar sextets (six carbon atom rings in between the benzene rings) and with only single bonds is the most aromatic [95]. Aromaticity is closely connected to the voltage that the electrode exhibits during redox reactions. The lithiation process occurs through the carbonyl group, which is tightly connected to the carbon skeleton. The resulting negative charge will be delocalized over the whole aromatic system. Consequently, this means that through the modifications to the carbon skeleton the lithiation voltages can be affected [93]. Furthermore, the lithiation voltage is directly affected by the energy of the lowest unoccupied molecular orbital (LUMO), since LUMO is occupied during the lithiation.

Low LUMO energies indicate an increase in reduction potential of organic electrode materials [96]. When the reduction occurs, an electron is added to the LUMO orbital of organics. The higher the energy of the LUMO orbital is, the more difficult it is to reduce the molecule [97]. Energy of LUMO can also be affected by substituting electron withdrawing or donating groups to the redox active part of the molecule, which is discussed later on.

Wu *et al*. [96] studied the correlation between the voltage and the aromaticity (a π-conjugated system) of carbonyl compounds with density functional theory (DFT) computations. They designed six molecules with maximum aromaticity according to Clar's theory and by adding carbonyl groups to optimal positions in the parent molecule (Figure 18).

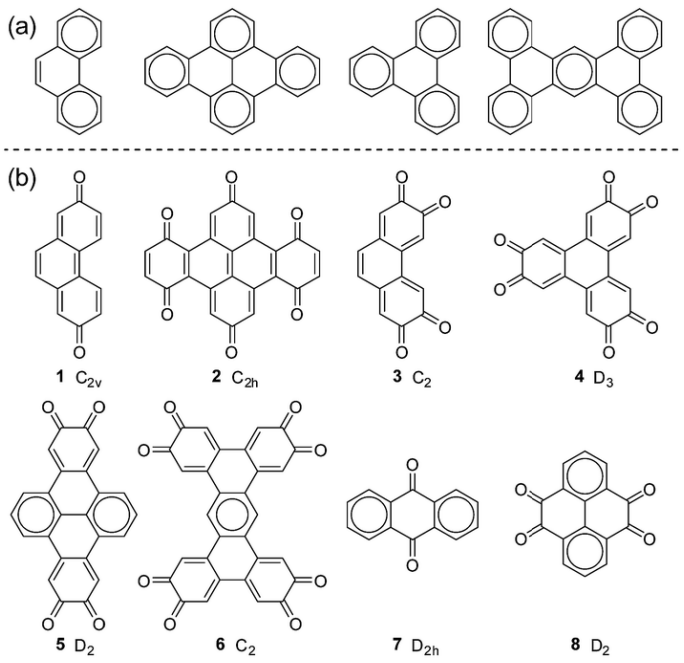

Figure 18. Designed molecules by Wu *et al.* Where in (a) are the full Clar polycyclic hydro carbons, used as a parent molecules. In the (b), the designed molecules 1-6, and 7-8, as a proof of the concept, to verify the results from the DFT calculations. [96]

Out of these concepts, number 3 shows a relatively high discharge capacity of 403 mAh/g with an average voltage of 3.08 V, and number 4 shows a high energy density of 1386 Wh/kg. However, these molecules have not been synthetized experimentally. To inspect the voltage gain from aromaticity an index called ΔC_{2Li} was introduced. The index describes "the average change of Clar sextet numbers when two Li atoms

are attached to the organic electrode material" [96]. A clear correlation between the index and the reduction voltage of the organics was found, such that with more positive index values, higher voltages were observed (Figure 19). Considering the Clar sextets is therefore important when designing new organic positive electrode materials. Despite the obvious advantages of aromatic systems, there are some drawbacks. Multiple aromatic rings has a lot of excess carbon in the structure lowering the gravimetric capacity of the electrode. Many of the chosen organics exhibit multiple charge/discharge slopes (Figure 19), since slightly different redox reactions are possible. This causes some of the materials to operate in wider voltage range, which is not ideal for actual battery applications [96].

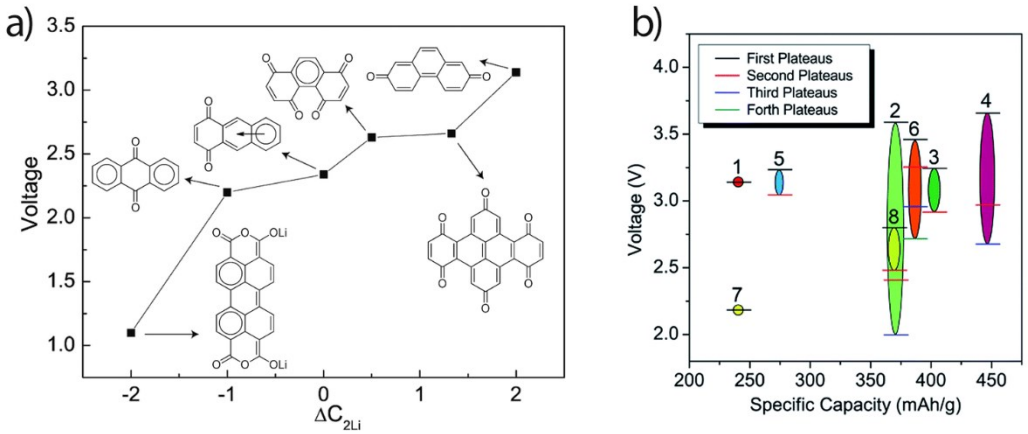

Figure 19. Correlation between the index ΔC_{2Li} and calculated reduction voltage. In b) the variance in the reduction voltage between the molecules. The corresponding molecules 1-8 are the same as in Figure 18. [96]

Optimal position of carbonyl was also studied by Gottis *et al.* [98] on the dihydroxyterephthaloyal system. When the system was switched from para to ortho-position (carbonyl groups from opposite sides to next to each other) the potential increased 300 mV. The same increase in potential was also observed by Wu *et al.* [96,98] and Hernández-Burgos *et al.* [97]. They both attributed this property to the binding energy of Li-ion. In their study, organics with the lowest LUMO energies had the highest Li^+ binding energies. The large binding energies help to stabilize the forming anion. Furthermore, the potential of the electrode can also be affected by substituting hetero atoms, rings, or additional functional groups to the carbon skeleton which is discussed in the following chapter [93].

4.3 Heteroatom Substituent

Multiple studies have suggested that substituting carbon with a more electronegative atom or by introducing additional more electronegative groups can be utilized to lower the reduction potential of the organics. Theoretical DFT studies were carried out by Hernández-Burgos *et al.* [97] where the effects of multiple substituents were reported. In the study, benzene and 5-membered ring were substituted with heteroatom, S, O or NH in this case, also the position of the heteroatom was considered (Figure 20.).

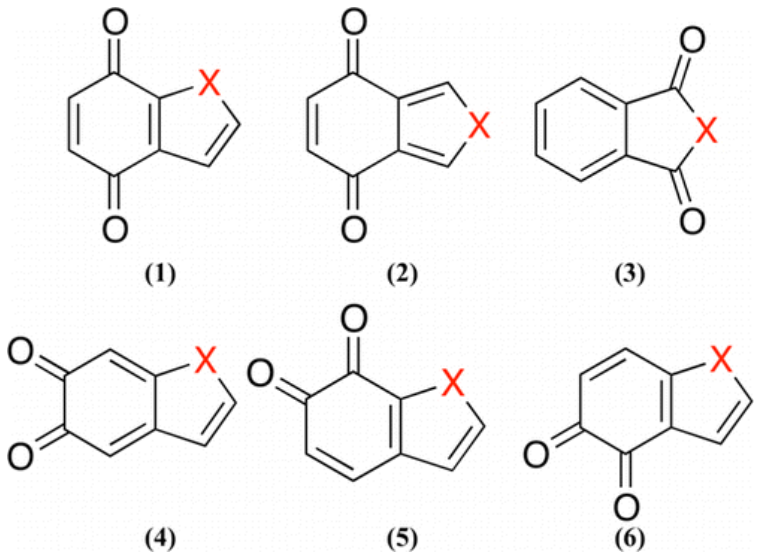

Figure 20. Organic molecules used to study the effect of the heteroatom in the ring. X was either sulfur, oxygen or nitrogen. [97]

All of the heteroatoms are more electronegative than carbon, thus in theory yielding higher reduction potential. The highest potential are obtained when sulfur was applied as the heteroatom. However, oxygen and sulfur were relatively close to each other, with both exhibiting similar LUMO energies. Organics motifs with nitrogen heteroatom display the lowest reduction potential and the highest LUMO energies and band gap, respectively. [97]

Similar experimental results were reported by Liang *et al.* [99]. They modified the carbon skeleton of the anthraquinone (AQ, Figure 18 molecule 7), by switching the benzene rings by the side of AQ with furan, pyridine, or thiophene. The familiar trend with LUMO energies and the reduction potential is observed. The highest momentary potential (2.75 V vs Li/Li^+) was achieved with pyridine substituent, but it had the lowest available capacity. Thiophene rings provided modest, but the most stable enhancement in electrochemical performance, by retaining the two-phase reaction

kinetics, increased potential (from 2.3 V to 2.5 V vs. Li/Li^+) and providing slightly better cyclability. AQ with furan rings had greatly improved high rate capabilities, cyclability, and increased reduction potential (two plateaus with 2.6 V and 2.3 V vs Li/Li^+), but the kinetics of the reaction were negatively altered, with two two-phase reactions.

4.4 Additional Functional Groups

Reduction voltage can also be affected by adding a functional group to the molecule, which is either electron-withdrawing group *e.g.* bromo, nitro or cyano, or an electron-donating group *e.g.* amine, hydroxyl, or alkane [93]. The withdrawing groups draw electron density from the π-conjugated system, which raises the potential, because it is now easier to add electrons to that orbital. The electron donating groups give electron density to the π-conjugated system, lowering the reduction voltage. Park *et al.* [100] studied the effect of the functional groups on sodium terephthalate (NaTP). The benzene ring was substituted with an amine, bromine, or nitro group and their potential was measured vs. Na/Na^+ pair (Figure 21).

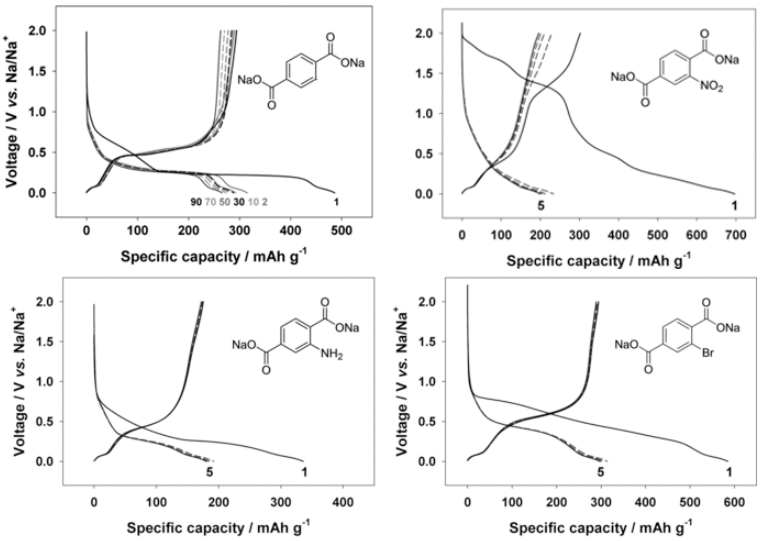

Figure 21. Electrochemical performance of NaTP substituted with NH_2, Br and NO_2. [100]

The electron donating amine group lowered the average reduction voltage, while the electron withdrawing halogen group bromine increased the potential, as expected, resulting in 0.19 V difference in quasi open-circuit voltage (QOCV). The effect of the nitro group was somewhat different. During the insertion of sodium ions, the nitro

group accepts first two sodium ions, followed by the typical reaction with carboxylate accepting two more ions. The insertion of sodium ions to the nitro group is in theory reversible, however a loss in capacity was observed during cycling. [100]

The shape of the charge/discharge curve is an important factor when looking at the performance of the cell. NaTP exhibits a single plateau while all the functionalized compounds have some degree of slope. Typically pure two phase reactions produce a flat plateau ($LiFePO_4$), while one phase reactions produce a slope ($LiCoO_2$). In addition slope or multiple plateaus may form if the kinetics of the electrode are complex or multiple different redox reactions occur, respectively. In ideal situation, plateau is a flat or the slope is reasonably gentle across wide capacity area. A wide plateau is essential for drawing stable voltage out of the cell. [100]

Lee *et al.* [101] experimented with cathode material 2,3-diamino-1,4-naphthoquinone (DANQ, Figure 22). The charge/discharge curve of the cell, exhibited two two-phase reactions, but the potential difference was only 0.1 V. The notable improvement was on cell's cyclability and high rate capabilities compared to compound without amino groups (NQ). DANQ retained 80 % of its initial capacity over 500 cycles while NQ retained only 20 % over 100 cycles. DANQ cell delivered 47 % of its theoretical capacity while cycling at 20C, and retained its original capacity when current was decreased to original 0.2C. The NQ cell could not recover after high rate cycling. [101]

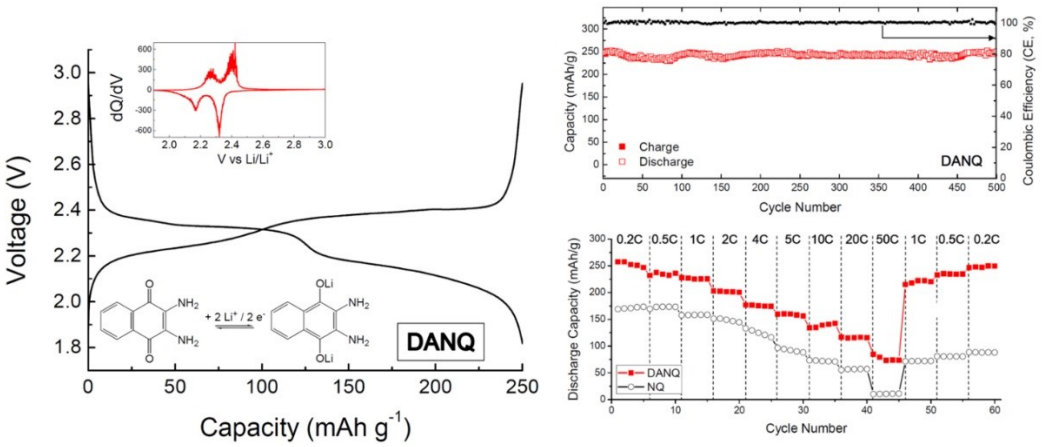

Figure 22. Electrochemical performance of DANQ [101].

The theoretical reduction potential of different groups was studied computationally by Hernández-Burgos *et al.* [97] and their result can be seen in Table 2.

Table 2. Effect of the different electron donating groups to the reduction voltage. Calculations were concluded by Hernández-Burgos *et al.* [97]

Molecule	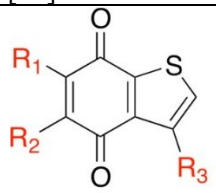 **R**= H, NO_2, CN, CF_3, OCH_3, CH_3, NH_2				
Substituent	Voltage (V vs. Li/Li^+)				
	R_1	R_2	R_1R_2	R_3	$R_1R_2R_3$
H	N/A	N/A	N/A	N/A	2.7
NO_2	3.5	3.4	3.7	3.1	3.9
CN	3.1	3.1	3.5	2.9	3.7
CF_3	3.2	3.0	3.3	3.1	3.4
CH_3	2.7	2.6	2.6	2.7	2.5
OCH_3	2.7	2.7	2.8	2.9	2.6
NH_2	2.4	2.4	2.4	2.7	2.4

The highest reduction potential was calculated to be 3.9 V vs. Li/Li^+ with NO_2 substituted into each position. The molecules with NH_2-group exhibited the lowest reduction potential which decreased the reduction potential below the non-substituted molecule. The position R_3 had the least effect on the reduction potential probably due to the conjugation which positions R_1 and R_2 were more directly connected. Position R_1 also had a slightly bigger impact on the voltage, due to the electronegative sulfur atom in the ring, lying on the same side of the molecule. These calculated voltage values probably predict only the most ideal situation, as seen from experimental studies the operating voltage drops drastically after the 1st cycle. Especially as already seen with nitro group (Figure 21), which was calculated to be the group with the highest potential increase, the voltage profile of the 1st and the 2nd cycle do not resemble each other almost at all. [97]

Other important features of the electrodes are the specific energy density and the specific capacity. Adding a functional group to the molecule that simply contributes or withdraws electrons from the conjugated system is just dead weight, because the change in voltage is not large enough to cover the loss in energy density [97]. This means that in gravimetric terms, the benefits of the functionalizing a molecule are

nonexistent. However, for example stationary applications the gravimetric capacity is not the most important feature. The volumetric capacity and the energy density are far more important characteristics in many applications and for example in the thin film battery research capacities are often presented as capacity or energy per area in contrast to capacity per unit of mass. However, if the gravimetric quantities are preferred, the functionalization should be done by directly modifying the carbon skeleton with heteroatoms, or in other electrochemically active areas, since this way capacity is not sacrificed [102].

The functional groups have however multiple purposes. Wan *et al.* [103] synthesized AQ, which is known to have problems with solubility with the electrolyte. The cycle performance and the operating voltage was greatly enhanced by the addition of sodium based functional group (SO_3Na). Pure AQ shows almost no capacity retention during cycling at 10C, while the AQ with 2 sodium groups still shows decent retention. In addition, the sodium groups also act as an electron withdrawing group, thus increasing the working potential of the cell. Therefore, the large sodium groups effectively stabilize the organic electrode by solving the dissolution problem and at the same time enhancing the potential.

4.5 Charge Storage

The intercalation phenomenon of inorganic electrode materials is rather sensitive to the size of the (de)inserted ion, which is one of the reasons why the development of sodium batteries has been slow. Organic electrode materials, due to their soft crystal structure, can often accept both lithium and sodium to the crystal structure. This allows the research concluded on sodium organic batteries to be directly applied to lithium organic batteries and *vice versa*. Only the voltage gap between the Li/Li^+ and Na/Na^+ pair is expected to be around 0.3 V lower for the sodium pair. [4]

4.5.1 Carbonyl Group

As already seen from Figure 17 the carbonyl groups have the critical role in determining the maximum theoretical capacity of the material. Based on this, the logical conclusion would be to maximize the amount of carbonyl groups present in the molecule. However, the experimental research on this topic has shown that increasing

the number of carbonyl groups to be over two, does not increase the capacity as much as was expected. This is probably due to the low utilization of the carbonyl groups, which means that the conjugated carbon skeleton of organic molecules cannot support the negative charge. Therefore, this problem can be solved by increasing the level of conjugation of the reduced molecule. [92]

What ultimately pushes the reduction reaction forward, is the amount of negative charge available. Liang *et al.* [104] proposed that HOMO's (the highest occupied molecular orbital) energy plotting and the change of thermodynamic energy might predict the percent of carbonyl utilization. The HOMO's of PHP, NTCDA, PTO, and $C_6O_6^{2-}$ were calculated during different reduction phases with DFT (Figure 23).

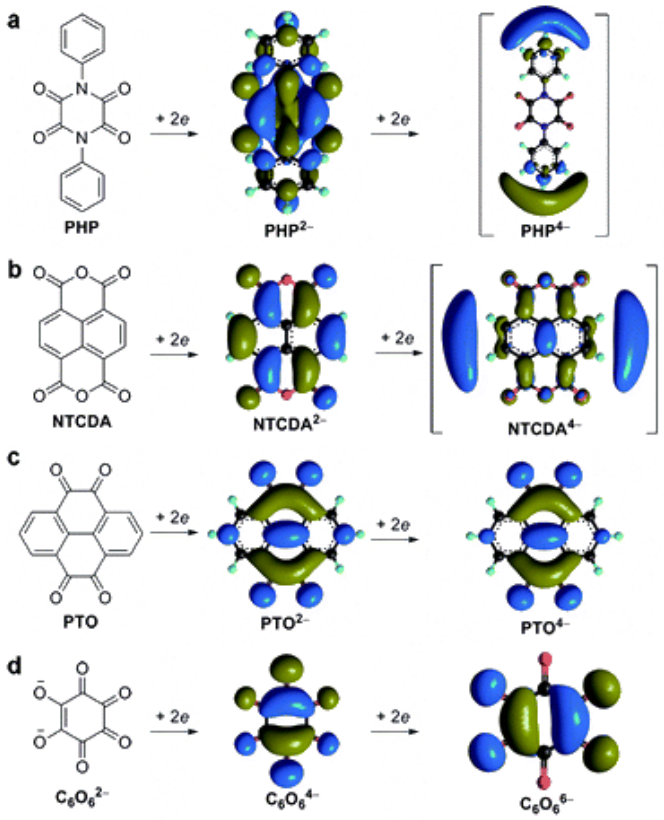

Figure 23. Plotted HOMOs of selected organic molecules. Experimental data suggests that a and b only go through two electron reaction and *c* and *d* four electron reactions. [104]

As seen from Figure 23, the four electron reaction HOMOs of PHP and NTCDA lay outside of the molecule, whereas the HOMOs of two electron reaction lay well inside the carbon backbone. If HOMOs are physically far away from the PHP and NTCDA molecules, they will not go through the four electron reaction which is also supported by the experimental data. In the case of PTO and $C_6O_6^{2-}$, the HOMO is at the reach of the molecules and four electron reaction is possible, which is also supported by the

experiments. Therefore, HOMO plotting can be a valuable tool, when the utilization of carbonyl groups is evaluated. [104]

The HOMO plotting however simplifies the model by leaving the cations out. If the calculations were performed on lithiated complexes, the results could not be replicated. To be able to inspect the lithiated complexes more accurately, the thermodynamic energy change from the intrinsic molecule to two and four lithiated states was calculated to the molecules (Figure 23). The PTO and $Li_2C_6O_6$ show similar energies when they are di/tetralithiated. Similarly, NTCDA and PHP show roughly equal energy for dilithiated states, but the energy change from the dilithiated to the tetralithiated state was smaller. This indicates that the driving force is smaller for the reduction reaction and it does not occur spontaneously. The HOMO plotting and thermodynamic energy change can therefore be powerful tools when new organic electrode materials are researched. [104]

4.5.2 Storage Mechanism

The position of the charge carrying cation in the crystal structure is a rather interesting topic. For example, Li_2TP have shown a capacity of ~2.3 Li-ions per organic molecule, which suggests that carbon backbone is an active part in the reaction [6]. In Li_2TP or Na_2TP, the cation bound to salt forming oxygen does not ideally take part in the redox reactions, because if it does, the crystal structure decomposes, which results in poor cycling capability [4]. The lithiated crystal structure of Li_2TP was calculated by Zhang *et al.* [105]. They proposed that the lithium is introduced in between of organic layers resulting in a slightly smaller unit cell (Figure 24). In case of Na_2TP results are fairly similar. Sk *et al.* [106] calculated that during the insertion of the sodium ions, the first sodium binds with the carboxyl group, and the second with the carbon backbone (benzene). The sodium ions simply cannot fit on the same site that lithium does, due to the larger ionic size of sodium (Figure 24). Even if the study of Zhang *et al.* did not accord for the carbon backbone binding of lithium, it is clear that Li_2TP displays the phenomena of the same kind as in Na_2TP to some degree, which will be discussed later on. [106]

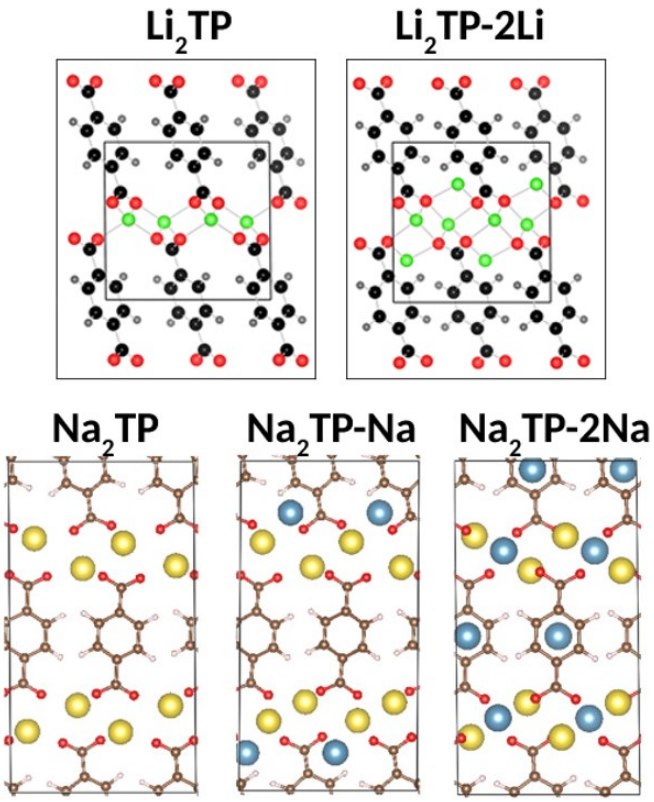

Figure 24. Different structures of Li_2TP and Na_2TP during the cation insertion calculated with DFT. While the sodium content is below 1:1 the sites next to carbonyl are filled. After the sodium content rises over 1:1 the carbon backbone site starts to fill. [105,106]

The storage mechanism of similar compound $Na_2C_6H_2O_4$ (Na_2DBQ) was studied by Wu *et al.* [107]. They propose a different storage mechanism for Na_2DBQ and for Na_2TP. The crystal structure of Na_2DBQ is fairly similar to Na_2TP, with alternating inorganic and organic layers. Their calculations imply that the inorganic layer hosts the storage sites and conducts the sodium ions, whereas the organic layer functions as the electron storage, conductor and a redox center. It is vital that the Na-O layer stays intact during (de)sodiation, even if the coordination environments of the atoms change drastically. According to their calculations, the distance between benzene rings expands up to ~0.5 Å upon sodiation, which causes the expansion of the lattice. Additionally, they reported that sodium ions do not diffuse from the inorganic to the organic layer, as Sk *et al.* [106] suggested with Na_2TP. In situ XRD (X-ray diffraction spectroscopy) of (de)sodiation also revealed that the reaction pathways were different for the first and the second cycles. During the first cycle, Na_2DBQ is directly sodiated to Na_4DBQ, skipping the Na_3DBQ phase (Figure 25).

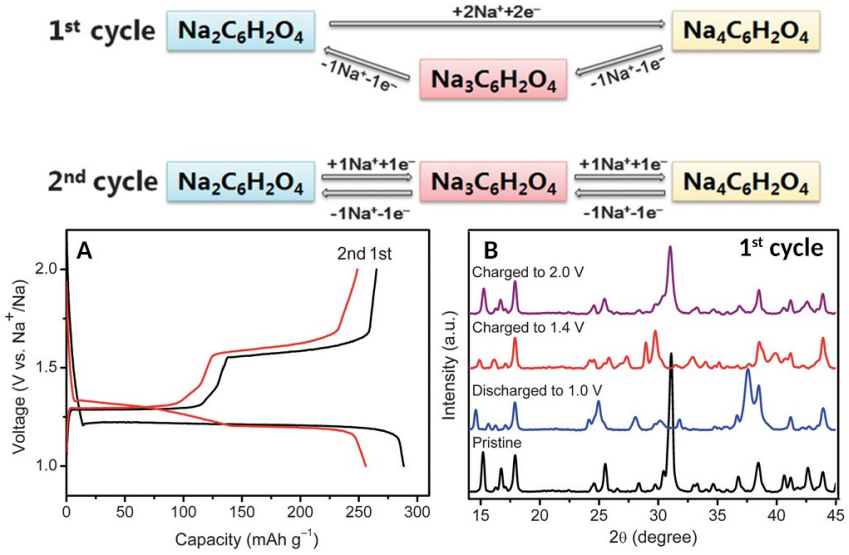

Figure 25. Reaction pathways during the first cycle and onwards. The changing shape of the charge/discharge curve is shown in A, and the change *in situ* XRD is shown in B. [107]

At Figure 25 during the 1st cycle, the direct change to Na_4DBQ is visible from both charge/discharge with only one plateau and from the *in situ* XRD data. In other words, Na_2DBQ goes through two-phase reaction during the first cycle and two two-phase reactions on the second cycle and onwards. The change in reaction pathways may be responsible for the irreversible loss at the cell, but the absolute reason what causes the different reaction pathways is still unknown. [107]

4.5.3 Excess Capacity

Graphite is currently widely utilized anode material in LIBs. It is common knowledge that the graphite possesses a relatively low theoretical capacity of 372 $mAhg^{-1}$, when the Li/C_6 complex is formed. However, recent research on nanographene has revealed that the actual capacity of these compounds is almost twice the theoretical capacity. While the mechanism is still unknown, the conclusion is that the carbon ring must be able to store more than one lithium ion. The abnormal excess capacity of organic electrodes has been reported to both lithium [108,109] and sodium [110] ion batteries. This excess capacity arises from the aromatic benzene rings of the electrode material.

Han *et al.* [111] studied the super-lithiation of NTCDA (Figure 23b) and show that the molecule is capable of accepting 18 Li-ions, resulting in capacity of 1800 $mAhg^{-1}$. During the discharge at potential 2.61 – 1.04 V, the NTCDA goes through the

usual carbonyl reduction with 4 Li-ions while retaining crystallinity. From 1.04 – 0.001 V, the carbon skeleton starts to accept seemingly extra Li-ions. During the discharge, the crystal structure decomposes and an amorphous phase starts to form, as was confirmed with ^{1}H NMR (proton nuclear magnetic resonance), XRD, and vacuum IR (infrared spectroscopy). The recovery of the crystal structure was not discussed in the article. Five distinct plateaus are seen in the voltage profile, which correspond lithiation of 1, 2, 4, 8, and 18 Li-ions (Figure 26). With higher C-rates Li-ions accumulate in to the structure, but with lower ones, full capacity retention is observed. These findings were compared with different aromatic and carbonyl based compounds, to see if the same kind of super-lithiation occurs (Figure 26). The capacity of these compounds were measured using the same procedure as in NTCDA, and calculated one was based on their proposed theory that each carbon in the aromatic ring can react with a lithium forming a Li_6/C_6 complex.

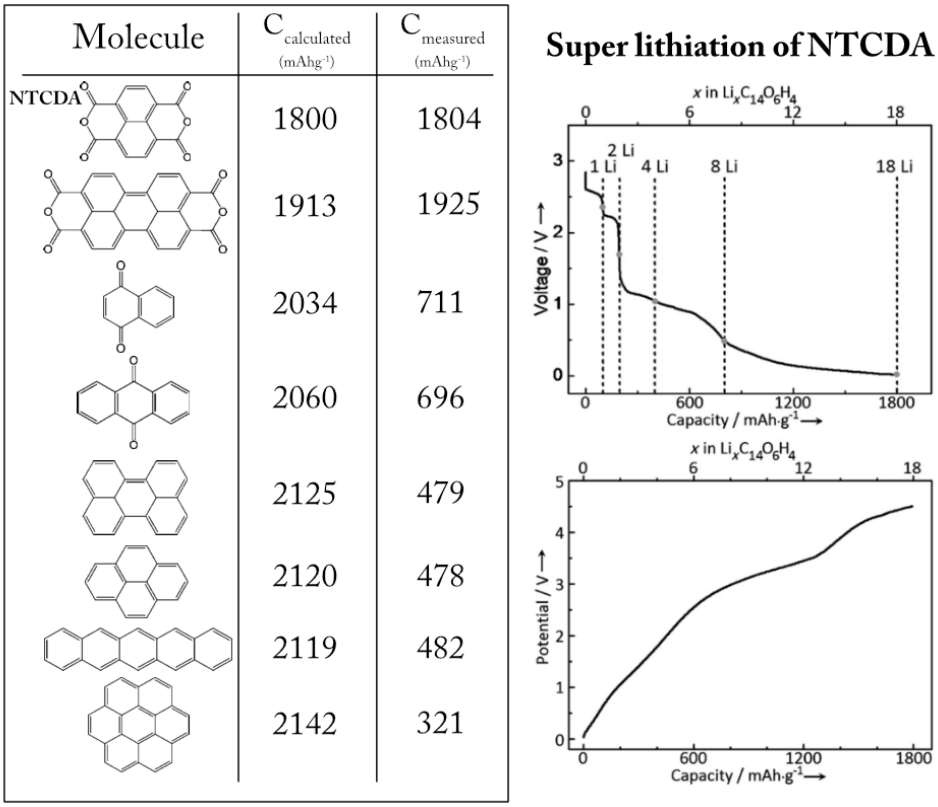

Figure 26. Molecules and their measured and calculated capacity. The calculated capacity is based on assumption that each aromatic ring can form C_6/Li_6 complex. The charge/discharge curves of NTCDA with super-lithiation are also shown. [111]

As shown in Figure 26, the super-lithiation does not occur in pure aromatic compounds and is not as prominent in the compounds containing only the carbonyl group.

Therefore, carbonyl and anhydride group has to have a crucial role in the ongoing mechanism due to the formation of higher oxidation states of the carbon in the ring [111]. To add to this list, Li_2TP and dilithium benzenedipropiolate are also shown to have super-lithiation capabilities, even without the anhydride group existing in the molecule [109]. For sodium, the super-sodiation is reported only for compounds with an anhydride group [110].

The actual capacity gained from the super-lithiation can be argued to be relatively hard to use in actual battery applications. The reaction is reversible, but the voltage needed to delithiate the structure is really high, for NTCDA 4.5 V vs. Li/Li^+ for the last lithium ions, resulting in a very low voltage of the actual battery. Nevertheless, knowing the origin of this phenomenon can be really useful in developing the doped graphite/graphene, and the hard carbon anode materials. [111]

5 GREENER BATTERIES

It has been estimated that by 2050 our annual energy consumption will be doubled from the current 14 TW to 28 TW. The increase in energy demand is equivalent to 10^{10} tons of oil annually for the next 40 years. This goal must be reached without increasing the CO_2 emissions. Multiple ways of generating green energy already exist: wind, tides, solar, biomass, and geothermal energy are all already applied or promising technologies. However, none of these energy sources are reliably available around the clock or they are geographically scarce. To gain any benefit of these renewable resources we need an efficient energy storage system. The current energy storage capacity covers around 1 % of the energy consumed, and 99 % of that 1 % is in form of hydroelectricity where water is pumped to a higher altitude. The future energy storage system must therefore be less costly and more efficient than hydroelectricity. LIBs are the most established battery technology, but the progress in developing LIBs has been slow and the research might be reaching the point of diminishing returns. Additionally, common LIBs include rare metals such as cobalt making them costly and energy intensive to produce in large scale. This chapter will discuss about closing the loop with current LIBs and discusses alternatives to the electrodes and possibility of moving onwards from lithium ion. [112,113]

5.1 LIB Recycling

The advantage of LIBs arises from their versatility. LIBs can be applied as batteries for small autonomous devices, portable devices, electric vehicles, and even for energy storage in the grid. But what would happen if the mass production of LIBs began this instant? To produce one 1 kWh LIB more than 400 kWh of energy is needed, which results in ~70 kg of CO_2 emissions, since the electricity used in such factories is often produced from fossil fuels. In comparison producing 1 kWh of energy out of coal releases only 1 kg of CO_2. This means that batteries have an ecological impact only after having been in use for hundreds of cycles. Therefore, the battery and electrode material production is one big contributor to CO_2 emissions and energy costs. Things would get even worse if the mass producing of batteries began, because the scarcer the element is in the crust of the earth; more energy intensive it is to purify. This raises the interest for the recycling of LIBs. [112]

However, the recycling of LIBs is not as simple as the recycling of lead-acid batteries (LABs) is. The recycling of LABs is simple and well organized (99% of the batteries are recycled in the U.S.), mainly because the components used by different manufactures are similar. On the contrary, the LIBs have a wide variety of shapes, different materials, and they are composed of multiple smaller cells (even up to ~5000 for Tesla's electric vehicle), while LABs are most often built out of a single unit. The active materials in LIBs are powders attached onto metal foil, which must be separated during the recycling process. [114]

The methods that are currently in the planning stage or applied to LIB recycling are pyrometallurgical recycling, intermediate recycling process, and direct recycling, which all have their pros and cons. A more detailed review of the working principles of these recycling techniques can be found in the report written by Dunn *et al.* [115]

To close the LIB loop, the materials produced from scrap batteries must be as cheap and as pure as the products refined from raw ore. What makes this more difficult, is that common electrode materials cobalt, nickel, and manganese are hard to separate without using expensive organic solvents. The impurities are difficult and energy intensive to get rid of and they are the reason why battery manufacturers often prefer to use new materials, since even the small impurities induce negative effects in the electrochemical performance of the battery. Currently, recycling industries usually only separate the really expensive metals (cobalt and nickel) and reuse the less expensive metals (manganese, iron, aluminum) in some applications that do not require as high purity as electrodes do. Hence, this leads to the question about the sustainability of metals utilized in LIBs. [116]

5.2 Sustainability of Rare Metals

Decreasing the usage of non-renewable resources *i.e.* limiting the use of metals that are not included in typical biomass is a mandatory goal for the greener future [117]. For example, 25 % of cobalt product goes into the production of LIBs and it is steadily increasing. In addition, cobalt may have far superior applications in other branches of electronics, where it is absolutely needed to achieve specific results, such as in permanent-magnetism. If the usage of cobalt in the battery industry were to continue, the "urban" mining of scrap batteries must be considered. Typical scrapped LIB

consists of 5-15 wt.% of cobalt, while in the crust the concentration of cobalt is 20 parts per million in average. Thus, cobalt is available in much higher concentrations in scrap batteries than in the crust of the earth. [112]

Substituting the expensive cobalt with cheaper *i.e.* more abundant elements such as Ni, Mn, Fe, and Al have become an attractive option and has already started to replace the long-standing industry standard $LiCoO_2$. For example $LiNi_{⅓}Mn_{⅓}Co_{⅓}O_2$, which is an excellent example of material where simple chemical modifications can improve both electrochemical performance and sustainability [112]. Furthermore, a rather promising recycling process has already been developed by Larcher *et al.* [116] for $LiNi_{⅓}Mn_{⅓}Co_{⅓}O_2$ batteries.

A greener solution would be to move onwards from pure cobalt based electrode materials, since the recycled battery materials often contain impurities, which have severe negative effect on the performance of the battery. Therefore, using alternative battery chemistries such as $LiFePO_4$, Li-S, organic, or Li-Air batteries are an attractive options, since the materials utilized in these technologies are largely recycled in nature. [112]

5.3 Alternatives for Lithium

By some estimations, if all the cars of the earth were converted to electric vehicles with 15 kWh LIB, the switch would consume up to 30 % of earth's known reserves of lithium [113]. Lithium deposits are divided into brines, pegmatites ($LiAlSi_4O_{10}$), and sedimentary rocks ($(Mg,Li)_3Si_4O_{10}(OH)_2$), where brine makes up 66 % of all lithium reserves. The lithium reserves are thought to be sufficient at least for the next century, even if a heavy adoption of electric vehicles takes off [118]. However, batteries are not the only application of lithium and the demand might exceed supply in the worst case scenario causing high fluctuations in the prices [119]. Therefore it is reasonable to look into alternatives.

Sodium is abundant and much cheaper element than lithium. It is part of the biomass, so it is recycled by the processes present in the nature. Using sodium permits also the use of aluminum current collectors instead of the copper ones, which ultimately cuts down the price and the carbon footprint of the battery. However, sodium is not without disadvantages. The electrochemical potential of Na/Na^+ pair is slightly higher, thus

resulting in a lower cell voltage. Naturally, the sodium ion is also heavier and larger, which results in smaller gravimetric capacities and larger volume expansion during cycling, which may cause the cell to degrade faster. Additionally, the common Li^+ intercalating inorganic metal oxides have not been wildly successful when the ion was switched to Na^+. However, with organic electrode materials, the Na-ion is basically interchangeable with lithium. Furthermore, sodium does not function well with graphite, but it does work well with hard carbons, which are often derived from biomass, such as apple or banana peels. [119]

Taking a wider field of view, rechargeable magnesium and aluminum batteries are also an attractive option. Magnesium has higher volumetric capacity than lithium, does not form dendrites, and is stable enough to handle in atmospheric conditions, which improves the safety. The biggest issues with magnesium ion batteries, are the sluggish reaction kinetics and the formation of passivating SEI, which Mg^{2+} cannot pass through [120]. The benefits of the aluminum ion battery arise from the same aspects. High capacity, due to three-valent ion, safety, and abundancy. Drawbacks have however been substantial: low discharge potential, low cycle life with high capacity decay. However, Lin *et al.* [121] have already produced a promising aluminum ion battery with high discharge potential and good cycling capabilities, which do give hope for these technologies.

5.4 Green Electrodes

If the goal is to build as green a battery as possible, the organic electrode materials are the way to go. For a long time, organic electrodes were forgotten due to the rapid development of the inorganic batteries, but as seen above, the sustainability of the inorganic materials is a controversial topic. The synthesis process is what makes the organic electrodes considerably greener. To produce high quality inorganic electrodes typically high temperature ceramic processes are used, while the organic electrode materials can be derived from ecofriendly processes and are recycled by nature. It can be argued that without a wider utilization of organic electrodes the European goal, which states that 50 % of the battery's weight should be recycled, is difficult to reach. An example of a recycling process can be found from Figure 27. [122]

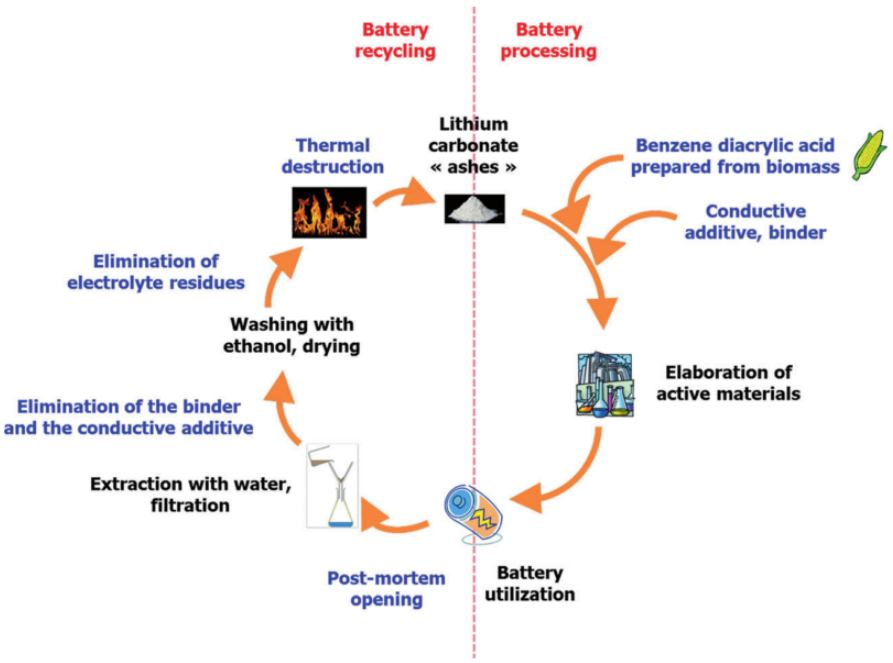

Figure 27. Recycling process of dilithium trans-trans benzenediacrylate ($BDALi_2$) developed by Renault *et al*. [122].

The $BDALi_2$ can be synthetized from all natural sources. After the battery utilization, it is opened and the components are separated based on their solubility on H_2O or ethanol. Separation based on solubility is overall simple and ecological process. The problematic part of their closed loop is the decomposition products of $BDALi_2$ formed during the battery cycling. These impurities make it impossible to reapply the recycled electrode material back to the battery, without advanced and expensive separation processes. Therefore, the most feasible solution is to thermally destruct the battery. Thermally decomposing the battery yields a pure enough powder of Li_2CO_3 the starting material for the synthesis. The thermal destruction of the compound naturally also yields CO_2, but since natural products are used to create the batteries no additional CO_2 is produced, thus this process is a closed loop. [122]

Currently organics are our strongest bet for the greener future. However, development and breakthroughs are still mandatory to overcome the low volumetric capacity, electric conductivity, and dissolution problems. Luckily with the organics, the structural diversity is massive, and even a small change can have tremendous impact on the electrochemical performance, as already seen in the previous chapters. Therefore, it is fairly certain that organics will have an impact on the energy storage systems, with the current LIBs or beyond them. [4]

EXPERIMENTAL PART

6 RESEARCH GOALS

In the experimental part, ALD and MLD are combined to fabricate novel thin films of organic lithium salts. These hybrid thin films are applied as the electrode in the cell. The ALD/MLD technique has already been shown to be feasible option to fabricate organic electrode materials [5]. However, the structural diversity of organic materials is immense and even a small change to the system's conjugation or addition of a functional group can have an impact on the chemical and the electrochemical properties.

The focus will be on five different organic molecules, which are analogous to a previously reported organic anode material Li_2TP [5,6]. These molecules are 2-aminoterephtalic acid (TPA2A), 2,5-dihydroxylterephtalic acid (TPA25OH), 2-bromoterephtalic acid (TPABr), 2,5-pyridinedicarboxylic acid (PDC25), and 3,5-pyridinedicarboxylic acid (PDC35). These organic compounds with the inorganic precursor LiTHD (THD = 2,2,6,6-tetramethyl-3,5-heptanedione) are employed as the ALD/MLD precursors. Currently, reports of lithium-organic hybrid thin films deposited with ALD/MLD are still limited.

The electrochemical properties of these lithium salts are measured (vs. Li/Li^+) in order to see which functional group is the most effective at tuning the electrochemical properties. The TPA2A and TPA25OH have electron donating groups of NH_3 and OH, respectively. In theory, these groups should decrease the reduction potential. The TPABr, PDC25, and PDC35 have electron withdrawing groups of Br, and N inside the aromatic ring, respectively. These groups should increase the reduction potential. However, with PDC25 and PDC35 the aromaticity and the conjugation of the system is also tuned, which has an additional effect on the electrochemical properties.

7 SAMPLE SYNTHESIS

7.1 Preparation of Precursors

Lithium precursors include but are not limited to Li(O^{t}Bu) (tertbutoxide), LiTHD and LiHMDS (lithium bis(trimethylsilyl)amide) (Figure 28). Li(O^{t}Bu) and LiHMDS are air sensitive, which makes them more difficult to handle. LiTHD was chosen because it is relatively stable, is easy to prepare in house, and in the previous study by Nisula *et al.* [5] on the Li_2TP, LiTHD was employed as the inorganic precursor. However, LiHMDS and Li(O^{t}Bu) are more reactive than LiTHD, which makes them more difficult to handle but they might react with the additional functional groups and possibly providing different crystal structures.

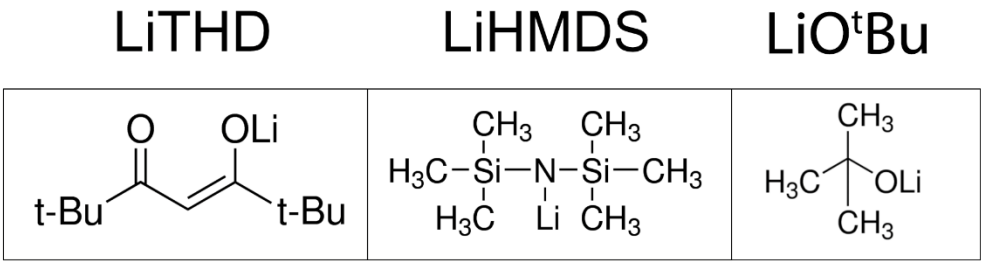

Figure 28. Lithium precursors for ALD employed in this stage.

The LiTHD precursor was prepared in house by dissolving 4.0 g of LiOH · H_2O (Alfa Aesar, 98%) into mixture of 45 ml of ion exchanged H_2O and 25 ml of 99.5 wt.% ethanol, some heating was required to get LiOH to dissolve completely. Additionally, 10 ml of HTHD (Tokyo Chemical Industry Co. Ltd.) was mixed with 20 ml of ethanol. The solution containing HTHD was added dropwise to the LiOH solution under constant stirring. A white precipitate was formed nearly instantly, making the stirring difficult. The precipitate was filtered and washed seven times with 20 ml of ethanol. The drying was done overnight at 110 °C directly in a sublimator to minimize the air-exposure of the compound. The compound was purified by sublimation at 190 °C. A white dusty powder condensed onto the cold inner tube of the sublimator, which was collected and used in the depositions (Figure 29).

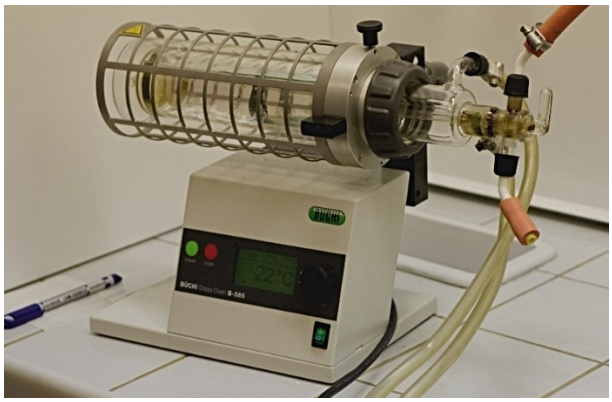

Figure 29. Sublimator and the unpurified LiTHD inside the vacuum chamber.

The functionalized TPA molecules were used as the organic precursors. More specific information about the purity and the composition can be found from Table 3.

Table 3. Organic precursors used in the depositions.

	Molecule	Purity (%)	Manufacturer	CAS
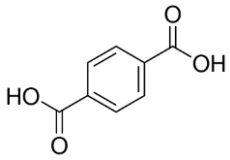	TPA	> 99	Tokyo Chemical Industry Co. Ltd.	100-21-0
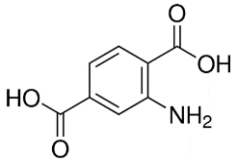	TPA2A	> 98	Tokyo Chemical Industry Co. Ltd.	10312-55-7
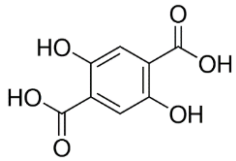	TPA25OH	98	Sigma-Aldrich	610-92-4
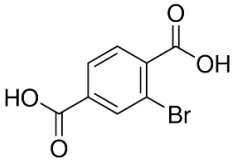	TPABr	95	Sigma-Aldrich	586-35-6
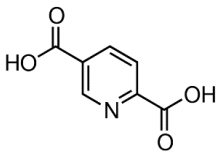	PDC25	96	Sigma-Aldrich	100-26-5
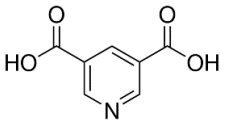	PDC35	> 98	Tokyo Chemical Industry Co. Ltd.	499-81-0

7.2 ALD/MLD Depositions

The ALD/MLD depositions were carried out in an F-120 flow-type hot-wall ALD reactor (ASM Microchemistry Ltd.) on Si(100), borosilicate glass and stainless steel substrates. The borosilicate glass and the steel substrates were cleaned in the ultrasonic bath while the silicon substrates were cleaned with compressed air prior to the use. The silicon substrates were used for all depositions, the glass substrates were used to measure the optical properties, and the steel substrates were used for electrochemical characterization. The carrier and purging gas in the reactor was nitrogen (>99.999 %, 300 sccm), produced from air (Schmidin UHPN 3000) or from N_2 gas cylinder.

The precursors were sublimated inside the reactor at various temperatures (Table 4) and pulsed into the reactor at low pressure (2-3 mbar). The optimal sublimation temperature of each organic compound was determined by measuring the weight loss of the precursor boat before and after the deposition and by visual inspection of the quality of the films.

Since the scope of the materials is wide, and even if the materials resemble each other, each of these materials acted very differently during preliminary testing and it would require an extensive study to find the optimal growth parameters for each different compound. Therefore, it was decided that only TPA2A process was investigated thoroughly, since its preliminary results were the most promising. The rest of the materials were also deposited with the ALD/MLD, but the linear growth and the ALD window were not confirmed. The parameters used for each material for the steel and glass substrate depositions can be found from Table 4.

Table 4. Parameters used for the films, which were used to determine the optical and electrochemical characteristics. All the depositions used LiTHD as the inorganic precursor with sublimation temperature of 170 °C and with pulse/purge length of 6 s / 6 s.

Organic compound	TPA	TPA2A	TPA25OH	TPABr	PDC25	PDC35
Sublimation temperature (°C)	185	185	200	195	180	190
Deposition temperature (°C)	200	200	250	220	250	250
ALD/MLD cycles	400	400	400	400	400	400
Pulse/purge (s)	10/30	15/30	15/30	15/30	15/30	15/30

7.3 Battery Assembly

The thin films deposited on the steel substrate were applied as the working electrode in a CR2016 coin cell. Metallic lithium was used as the counter electrode. The films on steel substrates were dried in vacuum at 110 °C for overnight and transferred into argon filled glove box, with O_2 and H_2O levels being less than 1 ppm. The electrolyte used was 1 M $LiPF_6$ in 1:1 ethylene carbonate/dimethyl carbonate solution. The separator used was a glass fiber separator. A schematic of the battery assembly is shown in Figure 30. The assembled coin cells were let to stabilize for at least 6 hours or until the open circuit voltage was constant.

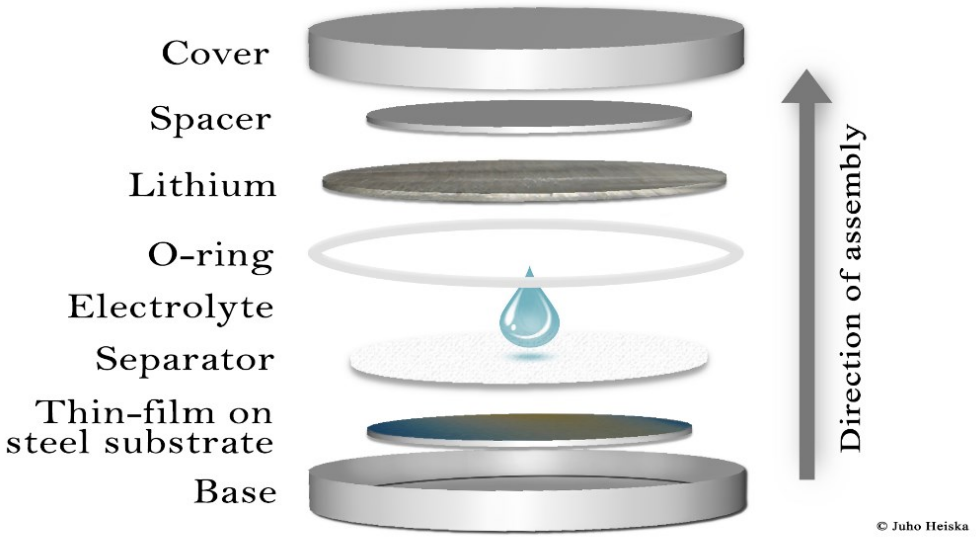

Figure 30. A schematic illustration of the assembly of a coin cell.

8 CHARACTERIZATION TECHNIQUES

8.1 X-ray Diffraction and Reflectivity

The thin films were characterized with grazing incidence X-ray diffraction (GIXRD) and X-ray reflectivity (XRR) with PANanalytical X'Pert Pro diffractometer. The X-ray source was Cu Kα radiation with a wavelength of 1.5418 Å. The crystallinity of the films was determined from the GIXRD data, with an incidence angle of 0.5° with 2θ angle of 5-60°. With low incidence angles, most of the X-ray reflections arise from the surface of the film rather than the substrate. The crystal phase of the film can be identifiable using powder diffraction databases. However, the proportion of peak intensities is often different and they can be slightly off-position. This is partly caused by the films not being completely polycrystalline and from any residual stress/strain caused by the lattice, since the ALD/MLD films are grown with layer-by-layer technique. Examples of crystalline and amorphous GIXRD diffractograms are shown in Figure 31.

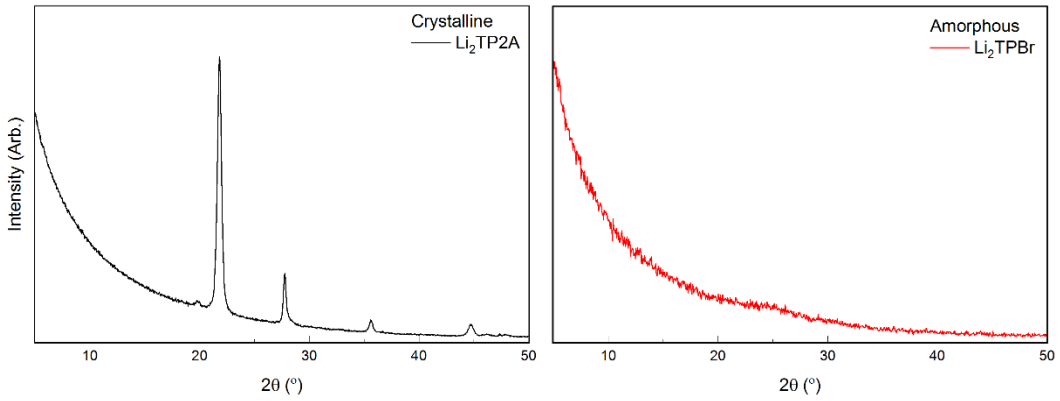

Figure 31. GIXRD diffractogram of crystalline Li_2TP2A and amorphous Li_2TPBr.

The crystal structures of the films were not solved with any refining methods. However, the minimum energy crystal structure of Li_2TP2A was resolved with Universal Structure Predictor: Evolutionary Xtallography [123] (USPEX) by professor Karttunen.

XRR was used to determine the films thickness and their density. The scan range was 0.12° – 2.0°. At every interface, a portion of X-rays are reflected to the detector. The interference of these partially reflected X-rays forms the oscillating reflection pattern.

The films thickness can be deduced from the period of oscillations and the critical angle. The thickness was computed with the program X'Pert Reflectivity. Both direct method and Fourier transform method was used and the average was used as the thickness. The critical angle is defined in the optics as the angle of incidence where total internal reflection occurs. From the reflection pattern, the critical angle was chosen to be at the incidence angle where the intensity is a half after the significant drop in intensity occurred. The XRR method can also be used to determine the roughness of the samples from the intensity and oscillation decay rate at higher angles. However in this study, the roughness of the films was not determined. An example graph showing what can be deduced from the XRR graph is shown in Figure 32.

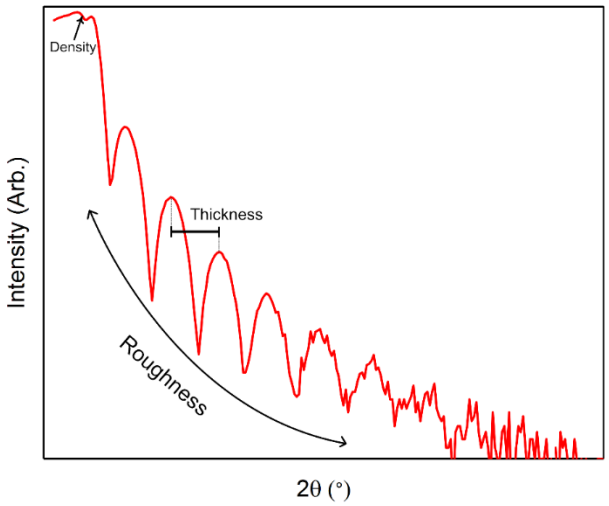

Figure 32. Information provided by XRR graph.

The critical angle is also a direct indicator for the density of the films. The density of the films can be calculated by first determining the materials mean electron density with (III).

$$\rho_e = \frac{\theta_c^2 \pi}{\lambda^2 r_e}. \qquad \text{(III)}$$

In the equation, ρ_e is the mean electron density, θ_c is the critical angle, λ is the X-ray wavelength and r_e is the classical electron radius. By assuming the ideal elemental composition where each of the organics have reacted with both of their carbonyl groups, the mass density can be calculated with (IV).

$$\rho_m = \frac{\rho_e \cdot A}{N_A \cdot Z}. \qquad \text{(IV)}$$

In the equation, ρ_m is the mass density, A is the average molar mass, N_A is the Avogadro constant and Z is the average atomic number. Densities calculated with this method are not exact, but they are comparable within a series of the same compound. [5]

8.2 Fourier Transform Infrared Spectroscopy

The Fourier transform infrared spectroscopy (FTIR) was used to gain information on the functional groups, and about their bonding and coordination. Many of the functional groups are IR active and they cause characteristics peaks in the FTIR spectrum. The peaks caused by carboxylic salts are at 1600 to 1400 cm^{-1}. The carboxylic salt peaks have a significant value since they differentiate from carboxylic acids. Therefore, it can be deduced if the precursors have reacted accordingly. An example of FTIR spectrum is shown in Figure 33.

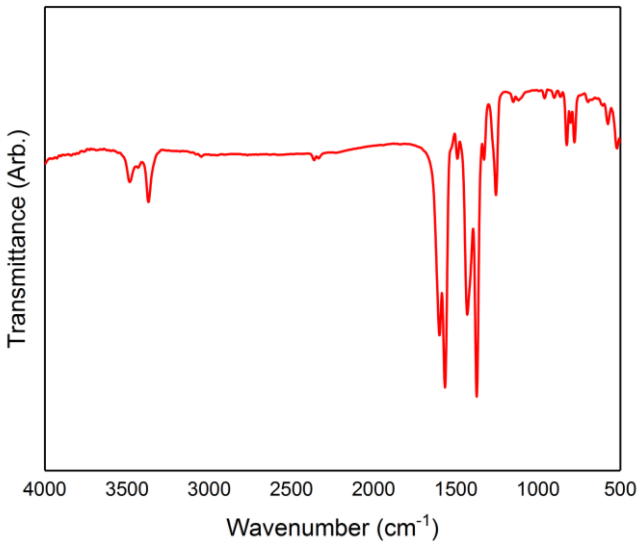

Figure 33. Example of FTIR spectrum. The peaks at 1600 to 1400 cm^{-1} are caused by antisymmetric and symmetric stretch of COO^- group.

The separation between the asymmetric and symmetric peaks is determined by the type of forming metal-oxygen complex. If the complex is bidentate the separation is 50 to 150 cm^{-1}, if the complex is bridging the separation is 130 to 200 cm^{-1}, and if the complex is unidentate the separation is greater than 200 cm^{-1} (Figure 34) [124].

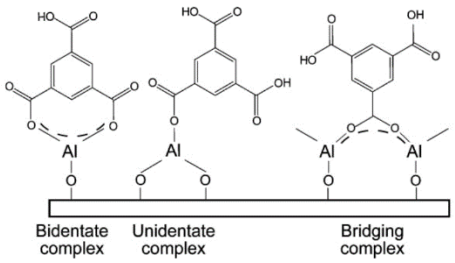

Figure 34. Differences between bidentate, unidentate and bridging complexes [124].

The FTIR apparatus was a Nicolet Protégé 460 spectrometer. The measurement range was from 400 to 4000 cm^{-1} with a resolution of 4 cm^{-1}. The films spectra were determined by subtracting the spectrum of a pure silicon substrate from the sample spectrum.

8.3 UV/Vis Spectroscopy

The optical properties were measured from the thin films deposited on borosilicate substrates. The apparatus was a LAMBDA 950 UV/Vis/NIR Spectrophotometer. Each additional functional group affects the electric band gap of the material. In theory, the modifications should also have a similar effect on the optical band gap [125]. To determine optical band gap films adsorption coefficient was calculated with Kubelka-Munk equation (V) [126].

$$\alpha = \frac{(1-R)^2}{2R}. \qquad \text{(V)}$$

In the equation, α is the absorption coefficient and R is the reflectance. The band gap is determined from the Tauc plot, where the x-axis is the photon energy and y-axis is the adsorption coefficient multiplied by the photon energy and raised to the power of 1 divided by r. The parameter r is 0.5 for direct allowed transitions, 1.5 for direct forbidden transitions, 2 for indirect allowed transitions, and 3 for indirect forbidden transitions. The band gap is determined from the point where the slope of the linear part of the function intersects with the x-axis. An example of Tauc plot is shown in Figure 35.

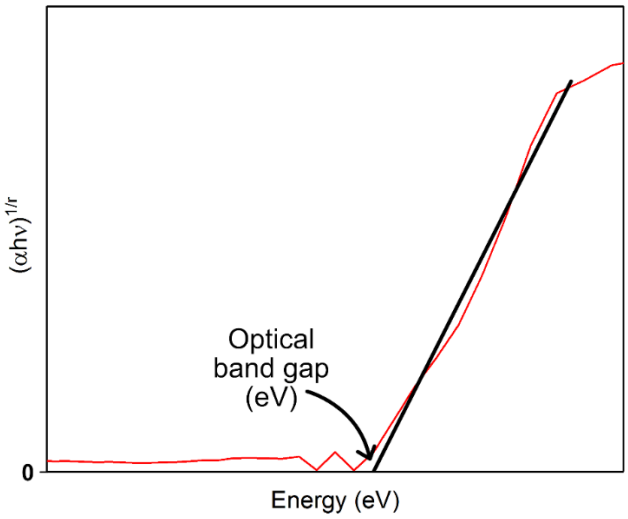

Figure 35. Example of Tauc plot and how the optical band gap is determined.

8.4 Electrochemical Measurements

To test the electrochemical performance of the assembled coin cells, cyclic voltammetry (CV) was measured from each material with an Autolab PGSTAT302N potentiostat/galvanostat. The scan rate was 0.5 mV/s and the range was from the 3.0 V to 0.01 V. The galvanostatic cycling of the cells was carried out in Neware battery testing system. Three different cycling programs were run on each material. One with 10 cycles and low C-rate, second with over 10 cycles and slightly higher C-rate and third one with different C-rates. C-rate describes the rate at which battery is charged or discharged relative to the capacity of the battery. An example of a cyclic voltammogram is shown in Figure 36.

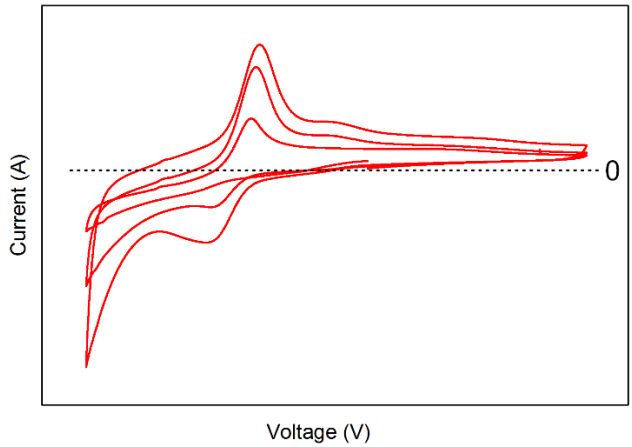

Figure 36. Example of a cyclic voltammogram.

A simplified theory of the CV states that the 1st initial peak can be explained by the Nernst equation, and the decay after peak is caused by the diffusion layer on the surface of the electrode and specifically Fick's law of diffusion through the layer [127]. If there is no current decay after the peak, the reaction is not diffusion limited. If the current is negative, reduction occurs at the working electrode (the film). The area of the peak describes how much material is reduced. Same is true for positive current and oxidation.

9 RESULTS AND DISCUSSION

In this chapter, results from the experimental work of thesis are presented and discussed.

9.1 Optimization of ALD/MLD Process

To be able to measure the films thickness with XRR, the film needs to be smooth. If the films are rough, the periodicity of oscillations is not visible and thickness cannot be determined. This proved to be case for most of the thin films grown, and especially for the crystalline films. Due to these difficulties, the Li_2TP2A process was the only one optimized.

9.1.1 Pulse Saturation

To test the saturation of pulse lengths in the Li_2TP2A films, the pulse time of the first precursor was kept constant, while the pulse/purge time of the second precursors was changed. The pulse is saturated when growth per cycle (GPC) is constant. The pulse saturation curves for LiTHD and TPA2A are shown in Figure 37.

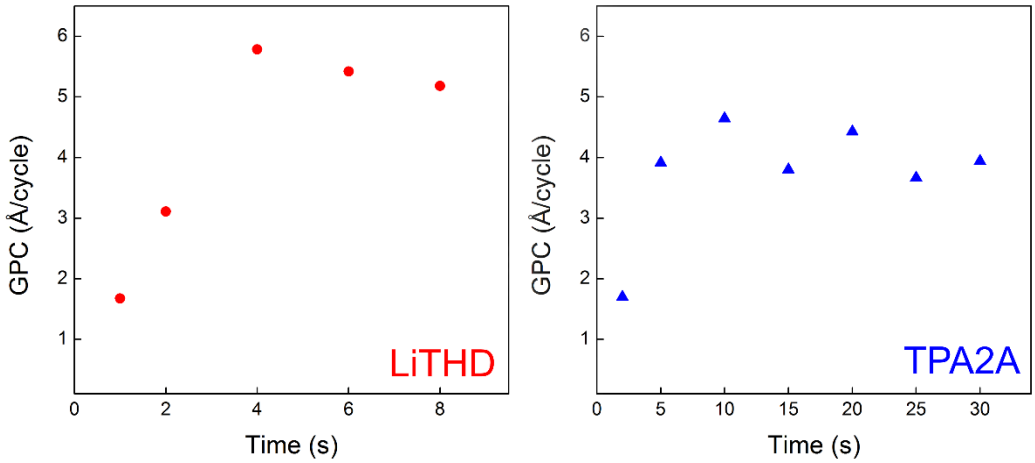

Figure 37. Saturation of the pulse lengths of Li_2TP2A. The LiTHD optimizations were made with 200 ALD/MLD cycles, while the TPA2A optimizations were made with 100 cycles. The deposition temperature was 200 °C.

As seen from Figure 37, the pulse length of both precursors saturates after 4 s for LiTHD and 5 s for TPA2A. The difference in the GPC value is probably caused by the different number of ALD/MLD cycles used in LiTHD and TPA2A optimization

experiments, 200 and 100 cycles respectively. The TPA2A depositions had to be done by only depositing 100 cycles instead of 200, since the thickness couldn't be determined otherwise. However, even if the GPC values vary in respect to ALD/MLD cycles, this process can still be ALD/MLD growth. It has been proposed that many crystalline thin films grow *via* an island growth nucleation model, which explains the nonlinear growth [5]. This is further supported by the fact that the films deposited with 200 ALD/MLD cycles were crystalline, while the films with 100 cycles were amorphous, as seen later.

9.1.2 Density

The critical angle is a direct indicator for the density of the film. In the case of Li_2TP2A, the films deposited with over 200 cycles and the films deposited with 100 cycles exhibited different critical angles, indicating that the materials density is different. For example, the density of a crystalline Li_2TP2A film can be calculated with equations III and IV, when the film is assumed to be only composed of the desired material.

$$A(Li_2C_8H_5O_4N) = \frac{(6.94\cdot 2 + 12.011\cdot 8 + 1.008\cdot 5 + 15.999\cdot 4 + 14.007)\,\frac{g}{mol}}{20}$$

$$A = 9.65\,\frac{g}{mol}$$

$$Z = \frac{3\cdot 2 + 6\cdot 8 + 1\cdot 5 + 8\cdot 4 + 7}{20} = 4.9$$

$$\rho_e = \frac{\theta_c^2 \pi}{\lambda^2 r_e} = \frac{0.003063^2 \cdot \pi}{(1.54\cdot 10^{-10}\,\mathrm{m})^2 \cdot 2.82\cdot 10^{-15}\,\mathrm{m}} = 4.41\cdot 10^{29}\,\mathrm{m}^3$$

$$\rho_m = \frac{\rho_e \cdot A}{N_A \cdot Z} = \frac{4.41\cdot 10^{29}\,\mathrm{m}\cdot 9.65\,\frac{g}{mol}}{6.022\cdot 10^{23}\,\mathrm{mol}^{-1}\cdot 4.9} = 1.44\,\frac{g}{cm^3}$$

The density of the 400-cycle Li_2TP2A film was ca. 1.4 g/cm^3 while the density of the 100-cycle film was ca. 1.6 g/cm^3. To our best knowledge, no experimental information about the density of crystalline bulk Li_2TP2A exists and therefore comparison is not

possible. However, the simulated density of Li_2TP2A was calculated to be 1.634 g/cm^3, which is slightly higher than the measured one from the film with 100 ALD/MLD cycles and 0.2 g/cm^3 higher than the density measured from the film with 400 ALD/MLD cycles. The density was higher in the depositions where the pulse lengths were too short to achieve saturated growth, thus producing thinner films. The lower density of the films with the higher number of ALD/MLD cycles is shown in Figure 38.

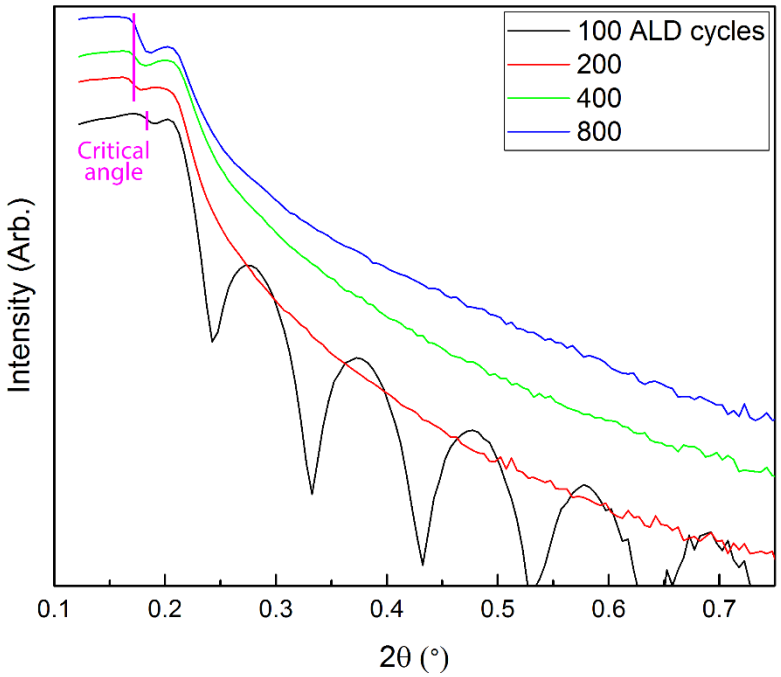

Figure 38. XRR graphs for Li_2TP2A thin films deposited with 100 vs. 200, 400, and 800 ALD/MLD cycles. The depositions with 200 or more cycles share a similar critical angle, while deposition with only 100 cycles is notably different. The two critical angles are caused by the deposited material and the substrate. The critical angle of silicon is at around 0.22°.

9.1.3 Film Growth

Even if the thickness of the crystalline films could not be measured by the instruments available, the gradual color change of the films can be a powerful qualitative indicator for the thickness. The color change of the films vs. the number of cycles can be seen in Figure 39.

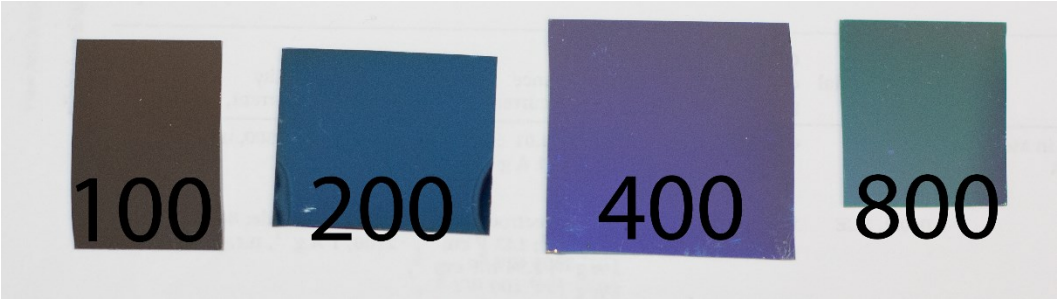

Figure 39. Gradual color change of the films vs. the number of cycles.

A series of depositions were made at different temperatures to examine the temperature dependence of the growth and the "ALD temperature window". The problems with the films roughness were again present, but a qualitative analysis can be made from the color of the films (Figure 40).

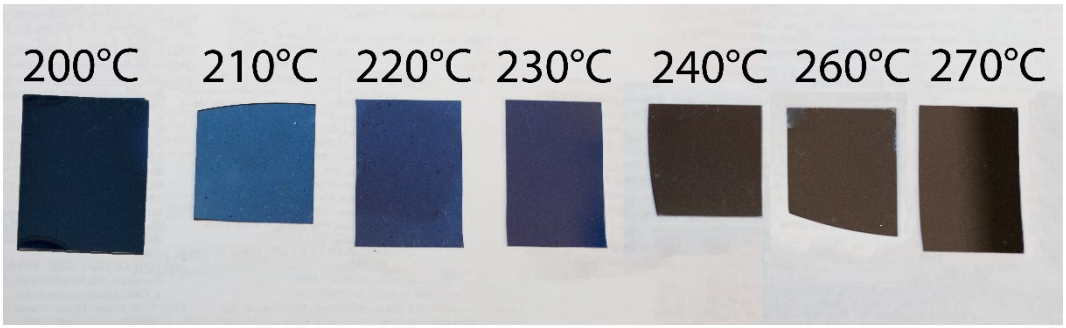

Figure 40. Color analysis of the films, where the color disappears between 230 and 240 °C.

The depositions were made with 200 ALD/MLD cycles and within temperature range of 195 to 270 °C. From the analysis, it can be clearly seen that the blue color vanishes between 230 and 240 °C, indicating that the growth has slowed down. The same observation is visible when the critical angle of the films is analyzed (Figure 41).

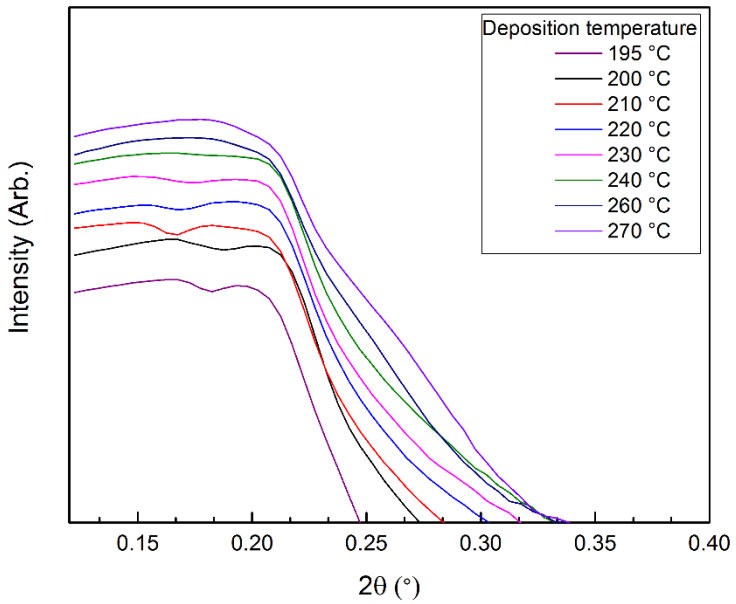

Figure 41. Change in the critical angle when the deposition temperature rises.

In Figure 41, two notable things occur. From 240 to 270 °C the typical critical angle of the films disappear. Also, the density of the films decrease when temperature rises from 200 to 210 °C. The disappearance of the critical angle occurs at the same point where the films lost their color. At higher temperatures only one critical angle is visible indicating that the growth is minimal. The density decrease of the film at 210 °C could be caused by increased crystallinity.

9.2 Crystallinity

The crystallinity of the Li_2TP2A films is discussed in its own chapter since it was studied in various occasions. The crystallinity of the other materials is shown in a separate chapter.

9.2.1 Li_2TP2A

The thin films deposited were mostly crystalline. The films with 100 ALD/MLD cycles were amorphous. Without an exception, all films with more than 400 ALD/MLD cycles were crystalline. The crystal structure of Li_2TP2A, was determined by computational method USPEX by Professor Karttunen (Figure 42).

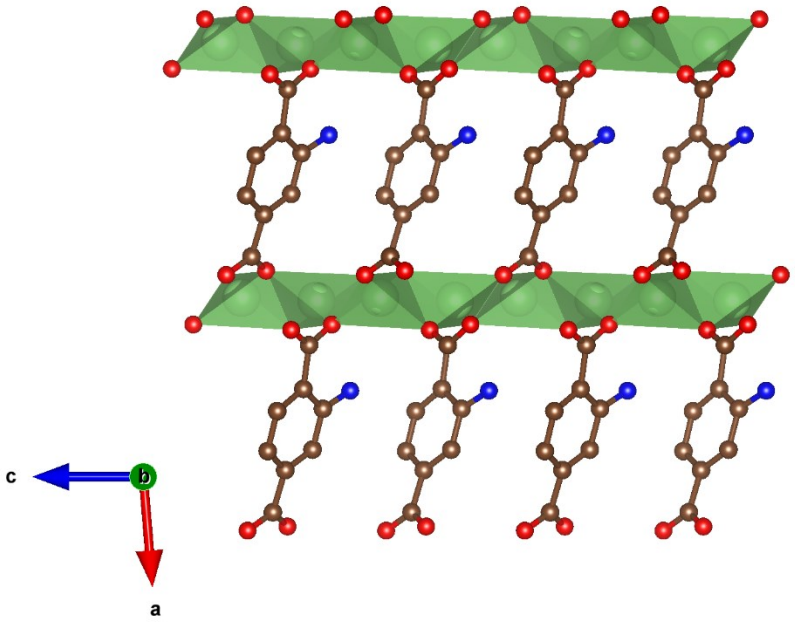

Figure 42. Minimum energy crystal structure of Li_2TP2A computed with USPEX.

The crystal structure in Figure 42, is the minimum energy structure, but not by large margin. In the alternative crystal structure, the direction of amino group can be on opposite side. The XRD pattern of the calculated structure was simulated using FullProf Suite [128] and it was compared to the measured GIXRD pattern of Li_2TP2A (Figure 43).

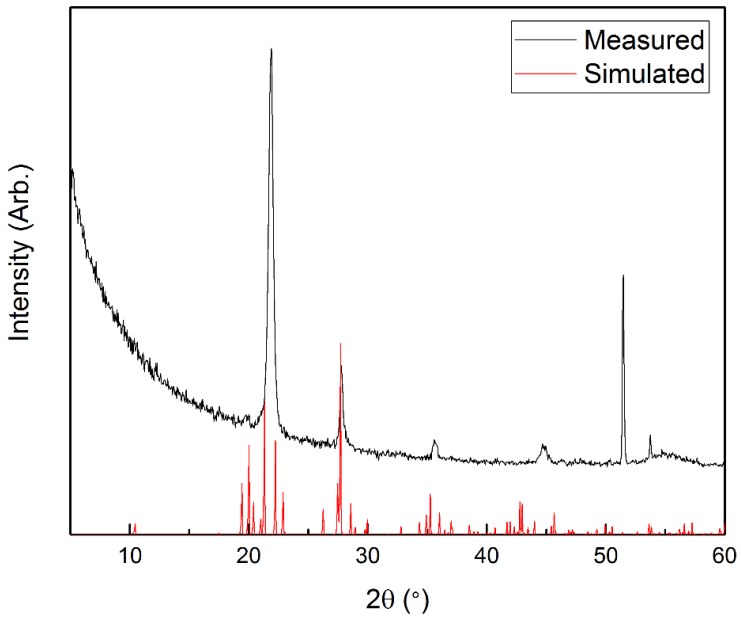

Figure 43. Measured GIXRD diffraction pattern with 800 ALD/MLD cycles and the simulated XRD diffraction pattern of Li_2TP2A. The peak at 52° is from silicon substrate.

The simulated and the measured XRD patterns share characteristics, but they are definitely not a perfect match. Comparing the films diffraction pattern with the powder or simulated one, is often a difficult task since films may have residual stress due to the synthesis or they may exhibit preferred orientation, which all have an effect on GIXRD pattern.

Earlier it was noted that density decreases as a function of temperature. Therefore, it is possible that some additional peaks could appear in the GIXRD graph (Figure 44).

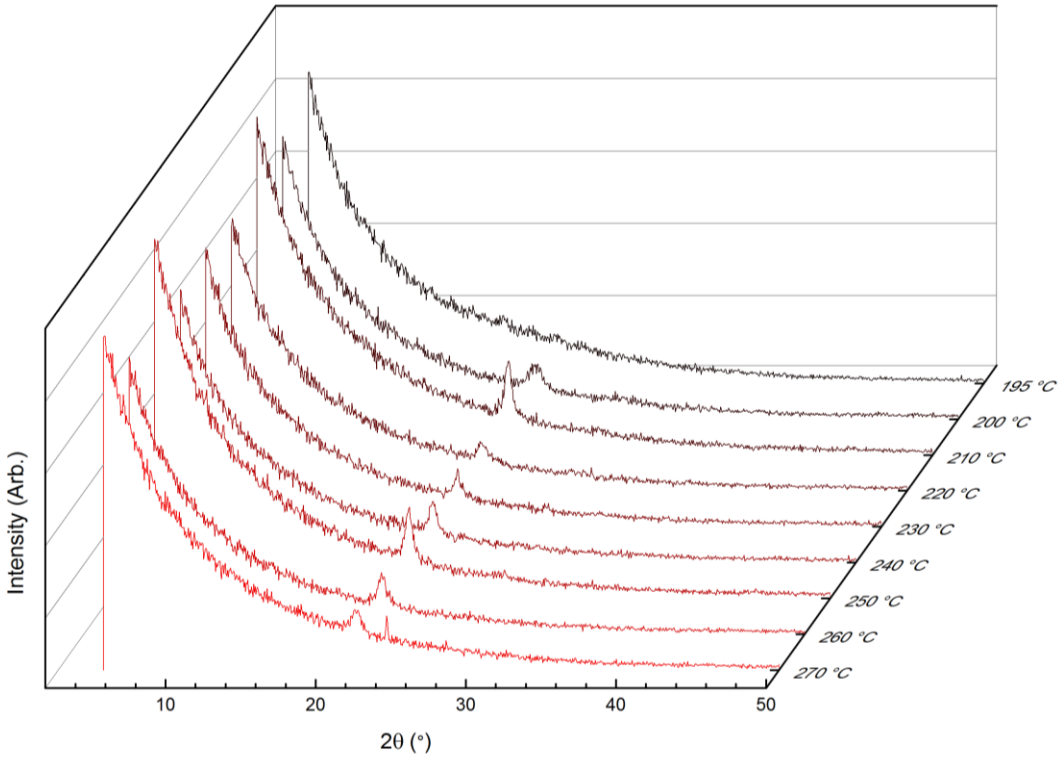

Figure 44. GIXRD patterns of Li_2TP2A deposited with 200 ALD/MLD cycles at various temperatures.

The typical peak at 22° emerges when temperature increases from 195 to 200 °C, implying that films start to have more crystalline characteristics at 200 °C and onwards. One additional peak emerges around 25° at 270 °C, which has no explanation. The results might have been way more informative if the number of ALD/MLD cycles would have been increased to 400. From the thicker films, it is considerably easier to obtain higher quality XRD data and therefore more peaks might appear in the graph (Figure 45).

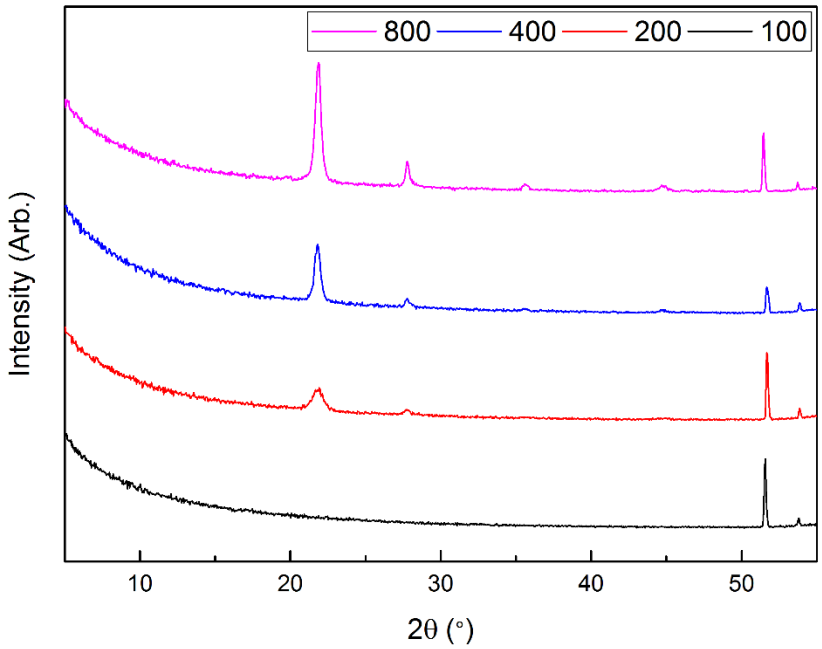

Figure 45. Peak intensity as a function of ALD/MLD cycles, which clearly shows how the intensity increases and new peaks appear as the films get thicker.

9.2.1 Other Films

Since the processes of Li_2TP25OH, Li_2TPBr, Li_2PDC25, or Li_2PDC35 were not optimized any reasonable claims about their temperature dependence or growth linearity cannot be made. The GIXRD patterns of the materials are shown in Figure 46.

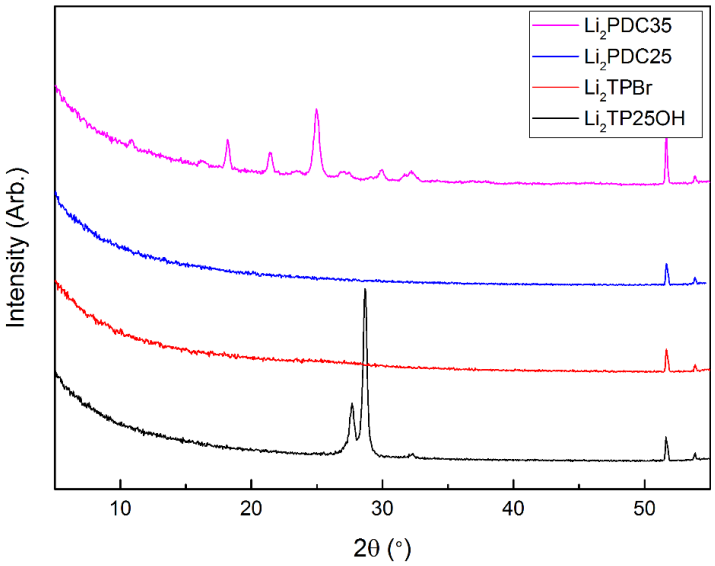

Figure 46. GIXRD patterns of Li_2TP25OH, Li_2PDC35, Li_2TPBr, and Li_2PDC25. Li_2TP25OH and Li_2PDC35 were clearly crystalline, while Li_2TPBr, and Li_2PDC25 were completely amorphous.

The GIXRD pattern of Li_2TP25OH shows one large and very intensive peak pair. Deng *et al.* [129] have synthetized Li_2TP25OH in bulk form and their XRD data shows similar peak (Figure 47).

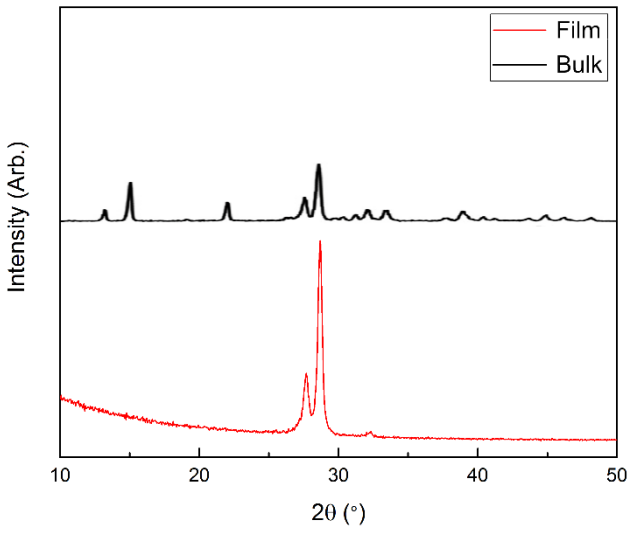

Figure 47. Comparison of bulk [129] and thin film Li_2TP25OH XRD spectra.

The peaks at 27 – 30° are remarkably similar in bulk and in the thin film sample, implying that the film might have similar structure to the one reported by Deng *et al.* [129]. The FTIR spectrum of the samples was also remarkably similar, which is discussed in the next chapter.

9.3 Composition

The composition, durability and the type of bonding of the thin films was studied with FTIR. Spectra of the deposited films are shown in Figure 48.

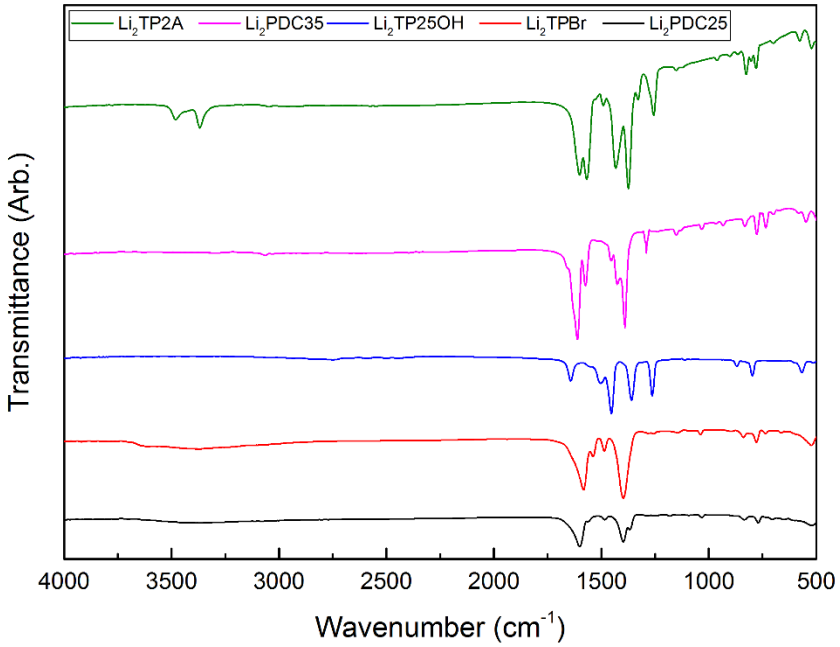

Figure 48. FTIR spectra of the films. All measurements were done shortly after the deposition.

The carboxyl group is clearly visible in the FTIR spectra and it causes characteristic peaks around 1500 cm^{-1}. If there would be a carboxylic O—H bond in the films, it would be visible in the 3400 – 2400 range, and none of the films have such peak. In the case of Li_2TP2A the peaks at 3450 – 3250, belong to a primary amine, which was confirmed by measuring the FTIR spectra of the pure precursor TPA2A (Figure 49). In Li_2TPBr, the peak at 650 - 500 is caused by stretching of C—Br bond. The peaks around 800 are caused by the aromatic C—H bonds of the benzene and pyridine rings, but they are shifted slightly depending on the number of substituents and the nature of the aromatic ring. Appointing the peaks to the Li_2TP25OH is rather difficult, since no unambiguous conclusions could be made. Fortunately FTIR spectrum of Li_2TP25OH prepared by Deng *et al.* [129] match with the film's (Figure 49).

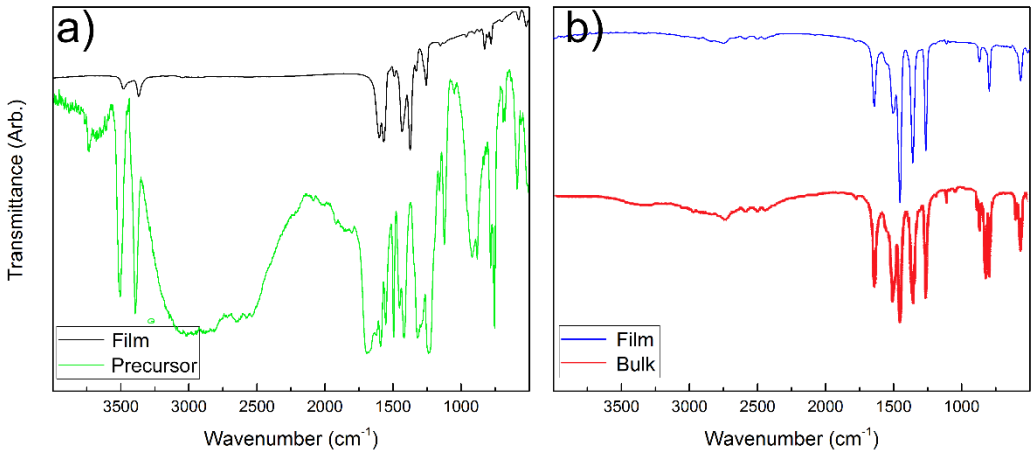

Figure 49. In the a), the comparison between bulk precursor TPA2A and a thin film of Li_2TP2A. The peaks caused by amino group (3450 – 3250 cm^{-1}) are visible in both samples. This indicates that amino group has remained unchanged during the deposition. In the b), the comparison of FTIR spectra between the bulk $Li_2TP25OH$ prepared by Deng *et al*. [129] and the thin film deposited in this study.

With the FTIR (Figure 49b) and XRD (Figure 47) spectra matching well, it can be concluded with high confidence that the material deposited is actually $Li_2TP25OH$ or at least the same material which Deng *et al.* prepared. The real interesting area of these spectra are from 1600 to 1400 cm^{-1}, where the symmetric and asymmetric stretches of the COO^- group take place. The separation of asymmetric and symmetric peak of different thin films are compared in the Table 5.

Table 5. The separation of asymmetric and symmetric peak of the deposited thin films.

Material	Separation (cm^{-1})	Type
Li_2TP2A	183	Bridging
Li_2TPBr	185	Bridging
Li_2PDC35	193	Bridging
Li_2PDC25	200	Bridging

The separation of the peaks for the $Li_2TP25OH$, could not be reliable identified since multiple peaks appear in the spectrum. The peaks are caused by the multiple C—O bond present in the molecule. But since the FTIR and XRD spectra match well with the reported bulk structure, it can be concluded with high confidence, the carboxyl group has reacted well with lithium in all of the films.

Earlier, the temperature dependence of the Li_2TP2A growth was discussed and same conclusions can be made from FTIR spectra. The magnitude of the absorbance diminishes as the temperature rises, which is also a qualitative indicator for films getting thinner. The GIXRD of Li_2TP2A showed one additional peak appearing at 270 °C, which remains unexplained even after close inspection of the FTIR spectrum, since no additional peaks appear. The additional peaks could indicate that the film or the precursors are decomposing (Figure 50).

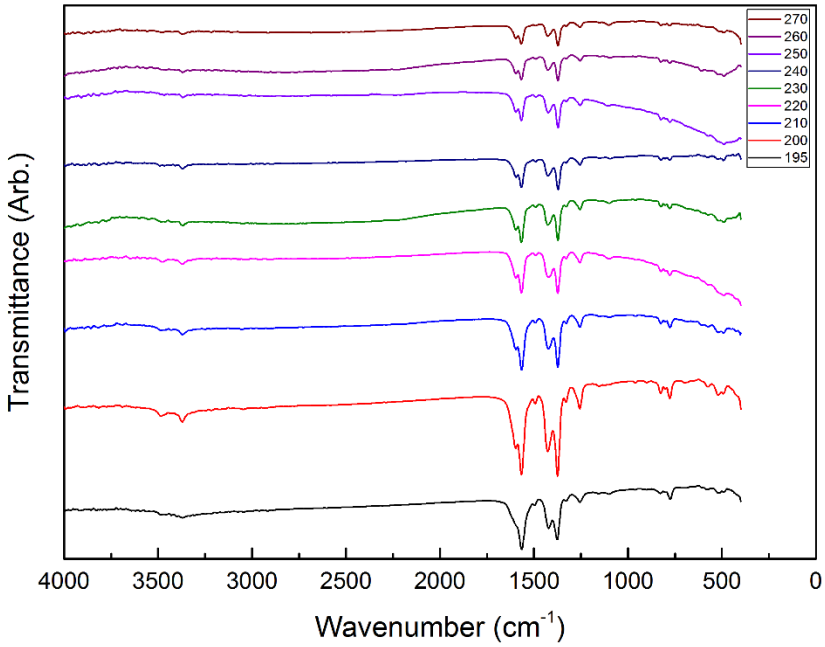

Figure 50. Change in the FTIR spectra with increasing temperature.

Earlier, it was seen that at 195 °C the films were not crystalline. The amorphous to crystalline change can be seen also in the FTIR spectra when temperature is increased from 195 °C to 200 °C, causing the peak at 1600 cm^{-1} to become better defined. The same transformation also occurred when the ALD/MLD cycles were increased from 100 to 200. The difference is caused by the surrounding environment being more defined in crystalline materials, therefore causing sharper peaks.

The durability of the thin films was checked by measuring the FTIR spectra after 3 months of storage in ambient conditions (Figure 51).

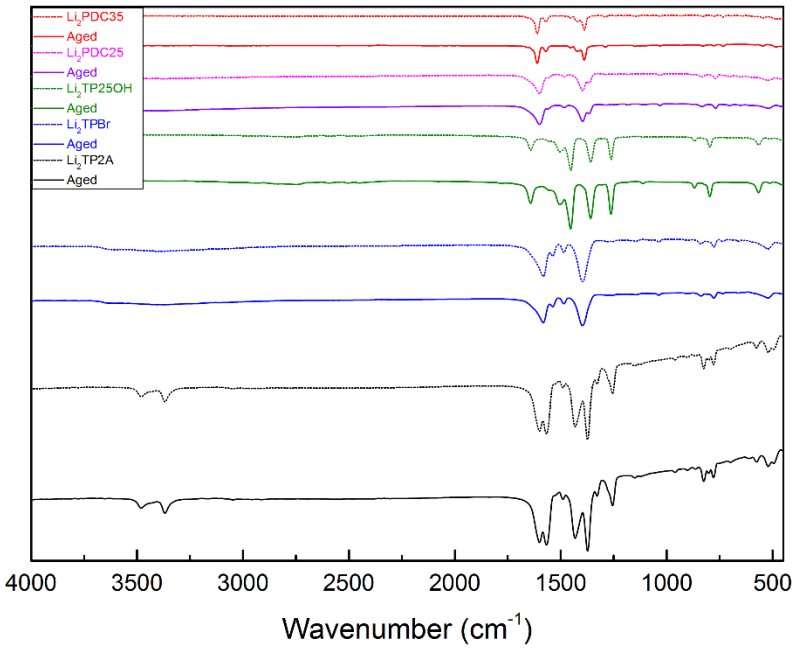

Figure 51. FTIR spectra of the films immediately after deposition and after 3 months of storage in ambient conditions.

The peaks have remained nearly identical and no water absorption has occurred, which would be clearly visible at 3000 – 3500 cm^{-1}. Therefore, the films are stable even in ambient conditions.

9.4 Optical Properties

UV-VIS spectroscopy was used to determine the reflectance from which the optical band gap can be calculated. The different functional groups in the films should cause effects on the electric band gap. In addition, the functional groups should also cause similar shift in the optical band gap [125]. Absorption coefficients of the films were calculated with the Kubelka-Munk equation (V). The Tauc plots of the Li_2TPBr, Li_2TP2A, and Li_2TP are shown in Figure 52.

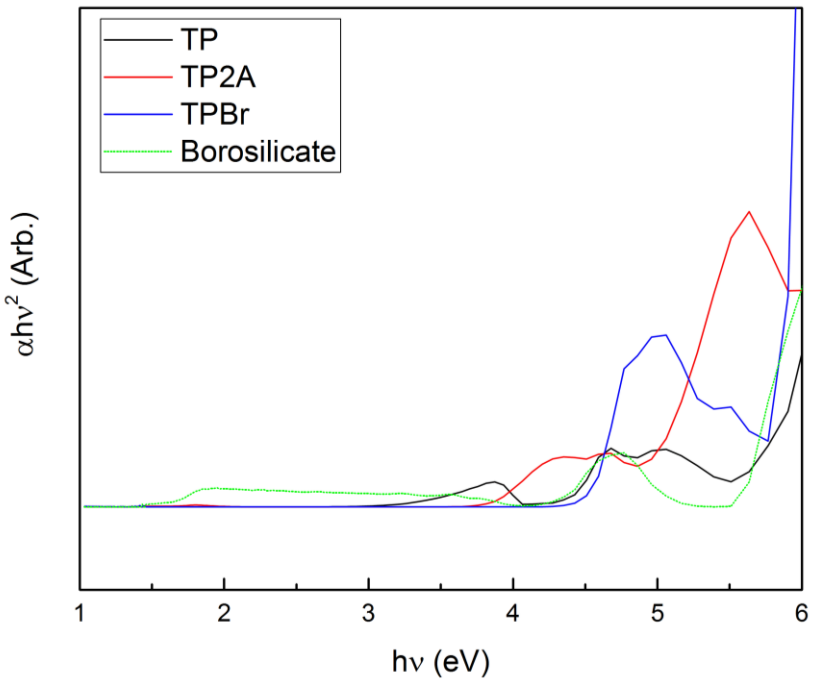

Figure 52. Tauc plot for selected thin films. The exponent is chosen for direct allowed transitions, which is a sophisticated guess based on the nature of material.

The optical band gaps can be determined from the Figure 52. The band gaps are 4.5, 4.9, and 4.3 eV for Li_2TPBr, Li_2TP2A, and Li_2TP, respectively. In theory, the LUMO energy of Li_2TPBr should be the most negative, while the LUMO energy of Li_2TP2A should be the most positive. If HOMO energy would stay as a constant the band gap of Li_2TPBr should be smallest and the band gap of Li_2TP2A highest, which is almost the case here. However, the band gap of Li_2TP is smaller than the band gap of Li_2TPBr, which is probably caused by the electron donating or withdrawing groups. The groups can have an even bigger effect on the HOMO than the LUMO and because of this it is hard to find any proof if the LUMO energy was actually modified as intended just by inspecting the optical band gap [125]. The data from UV-VIS measurements is also rather low quality, since the reflectance measurement of transparent thin films is difficult to do and absorbance measurement was not available at the time.

9.5 Electrochemical Performance

The electrochemical performance of the films was evaluated with CV, galvanostatic cycling and with different C-rates. The results are discussed in the next chapters.

9.5.1 Redox activity

The cyclic voltammetry was conducted on the coin cells whose assembly was described earlier. The films inside of the coin cells were deposited with 400 ALD/MLD cycles. In the measurements, it was decided to only use capacity or current per area, since as discussed earlier, the thickness of the films is unknown and therefore also the mass of the electrode is unknown. This of course raises a question if increasing the number of ALD/MLD cycles would also increase the capacity per area. However with these limitations, the redox potential is still comparable within a series, capacity is not. The voltage range was from 3.0 V to 0.01 V versus Li^+/Li, starting from the open circuit voltage. The voltammograms of the coin cells are shown in Figure 53.

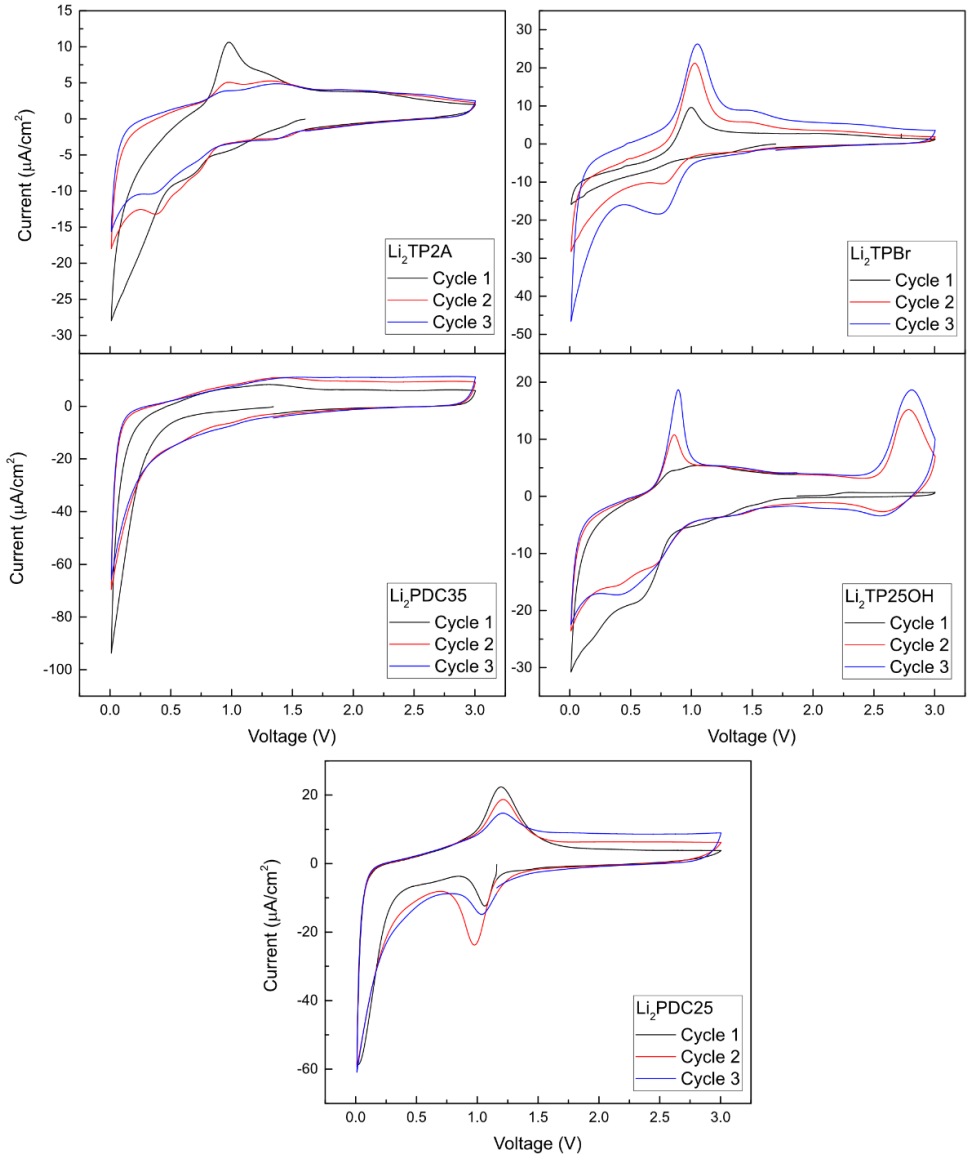

Figure 53. Cyclic voltammograms of Li_2TP2A, Li_2TPBr, $Li_2TP25OH$, Li_2PDC35, and Li_2PDC25.

The cyclic voltammograms show that the coin cells are electrochemically active. All of the cyclic voltammograms have a sharp peak at 0.01 V, which is probably caused by the decomposition of the electrolyte. Starting from Li_2TP2A, during the 1st cycle the CV shows two small reduction peaks at 0.96 V and 0.7 V, and one broad oxidation peak at 0.98 V. During the 2nd and 3rd cycle one additional peak appears at 0.34 V, which is not visible during the 1st cycle, which might be due the peak at 0.01 V being very broad. The peak caused by oxidation also gets notably smaller after the 1st cycle, however the overall oxidation area is still 91 % of the 1st cycle. During the 1st cycle of Li_2TPBr, there are no visible reduction peaks and only after the oxidation a clear reduction peaks appear at 0.75 V. Oddly enough, the current density of both oxidation and reduction increases, which might imply that the electrode goes through of some kind of morphological transformation, since more capacity becomes available. The relation of oxidation and reduction peaks during 2nd and 3rd cycles also show that the reaction is somewhat reversible, since the equivalent reduction and oxidation areas are within 99 % of each other. The voltammogram of Li_2TP25OH shows interesting properties. The 1st cycle shows broad reduction peak at 0.5 V and also a very similar broad peak at 2nd and 3rd cycles. Second reduction reaction occur at 2.58 V during the 2nd and 3rd cycles, while the oxidation side also show two separate peaks at 0.86 V and 2.79 V. These peaks can be explained by the redox reaction of carboxyl groups at lower potential and the redox reaction of alcohol groups at higher potential. The multiple redox reactions occurring far away from each other could in theory allow the usage of Li_2TP25OH as both anode and cathode, if for example the cathode side could be deposited in the form where both alcohol groups are lithiated. This could be achieved by using more reactive lithium precursor such as LiHMDS during the deposition. The 1st cycle in almost all of the materials seems not to be diffusion limited, while the second and third are. However, with even slower scan rates it could be possible to see the formation of diffusion layers.

Moving on to the pyridine derivatives, the Li_2PDC35 shows no clear peaks, excluding the peak at 0.01 V. However, since the current density is negative, some reduction reaction must take place, which probably is not related to carboxyl. The carboxyl groups in the PDC35 are separated only by one carbon atom inside the benzene ring, which makes the reduction reaction at the carboxyl group impossible to occur (Figure 54).

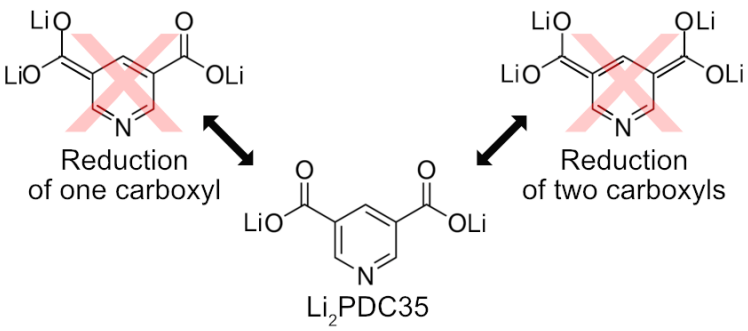

Figure 54. Problematic reduction pathways of Li_2PDC35.

The Li_2PDC25 displays only one relatively sharp reduction (~ 1.0 V) and oxidation peak (~ 1.2 V). Both reduction and oxidation occur in higher potential, compared to the aromatic rings without the nitrogen. Therefore, the nitrogen inside a ring acts as an electron withdrawing group. Due to the similar peak areas, the reaction can be considered pseudo reversible. However, during the 1st cycle oxidation peak area is larger, while at the 2nd cycle it is smaller compared to the reduction peak and only during the 3rd cycle the peaks are approximately the same area. This could indicate that some morphological changes occur during each cycle allowing more material to become redox active.

9.5.2 Cyclability

Similar coin cells were also used to determine the cycling capabilities of these materials. The preliminary tests were made with really low current density to achieve the maximum capacity. The charge discharge curves of the coin cells are shown in Figure 55.

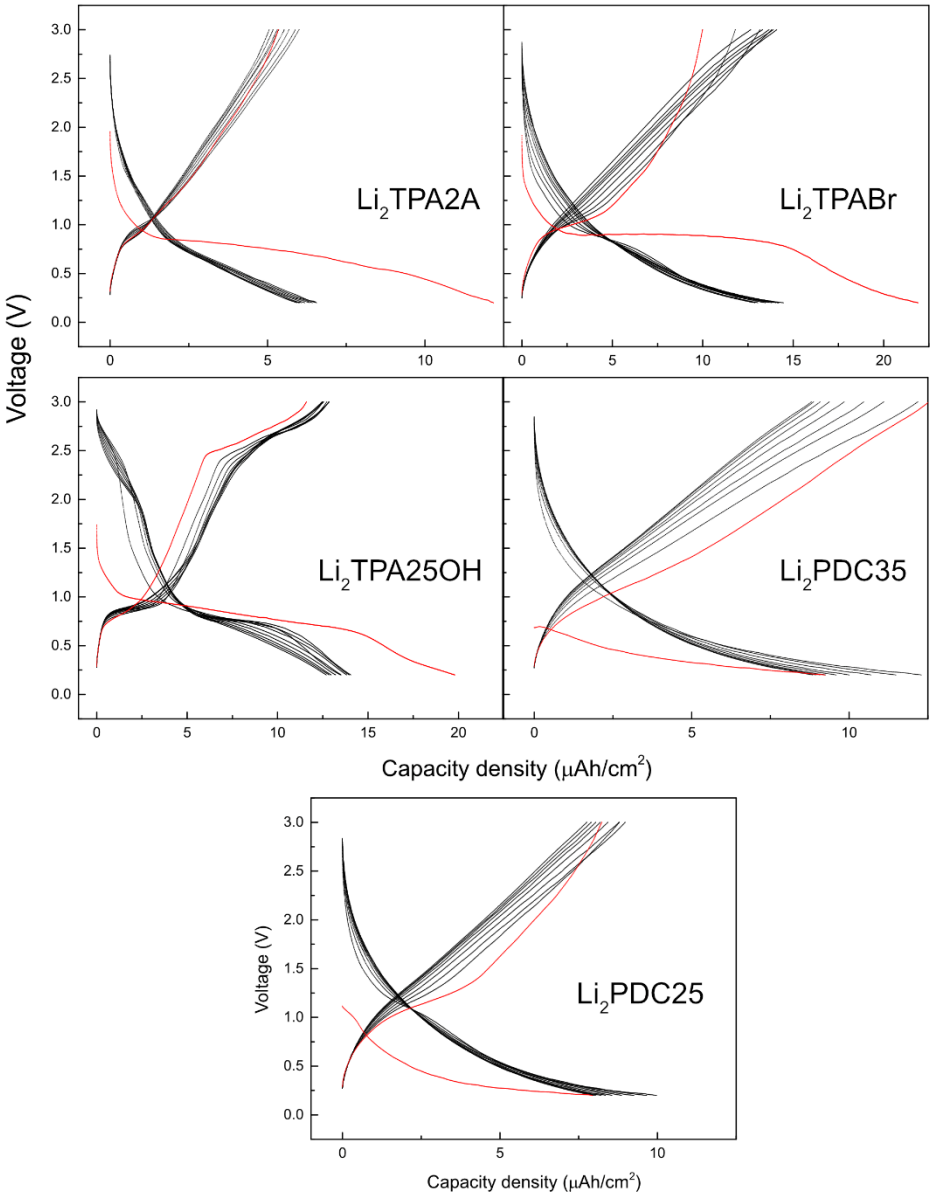

Figure 55. Charge discharge curves of the coin cells, where the 1st cycle is colored red. The current density was approximately 1 μA / cm^2.

The charge discharge curves show that in all materials the 1st cycle is drastically different from other cycles. In terephthalate derivatives, the reduction potential of the 1st cycle is considerably flatter than the following cycles. This makes it easier to compare reduction voltages with the Li_2TP, since it also possesses a flat reduction potential (Table 6).

Table 6. Comparison of the average lithiation potential of the flat section within terephthalate derivatives.

Compound	Li_2TP	Li_2TP2A	Li_2TPBr	$Li_2TP25OH$
Reduction potential (V)	0.81 [5]	0.75	0.86	0.79

As shown in Table 6 the average lithiation potential increases with electron withdrawing groups (Br), and decreases with electron donating groups (-NH_2 and -OH), as predicted. However, after the 1st cycle kinetics change drastically and the capacity decay is notable. The loss of flat reduction potential indicates that the reaction mechanism transforms from two phase reaction to one phase reaction or to multiple complex ones, which all produce a slope.

The pyridine derivatives act completely differently during the measurement. During the 1st cycle the capacity and the reduction voltage is notably lower compared to the rest of cycles. After the 1st oxidation cycle, the "normal" behavior starts to occur. This might be due to morphological changes on the surface of the electrode, which was already suspected when analyzing the cyclic voltammograms earlier.

When the capacities of the materials are compared, Li_2TPBr and Li2TP25OH have the highest initial capacities. The specific capacities of the coin cells as a function of cycles is drawn in Figure 56.

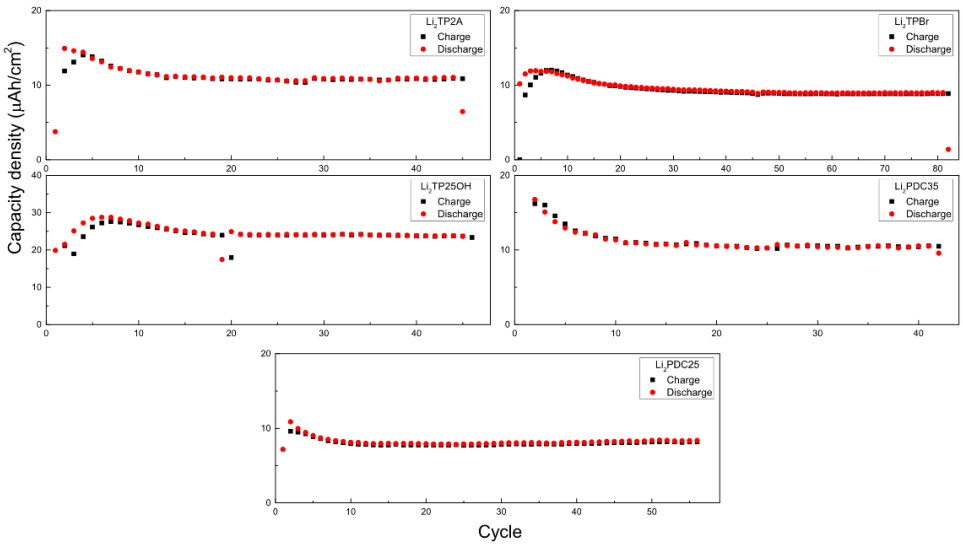

Figure 56. Capacity density as a function of cycles.

All of the cells show rather stable cycling ability after the initial cycles. The materials Li_2TP2A, Li_2TPBr, $Li_2TP25OH$, Li_2PDC25, and Li_2PDC35 retain 95, 92, 87, 98, and 92 % of their discharge capacity respectively, from cycle 10 to the end of cycling.

9.5.3 Rate Capability

Charge discharge rate capability (C-rate) is another important electrochemical parameter. The battery needs to be able to deliver decent capacity, even if it is discharged rapidly, and even better if it can be charged to the maximum capacity quickly. The exact C-rates of the samples are not known, but comparing the capacities at different current densities can be used as an exact alternative (Figure 57).

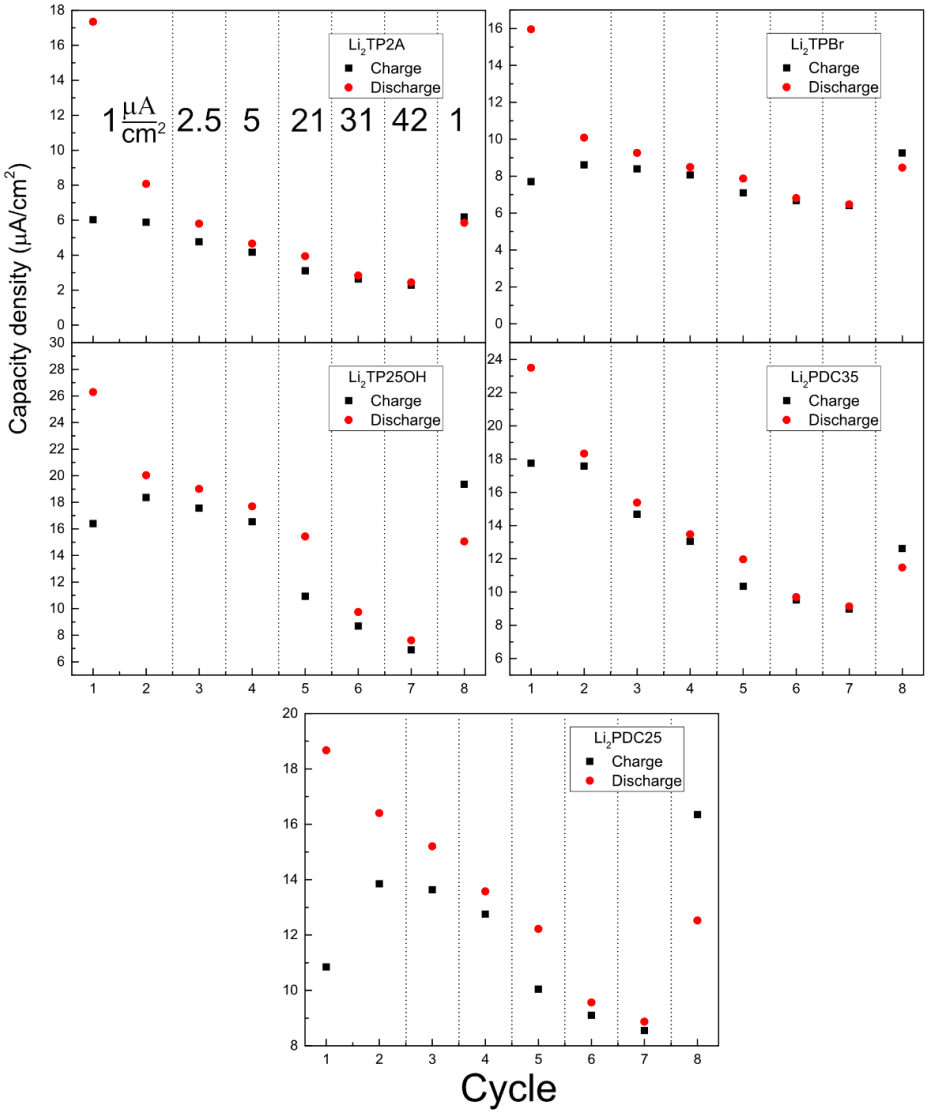

Figure 57. Capacity of the films measured at different current densities. The cycles 1, 2, and 8 are measured with the current density of 1 μA/cm^2 and the cycles 3, 4, 5, 6, and 7 with the current densities of 2.5, 5, 21, 31, and 42 μA/cm^2, respectively.

The cycles one and two were decided to be charged with a current of 1 μA/cm^2 to lessen the effect caused by the 1st cycle and therefore be able to calculate the capacity retained between cycles 2 and 8. The capacity retained for the Li_2TP2A, Li_2TPBr, Li_2TP25OH, Li_2PDC25, and Li_2PDC35 were 72, 83, 75, 76, and 62 % respectively. Performance of the coin cells on the higher current densities varies. When comparing the cycles 2 and 7, e.g. the initial reduction capacity versus the capacity at the highest current density, Li_2TPBr outperforms the other materials, by retaining 64 % of its capacity. The Li_2PDC25 is the second which delivers 54 % of its initial capacity, followed by Li_2PDC35 at 49 %, Li_2TP25OH at 38 %, and Li_2TP2A at 30 %.

Overall, Li_2TPBr performed well in both cycling and current density experiments, making it an interesting option to look into more carefully in the future. The bromine group is not optimal for anode materials, since it increases the reduction voltage, but since it seems to deliver the most stable kinetics, it may be worthwhile to look into adding a bromine group into some potential cathode materials, and to see how their electrochemical properties are affected. The weakest performer electrochemistry wise was Li_2TP2A on all fronts, which is unfortunate, since the ALD process of it is working well.

The functional groups affected the voltage as expected, but they also negatively affected the reaction kinetics. Since the change in voltage is marginal, and no significant improvements were observed during cycling it can be a concern if the functionalization is a valid approach to improve the electrochemical properties of organic electrode materials. However, film quality and uniformity of growth on the steel substrate was not taken into account, and it may have major impact on the electrochemical performance of the films. Example of this can be seen during the longer cycling of Li_2TP25OH, which yields notably higher capacities on the latter, even if the substrates were deposited in the same batch.

10 CONCLUSIONS

Organic electrode materials are an interesting alternative to the inorganic electrode materials, since they possess a high gravimetric energy and power density. Films made with organic materials are often flexible and transparent. Organic electrode materials do not require expensive and rare metals, they are abundant and can be produced from sustainable resources. The redox properties of organic electrode materials can be tuned, due to the immense structural diversity of organic materials. Modifying the carbon skeleton or adding a functional group can have a significant effect on the properties of organic electrode materials.

The goal of this thesis was to develop new ALD/MLD processes for organic lithium salts. These salts are analogous to another organic anode material Li_2TP, but they have an additional electron withdrawing and donating group. The goal of these modifications was to see which of the functional groups is the most effective at tuning the redox properties. The chosen organic molecules were 2-aminoterephtalic acid (TPA2A), 2-bromoterephtalic acid (TPABr), 2,5-dihydroxylterephtalic (TP25OH) acid or 2,5-pyridinecaboxylic acid (PDC25), and 3,5-pyridinecaboxylic acid (PDC35). These molecules, with the lithium source LiTHD (THD = 2,2,6,6-tetramethyl-3,5-heptanedione), were employed as the ALD/MLD precursors.

Even the smallest modifications alter the ALD process and therefore each one of the materials would require extensive study and optimizations to confirm the linear ALD growth. During preliminary tests, the films with the TPA2A showed to be the most promising and therefore it was chosen to be optimized and experimented in more detail. Parameters for the rest of the materials were chosen based on the film uniformity and if the films were crystalline.

Pulse saturation was confirmed for the Li_2TP2A films during the first 100 ALD/MLD cycles. The thickness of the films could not be reliably determined with XRR after 200 cycles, since the films became crystalline and rough. The density of the Li_2TP2A films also decreased when the amorphous to crystalline transformation occurred. These results could imply that the nucleation mechanism of Li_2TP2A is the island growth type, but further experiments were not made. The linearity of the growth was experiment by observing the gradual color change of the films. The temperature

dependence of the growth was experimented with similar method, since the thickness could not be determined from the films. The growth is clearly slowed down after the deposition temperature rises over 230 °C. The critical angle caused by the film, also starts to disappear in this particular temperature range. The films were crystalline between 200 to 270 °C, and amorphous at 195 °C. The minimum energy crystal structure of Li_2TP2A was predicted with structure evolutionary computational method USPEX. The simulated and measured XRD share characteristics, but the match is far from perfect. Even with all the inconvenience, the development of new ALD/MLD process for organic lithium salt Li_2TP2A was successful.

Out of the rest of the materials, Li_2TP25OH and Li_2PDC35 were also crystalline, while Li_2TPBr and Li_2PDC25 were amorphous. The XRD of Li_2TP25OH is very similar with the bulk material prepared and reported by Deng *et al.* [129], also the FTIR data is almost a perfect match. Therefore, it is probable that the film and the bulk share similarities in the actual crystal structure.

The FTIR showed that the bond between carboxyl and the lithium is bridging type in most of the materials. The bonding type of Li_2TP25OH could not be determined since the free alcohol groups make the interpreting of the spectrum difficult. The films FTIR spectra were measured again after 3 months of storage in ambient conditions, and no changes are visible, which implies that the films are rather stable in ambient conditions. The results from the UV-VIS measurements are indecisive, but it shows that functionalization has a strong effect on the optical band gap.

The cyclic voltammograms show that all the materials are electrochemically active and that the 1st cycle differs drastically from the rest. The redox reactions of Li_2TPBr and Li_2PDC25 are somewhat reversible. Many of the materials show interesting property where more material becomes electroactive after the initial cycle. This might be due some morphological change on the surface of the electrode. The reduction voltages were successfully affected by the functionalization. The electron withdrawing group increased the voltage, while the electron withdrawing groups decreased it, confirming the hypothesis. However, the kinetics were strongly altered after the 1st cycle and no notable improvements in rate capability or cycling are observed. Out of these materials, the Li_2TPBr seems to be most promising with a notable effect on the reduction potential, decent rate capability, good cycling properties and high capacity.

Therefore, addition of Br yielded the most convincing results, even if raising the reduction potential in the anode materials is not the intent. After all, there is no reason to believe that Br would not increase the reduction potential also for cathode materials.

The organic electrode materials are still a rather new topic and still a lot of preliminary research needs be done. Hopefully someday the organic electrode materials will be comparable to inorganic ones.

11 SUGGESTIONS FOR FURTHER RESEARCH

To be able to determine the thickness of the rough crystalline thin films should be the first step in the further research. Without the thickness the mass of the electrode cannot be determined and it also makes the determination of pulse lengths, linearity of growth, and the temperature dependency of the films difficult. Luckily, the thickness of the films can also be determined by ellipsometry, which measures the change in the polarization of light upon reflection or transmission. Determination of the thickness of the thicker Li_2TP2A films would allow to inspect if the growth is in reality pure ALD.

The LiTHD was used as the inorganic precursor in all of the depositions, but it is not the most reactive precursor of lithium. The TPA2A and TPA25OH should be experiment with LiHMDS or Li(O^tBu) more reactive lithium precursor, to see if the functional groups could be directly lithiated during the depositions. This could help with the unstable redox kinetics and furthermore could allow the use of TPA25OH as both anode and cathode, if the alcohol groups could be successfully lithiated.

The UV-Vis measurements of the films should be done from thick films and directly in the absorbance mode. The reflectance of the transparent material is low making the Kubelka-Munk transformation less reliable. The band gap measurement of these materials is really important, since it gives indirect information about the HOMO and the LUMO. However, with the four-probe method, electric conductivity and band gap can also be determined and could be compared with optical band gap to verify both results. The exact values of HOMO and the LUMO should also be possible to calculate from CV measurement, with a standard like ferrocene [130]. In addition, some computational methods to directly calculate the energy of LUMO should be looked into.

Protecting the electrode layer with an inert oxide, solid electrolyte layer, or any other coating could drastically improve the stability of the reaction, since the dissolution of the electrode material into the electrolyte might be causing some problems currently. This method already proven to be efficient tactic to improve kinetics [5,131]. In future studies, it is also important to examine if capacity of the cells increases linearly with increasing ALD/MLD cycles and when the electrode utilization decreases.

Atomic force microscope (AFM) studies on the nucleation mechanism of Li_2TP2A, could prove or disprove the island growth model theory. Additionally, AFM could be used to study if there are any morphological changes during the cycling, which could provide valuable additional information.

Since the Li_2TPBr was the most successful as the battery material in terms of capacity and cyclability, the functionalization of organic cathode with bromine should be looked into. Bromine increased the reduction voltage, which is preferable for a cathode material. However, there is still a vast amount of different organic linkers and functional groups that could be experimented on. For example, it would be probably worthwhile to investigate how the electrochemical performance changes when two amino or bromine groups are present instead of one. Also, other groups such as: nitro, thiols, furan, other halides, or even phosphates, could be experimented on and to examine if all these variations could be deposited with ALD/MLD to find new lithium hybrid materials.

REFERENCES

[1] M. Roberts, P. Johns, J. Owen, D. Brandell, K. Edstrom, G. El Enany, C. Guery, D. Golodnitsky, M. Lacey, C. Lecoeur, H. Mazor, E. Peled, E. Perre, M. M. Shaijumon, P. Simon, and P.-L. Taberna, 3D lithium ion batteries—from fundamentals to fabrication, *J. Mater. Chem.* **21** (2011) 9876–9890.

[2] J. L. Souquet, and M. Duclot, Thin film lithium batteries, *Solid State Ionics* **148** (2002) 375–379.

[3] S. K. Cheah, E. Perre, M. Rooth, M. Fondell, A. Hårsta, L. Nyholm, M. Boman, T. Gustafsson, J. Lu, P. Simon, and K. Edström, Self-Supported Three-Dimensional Nanoelectrodes for Microbattery Applications, *Nano Lett.* **9** (2009) 3230–3233.

[4] Z. Song, and H. Zhou, Towards sustainable and versatile energy storage devices: an overview of organic electrode materials, *Energy Environ. Sci.* **6** (2013) 2280–2301.

[5] M. Nisula, and M. Karppinen, Atomic/Molecular Layer Deposition of Lithium Terephthalate Thin Films as High Rate Capability Li-Ion Battery Anodes, *Nano Lett.* **16** (2016) 1276–1281.

[6] M. Armand, S. Grugeon, H. Vezin, S. Laruelle, P. Ribière, P. Poizot, and J.-M. Tarascon, Conjugated dicarboxylate anodes for Li-ion batteries, *Nat. Mater.* **8** (2009) 120–125.

[7] D. C. Bock, A. C. Marschilok, K. J. Takeuchi, and E. S. Takeuchi, Batteries used to power implantable biomedical devices, *Electrochim. Acta* **84** (2012) 155–164.

[8] A. Patil, V. Patil, D. Wook Shin, J.-W. Choi, D.-S. Paik, and S.-J. Yoon, Issue and challenges facing rechargeable thin film lithium batteries, *Mater. Res. Bull.* **43** (2008) 1913–1942.

[9] Y. Wang, B. Liu, Q. Li, S. Cartmell, S. Ferrara, Z. D. Deng, and J. Xiao, Lithium and lithium ion batteries for applications in microelectronic devices: A review, *J. Power Sources* **286** (2015) 330–345.

[10] R. Van Noorden, The rechargeable revolution: A better battery, *Nat. | News Featur.* **507** (2014) 26–28.

[11] M. S. Islam, and C. A. J. Fisher, Lithium and sodium battery cathode materials: computational insights into voltage, diffusion and nanostructural properties, *Chem. Soc. Rev.* **43** (2014) 185–204.

[12] J. F. M. Oudenhoven, L. Baggetto, and P. H. L. Notten, All-solid-state lithium-ion microbatteries: A review of various three-dimensional concepts, *Adv. Energy Mater.* **1** (2011) 10–33.

[13] S. Jones, J. Akridge, and F. Shokoohi, Thin film rechargeable Li batteries, *Solid State Ionics* **69** (1994) 357–368.

[14] Panasonic, Lithium & Micro Batteries Overview, http://industrial.panasonic.com/cdbs/www-data/pdf/AAA4000/AAA4000COL15.pdf, 8.8.2016.

[15] Anonymous, Data Sheet CoinPower ® CP 1654 A2, https://www.texim-europe.com/getfile.aspx?id=109350, 8.8.2016.

[16] J. Kostamo, Picosun's ALD solutions transform battery technology, http://www.picosun.com/sitenews/view/-/nid/145/ngid/4, 10.8.2016.

[17] J. W. Long, B. Dunn, D. R. Rolison, and H. S. White, Three-Dimensional Battery Architectures, *Chem. Rev.* **104** (2004) 4463–4492.

[18] R. W. Hart, H. S. White, B. Dunn, and D. R. Rolison, 3-D Microbatteries, *Electrochem. Commun.* **5** (2003) 120–123.

[19] J. W. Long, and D. R. Rolison, Architectural design, interior decoration, and three-dimensional plumbing en route to multifunctional nanoarchitectures, *Acc. Chem. Res.* **40** (2007) 854–862.

[20] V. R. Mamilla, and K. S. Chakradhar, Micro Machining for Micro Electro Mechanical Systems (MEMS), *Procedia Mater. Sci.* **6** (2014) 1170–1177.

[21] K. Sun, T. S. Wei, B. Y. Ahn, J. Y. Seo, S. J. Dillon, and J. A. Lewis, 3D printing of interdigitated Li-ion microbattery architectures, *Adv. Mater.* **25** (2013) 4539–4543.

[22] E. Perre, L. Nyholm, T. Gustafsson, P.-L. Taberna, P. Simon, and K. Edström, Direct electrodeposition of aluminium nano-rods, *Electrochem. Commun.* **10** (2008) 1467–1470.

[23] S. Leopold, I. . Schuchert, J. Lu, M. . Toimil Molares, M. Herranen, and J.-O. Carlsson, Electrochemical deposition of cylindrical Cu/Cu_2O microstructures, *Electrochim. Acta* **47** (2002) 4393–4397.

[24] C. Mack, Semiconductor Lithography (Photolithography) - The Basic Process, http://www.lithoguru.com/scientist/lithobasics.html, 10.8.2016.

[25] H. Ning, J. H. Pikul, R. Zhang, X. Li, S. Xu, J. Wang, J. A. Rogers, W. P. King, and P. V Braun, Holographic patterning of high-performance on-chip 3D lithium-ion microbatteries, *Proc. Natl. Acad. Sci.* **112** (2015) 6573–6578.

[26] J. H. Pikul, H. Gang Zhang, J. Cho, P. V Braun, and W. P. King, High-power lithium ion microbatteries from interdigitated three-dimensional bicontinuous nanoporous electrodes., *Nat. Commun.* **4** (2013) 1–5.

[27] K. Edström, D. Brandell, T. Gustafsson, and L. Nyholm, Electrodeposition as a Tool for 3D Microbattery Fabrication, *Electrochem. Soc. Interface* (2011) 41–46.

[28] M. Kotobuki, Y. Suzuki, H. Munakata, K. Kanamura, Y. Sato, K. Yamamoto, and T. Yoshida, Fabrication of Three-Dimensional Battery Using Ceramic Electrolyte with Honeycomb Structure by Sol–Gel Process, *J. Electrochem. Soc.* **157** (2010) 493–498.

[29] M. Nathan, D. Golodnitsky, V. Yufit, E. Strauss, T. Ripenbein, I. Shechtman, S. Menkin, and E. Peled, Three-dimensional thin-film Li-ion microbatteries for autonomous MEMS, *J. Microelectromechanical Syst.* **14** (2005) 879–885.

[30] P. H. L. Notten, F. Roozeboom, R. A. H. Niessen, and L. Baggetto, 3-D Integrated All-Solid-State Rechargeable Batteries, *Adv. Mater.* **19** (2007) 4564–4567.

[31] S. Cosnier, and A. Karyakin, *Electropolymerization*, Wiley-VCH Verlag GmbH & Co. KGaA, Weinheim, Germany, 2010.

[32] G. El-Enany, M. J. Lacey, P. A. Johns, and J. R. Owen, In situ growth of

polymer electrolytes on lithium ion electrode surfaces, *Electrochem. Commun.* **11** (2009) 2320–2323.

[33] R. W. Johnson, A. Hultqvist, and S. F. Bent, A brief review of atomic layer deposition: From fundamentals to applications, *Mater. Today* **17** (2014) 236–246.

[34] O. Nilsen, V. Miikkulainen, K. B. Gandrud, E. Østreng, A. Ruud, and H. Fjellvåg, Atomic layer deposition of functional films for Li-ion microbatteries, *Phys. Status Solidi* **211** (2014) 357–367.

[35] P. Sundberg, and M. Karppinen, Organic and inorganic–organic thin film structures by molecular layer deposition: A review, *Beilstein J. Nanotechnol.* **5** (2014) 1104–1136.

[36] A. J. Pearse, T. E. Schmitt, E. J. Fuller, F. El-Gabaly, and A. C. Kozen, Nanoscale Solid State Batteries Enabled By Thermal Atomic Layer Deposition of a Lithium Polyphosphazene Solid State Electrolyte, (2017) 1–31.

[37] E. Quartarone, and P. Mustarelli, Electrolytes for solid-state lithium rechargeable batteries: recent advances and perspectives, *Chem. Soc. Rev.* **40** (2011) 2525–2540.

[38] K. Murata, S. Izuchi, and Y. Yoshihisa, An overview of the research and development of solid polymer electrolyte batteries, *Electrochim. Acta* **45** (2000) 1501–1508.

[39] P. Knauth, Inorganic solid Li ion conductors: An overview, *Solid State Ionics* **180** (2009) 911–916.

[40] Q. Zhao, C. Guo, Y. Lu, L. Liu, J. Liang, and J. Chen, Rechargeable Lithium Batteries with Electrodes of Small Organic Carbonyl Salts and Advanced Electrolytes, *Ind. Eng. Chem. Res.* **55** (2016) 5795–5804.

[41] B. Scrosati, and C. Vincent, Polymer Electrolytes: The Key to Lithium Polymer Batteries, *MRS Bull.* **25** (2000) 28–30.

[42] J. W. Fergus, Ceramic and polymeric solid electrolytes for lithium-ion batteries, *J. Power Sources* **195** (2010) 4554–4569.

[43] L. Z. Fan, X. L. Wang, F. Long, and X. Wang, Enhanced ionic conductivities in composite polymer electrolytes by using succinonitrile as a plasticizer, *Solid State Ionics* **179** (2008) 1772–1775.

[44] S. Y. An, I. C. Jeong, M.-S. Won, E. D. Jeong, and Y.-B. Shim, Effect of additives in PEO/PAA/PMAA composite solid polymer electrolytes on the ionic conductivity and Li ion battery performance, *J. Appl. Electrochem.* **39** (2009) 1573–1578.

[45] H. M. J. C. Pitawala, M. A. K. L. Dissanayake, V. A. Seneviratne, B.-E. Mellander, and I. Albinson, Effect of plasticizers (EC or PC) on the ionic conductivity and thermal properties of the $(PEO)_9LiTf$: Al_2O_3 nanocomposite polymer electrolyte system, *J. Solid State Electrochem.* **12** (2008) 783–789.

[46] F. Croce, L. Persi, B. Scrosati, F. Serraino-Fiory, E. Plichta, and M. Hendrickson, Role of the ceramic fillers in enhancing the transport properties of composite polymer electrolytes, *Electrochim. Acta* **46** (2001) 2457–2461.

[47] D. Golodnitsky, Effect of plasticizers on the CPE conductivity and on the Li-CPE interface, *Solid State Ionics* **85** (1996) 231–238.

[48] C.-W. Nan, L. Fan, Y. Lin, and Q. Cai, Enhanced Ionic Conductivity of Polymer Electrolytes Containing Nanocomposite SiO_2 Particles, *Phys. Rev. Lett.* **91** (2003) 1–4.

[49] H. Y. Sun, Y. Takeda, N. Imanishi, O. Yamamoto, and H.-J. Sohn, Ferroelectric Materials as a Ceramic Filler in Solid Composite Polyethylene Oxide-Based Electrolytes, *J. Electrochem. Soc.* **147** (2000) 2462–2467.

[50] A. Manuel Stephan, and K. S. Nahm, Review on composite polymer electrolytes for lithium batteries, *Polymer (Guildf).* **47** (2006) 5952–5964.

[51] Y.-J. Wang, Y. Pan, and D. Kim, Conductivity studies on ceramic $Li_{1.3}Al_{0.3}Ti_{1.7}(PO_4)_3$-filled PEO-based solid composite polymer electrolytes, *J. Power Sources* **159** (2006) 690–701.

[52] F. Croce, L. Persi, F. Ronci, and B. Scrosati, Nanocomposite polymer electrolytes and their impact on the lithium battery technology, *Solid State Ionics* **135** (2000) 47–52.

[53] W. Liu, N. Liu, J. Sun, P.-C. Hsu, Y. Li, H.-W. Lee, and Y. Cui, Ionic Conductivity Enhancement of Polymer Electrolytes with Ceramic Nanowire Fillers, *Nano Lett.* **15** (2015) 2740–2745.

[54] W.-K. Shin, J. Cho, A. G. Kannan, Y.-S. Lee, and D.-W. Kim, Cross-linked Composite Gel Polymer Electrolyte using Mesoporous Methacrylate-Functionalized SiO_2 Nanoparticles for Lithium-Ion Polymer Batteries, *Sci. Rep.* **6** (2016) 1–10.

[55] C. W. Kuo, W. Bin Li, P. R. Chen, J. W. Liao, C. G. Tseng, and T. Y. Wu, Effect of plasticizer and lithium salt concentration in PMMA-based composite polymer electrolytes, *Int. J. Electrochem. Sci.* **8** (2013) 5007–5021.

[56] J. Zhang, B. Sun, X. Huang, S. Chen, and G. Wang, Honeycomb-like porous gel polymer electrolyte membrane for lithium ion batteries with enhanced safety, *Sci. Rep.* **4** (2014) 1–7.

[57] R. C. Agrawal, and G. P. Pandey, Solid polymer electrolytes: materials designing and all-solid-state battery applications: an overview, *J. Phys. D. Appl. Phys.* **41** (2008) 1–18.

[58] K.-S. Liao, T. E. Sutto, E. Andreoli, P. Ajayan, K. A. McGrady, and S. A. Curran, Nano-sponge ionic liquid–polymer composite electrolytes for solid-state lithium power sources, *J. Power Sources* **195** (2010) 867–871.

[59] K. Ghandi, A Review of Ionic Liquids, Their Limits and Applications, *Green Sustain. Chem.* **4** (2014) 44–53.

[60] R. Zhang, Y. Chen, and R. Montazami, Ionic Liquid-Doped Gel Polymer Electrolyte for Flexible Lithium-Ion Polymer Batteries, *Materials (Basel).* **8** (2015) 2735–2748.

[61] K. Matsumoto, S. Sogabe, and T. Endo, Conductive networked polymer gel electrolytes composed of poly(meth)acrylate, lithium salt, and ionic liquid, *J. Polym. Sci. Part A Polym. Chem.* **50** (2012) 1317–1324.

[62] V. Thangadurai, and W. Weppner, Recent progress in solid oxide and lithium ion conducting electrolytes research, *Ionics (Kiel).* **12** (2006) 81–92.

[63] J. C. Bachman, S. Muy, A. Grimaud, H.-H. Chang, N. Pour, S. F. Lux, O.

Paschos, F. Maglia, S. Lupart, P. Lamp, L. Giordano, and Y. Shao-Horn, Inorganic Solid-State Electrolytes for Lithium Batteries: Mechanisms and Properties Governing Ion Conduction, *Chem. Rev.* **116** (2016) 140–162.

[64] Y. Kobayashi, M. Tabuchi, and O. Nakamura, Ionic conductivity enhancement in $LiTi_2(PO_4)_3$-based composite electrolyte by the addition of lithium nitrate, *J. Power Sources* **68** (1997) 407–411.

[65] M. Zhang, K. Takahashi, N. Imanishi, Y. Takeda, O. Yamamoto, B. Chi, J. Pu, and J. Li, Preparation and Electrochemical Properties of $Li_{1+x}Al_xGe_{2-x}(PO_4)_3$ Synthesized by a Sol-Gel Method, *J. Electrochem. Soc.* **159** (2012) 1114–1119.

[66] V. Thangadurai, S. Narayanan, and D. Pinzaru, Garnet-type solid-state fast Li ion conductors for Li batteries: critical review., *Chem. Soc. Rev.* **43** (2014) 4714–4727.

[67] C. Deviannapoorani, L. Dhivya, S. Ramakumar, and R. Murugan, Lithium ion transport properties of high conductive tellurium substituted $Li_7La_3Zr_2O_{12}$ cubic lithium garnets, *J. Power Sources* **240** (2013) 18–25.

[68] N. Kamaya, K. Homma, Y. Yamakawa, M. Hirayama, R. Kanno, M. Yonemura, T. Kamiyama, Y. Kato, S. Hama, K. Kawamoto, and A. Mitsui, A lithium superionic conductor, *Nat. Mater.* **10** (2011) 682–686.

[69] E. Rangasamy, Z. Liu, M. Gobet, K. Pilar, G. Sahu, W. Zhou, H. Wu, S. Greenbaum, and C. Liang, An Iodide-Based $Li_7P_2S_8I$ Superionic Conductor, *J. Am. Chem. Soc.* **137** (2015) 1384–1387.

[70] G. Sahu, E. Rangasamy, J. Li, Y. Chen, K. An, N. Dudney, and C. Liang, A high-conduction Ge substituted Li_3AsS_4 solid electrolyte with exceptional low activation energy, *J. Mater. Chem. A* **2** (2014) 10396–10403.

[71] Y. Seino, T. Ota, K. Takada, A. Hayashi, and M. Tatsumisago, A sulphide lithium super ion conductor is superior to liquid ion conductors for use in rechargeable batteries, *Energy Environ. Sci.* **7** (2014) 627–631.

[72] Y. Kato, S. Hori, T. Saito, K. Suzuki, M. Hirayama, A. Mitsui, M. Yonemura, H. Iba, and R. Kanno, High-power all-solid-state batteries using sulfide superionic conductors, *Nat. Energy* **1** (2016) 1–7.

[73] S. Zhao, Z. Fu, and Q. Qin, A solid-state electrolyte lithium phosphorus oxynitride film prepared by pulsed laser deposition, *Thin Solid Films* **415** (2002) 108–113.

[74] H. T. Kim, T. Mun, C. Park, S. W. Jin, and H. Y. Park, Characteristics of lithium phosphorous oxynitride thin films deposited by metal-organic chemical vapor deposition technique, *J. Power Sources* **244** (2013) 641–645.

[75] A. C. Kozen, A. J. Pearse, C.-F. Lin, M. Noked, and G. W. Rubloff, Atomic Layer Deposition of the Solid Electrolyte LiPON, *Chem. Mater.* **27** (2015) 5324–5331.

[76] M. Nisula, Y. Shindo, H. Koga, and M. Karppinen, Atomic Layer Deposition of Lithium Phosphorus Oxynitride, *Chem. Mater.* **27** (2015) 6987–6993.

[77] S. Shibata, Thermal Atomic Layer Deposition of Lithium Phosphorus Oxynitride as a Thin-Film Solid Electrolyte, *J. Electrochem. Soc.* **163** (2016) 2555–2562.

[78] B. Fleutot, B. Pecquenard, F. Le Cras, B. Delis, H. Martinez, L. Dupont, and D. Guy-Bouyssou, Characterization of all-solid-state Li/LiPONB/TiOS microbatteries produced at the pilot scale, *J. Power Sources* **196** (2011) 10289–10296.

[79] X. Yu, A Stable Thin-Film Lithium Electrolyte: Lithium Phosphorus Oxynitride, *J. Electrochem. Soc.* **144** (1997) 524–532.

[80] S. Zugmann, M. Fleischmann, M. Amereller, R. M. Gschwind, H. D. Wiemhöfer, and H. J. Gores, Measurement of transference numbers for lithium ion electrolytes via four different methods, a comparative study, *Electrochim. Acta* **56** (2011) 3926–3933.

[81] L. Porcarelli, C. Gerbaldi, F. Bella, and J. R. Nair, Super Soft All-Ethylene Oxide Polymer Electrolyte for Safe All-Solid Lithium Batteries, *Sci. Rep.* **6** (2016) 1–14.

[82] L. O. Valøen, and J. N. Reimers, Transport Properties of $LiPF_6$-Based Li-Ion Battery Electrolytes, *J. Electrochem. Soc.* **152** (2005) 882–891.

[83] Q. Guo, Y. Han, H. Wang, X. Hong, C. Zheng, S. Liu, and K. Xie, Safer lithium

metal battery based on advanced ionic liquid gel polymer nonflammable electrolytes, *RSC Adv.* **6** (2016) 101638–101644.

[84] H. Aono, Ionic Conductivity of Solid Electrolytes Based on Lithium Titanium Phosphate, *J. Electrochem. Soc.* **137** (1990) 1023–1027.

[85] L. Le Van-Jodin, F. Ducroquet, F. Sabary, and I. Chevalier, Dielectric properties, conductivity and Li^+ ion motion in LiPON thin films, *Solid State Ionics* **253** (2013) 151–156.

[86] W. G. Zeier, and J. Janek, A solid future for battery development, *Nat. Energy* **1** (2016) 1–4.

[87] T. B. Schon, B. T. McAllister, P.-F. Li, and D. S. Seferos, The rise of organic electrode materials for energy storage, *Chem. Soc. Rev.* **45** (2016) 6345–6404.

[88] J. J. Byrne, J. S. Driscoll, and D. L. Williams, A high energy density lithium/ dichloroisocyanuric acid battery system., *Electrochem. Sci.* **116** (1969) 3–5.

[89] Z. Zhu, and J. Chen, Review—Advanced Carbon-Supported Organic Electrode Materials for Lithium (Sodium)-Ion Batteries, *J. Electrochem. Soc.* **162** (2015) 2393–2405.

[90] B. Häupler, A. Wild, and U. S. Schubert, Carbonyls: Powerful Organic Materials for Secondary Batteries, *Adv. Energy Mater.* **5** (2015) 1402034.

[91] Y. Liang, Z. Tao, and J. Chen, Organic electrode materials for rechargeable lithium batteries, *Adv. Energy Mater.* **2** (2012) 742–769.

[92] J. Xie, and Q. Zhang, Recent progress in rechargeable lithium batteries with organic materials as promising electrodes, *J. Mater. Chem. A* **4** (2016) 7091–7106.

[93] M. Miroshnikov, K. P. Divya, G. Babu, A. Meiyazhagan, L. Mohana, R. Arava, P. M. Ajayan, and G. John, Power from nature: designing green battery materials from electroactive quinone derivatives and organic polymers, *J. Mater. Chem. A Mater. Energy Sustain.* **4** (2016) 12370–12386.

[94] H. Chen, M. Armand, M. Courty, M. Jiang, C. P. Grey, F. Dolhem, J.-M. Tarascon, and P. Poizot, Lithium Salt of Tetrahydroxybenzoquinone: Toward

the Development of a Sustainable Li-Ion Battery, *J. Am. Chem. Soc.* **131** (2009) 8984–8988.

[95] M. Solà, Forty years of Clar's aromatic π-sextet rule, *Front. Chem.* **1** (2013) 4–11.

[96] D. Wu, Z. Xie, Z. Zhou, P. Shen, and Z. Chen, Designing high-voltage carbonyl-containing polycyclic aromatic hydrocarbon cathode materials for Li-ion batteries guided by Clar's theory, *J. Mater. Chem. A* **3** (2015) 19137–19143.

[97] K. Hernández-Burgos, S. E. Burkhardt, G. G. Rodríguez-Calero, R. G. Hennig, and H. D. Abruña, Theoretical Studies of Carbonyl-Based Organic Molecules for Energy Storage Applications: The Heteroatom and Substituent Effect, *J. Phys. Chem. C* **118** (2014) 6046–6051.

[98] S. Gottis, A.-L. Barrès, F. Dolhem, and P. Poizot, Voltage Gain in Lithiated Enolate-Based Organic Cathode Materials by Isomeric Effect, *ACS Appl. Mater. Interfaces* **6** (2014) 10870–10876.

[99] Y. Liang, P. Zhang, S. Yang, Z. Tao, and J. Chen, Fused heteroaromatic organic compounds for high-power electrodes of rechargeable lithium batteries, *Adv. Energy Mater.* **3** (2013) 600–605.

[100] Y. Park, D. S. Shin, S. H. Woo, N. S. Choi, K. H. Shin, S. M. Oh, K. T. Lee, and S. Y. Hong, Sodium terephthalate as an organic anode material for sodium ion batteries, *Adv. Mater.* **24** (2012) 3562–3567.

[101] J. Lee, H. Kim, and M. J. Park, Long-Life, High-Rate Lithium-Organic Batteries Based on Naphthoquinone Derivatives, *Chem. Mater.* **28** (2016) 2408–2416.

[102] Y. Zhang, J. Wang, and S. N. Riduan, Strategies toward improving the performance of organic electrodes in rechargeable lithium (sodium) batteries, *J. Mater. Chem. A* **4** (2016) 14902–14914.

[103] W. Wan, H. Lee, X. Yu, C. Wang, K.-W. Nam, X.-Q. Yang, and H. Zhou, Tuning the electrochemical performances of anthraquinone organic cathode materials for Li-ion batteries through the sulfonic sodium functional group, *RSC Adv.* **4** (2014) 19878–19882.

[104] Y. Liang, P. Zhang, and J. Chen, Function-oriented design of conjugated carbonyl compound electrodes for high energy lithium batteries, *Chem. Sci.* **4** (2013) 1330–1337.

[105] Y. Y. Zhang, Y. Y. Sun, S. X. Du, H.-J. Gao, and S. B. Zhang, Organic salts as super-high rate capability materials for lithium-ion batteries, *Appl. Phys. Lett.* **100** (2012) 1–4.

[106] M. A. Sk, and S. Manzhos, Exploring the sodium storage mechanism in disodium terephthalate as anode for organic battery using density-functional theory calculations, *J. Power Sources* **324** (2016) 572–581.

[107] X. Wu, S. Jin, Z. Zhang, L. Jiang, L. Mu, Y.-S. Hu, H. Li, X. Chen, M. Armand, L. Chen, and X. Huang, Unraveling the storage mechanism in organic carbonyl electrodes for sodium-ion batteries, *Sci. Adv.* **1** (2015) 1–9.

[108] H. H. Lee, Y. Park, K. H. Shin, K. T. Lee, and S. Y. Hong, Abnormal excess capacity of conjugated dicarboxylates in lithium-ion batteries, *ACS Appl. Mater. Interfaces* **6** (2014) 19118–19126.

[109] S. Renault, V. A. Oltean, C. M. Araujo, A. Grigoriev, K. Edström, and D. Brandell, Superlithiation of Organic Electrode Materials: The Case of Dilithium Benzenedipropiolate, *Chem. Mater.* **28** (2016) 1920–1926.

[110] W. Luo, M. Allen, V. Raju, and X. Ji, An Organic Pigment as a High-Performance Cathode for Sodium-Ion Batteries, *Adv. Energy Mater.* **4** (2014) 1–5.

[111] X. Han, G. Qing, J. Sun, and T. Sun, How Many Lithium Ions Can Be Inserted onto Fused C_6 Aromatic Ring Systems?, *Angew. Chemie Int. Ed.* **51** (2012) 5147–5151.

[112] D. Larcher, and J.-M. Tarascon, Towards greener and more sustainable batteries for electrical energy storage, *Nat. Chem.* **7** (2014) 19–29.

[113] M. Armand, and J.-M. Tarascon, Building better batteries, *Nature* **451** (2008) 652–657.

[114] L. Gaines, The future of automotive lithium-ion battery recycling: Charting a sustainable course, *Sustain. Mater. Technol.* **1–2** (2014) 2–7.

[115] J. B. Dunn, L. Gaines, M. Barnes, M. Wang, and J. Sullivan, *Material and energy flows in the materials production, assembly, and end-of-life stages of the automotive lithium-ion battery life cycle*, Argonne National Laboratory, Argonne, IL (United States), 2012.

[116] E. Gratz, Q. Sa, D. Apelian, and Y. Wang, A closed loop process for recycling spent lithium ion batteries, *J. Power Sources* **262** (2014) 255–262.

[117] P. Poizot, and F. Dolhem, Clean energy new deal for a sustainable world: from non-CO_2 generating energy sources to greener electrochemical storage devices, *Energy Environ. Sci.* **4** (2011) 2003–2019.

[118] P. W. Gruber, P. A. Medina, G. A. Keoleian, S. E. Kesler, M. P. Everson, and T. J. Wallington, Global Lithium Availability, *J. Ind. Ecol.* **15** (2011) 760–775.

[119] V.-A. Oltean, S. Renault, M. Valvo, and D. Brandell, Sustainable Materials for Sustainable Energy Storage: Organic Na Electrodes, *Materials (Basel)*. **9** (2016) 1–27.

[120] R. Mohtadi, and F. Mizuno, Magnesium batteries: Current state of the art, issues and future perspectives, *Beilstein J. Nanotechnol.* **5** (2014) 1291–1311.

[121] M.-C. Lin, M. Gong, B. Lu, Y. Wu, D.-Y. Wang, M. Guan, M. Angell, C. Chen, J. Yang, B.-J. Hwang, and H. Dai, An ultrafast rechargeable aluminium-ion battery, *Nature* **520** (2015) 324–328.

[122] S. Renault, D. Brandell, and K. Edström, Environmentally-Friendly Lithium Recycling From a Spent Organic Li-Ion Battery, *ChemSusChem* **7** (2014) 2859–2867.

[123] C. W. Glass, A. R. Oganov, and N. Hansen, USPEX-Evolutionary crystal structure prediction, *Comput. Phys. Commun.* **175** (2006) 713–720.

[124] K. B. Klepper, O. Nilsen, and H. Fjellvag, Deposition of thin films of organic-inorganic hybrid materials based on aromatic carboxylic acids by atomic layer deposition, *Dalt. Trans.* **39** (2010) 11628–11635.

[125] J. Wilbuer, D. C. Grenz, G. Schnakenburg, and B. Esser, Donor- and acceptor-functionalized dibenzo[a,e]pentalenes: modulation of the electronic band gap, *Org. Chem. Front.* (2017) 1–6.

[126] H.-S. Kim, C.-R. Lee, J.-H. Im, K.-B. Lee, T. Moehl, A. Marchioro, S.-J. Moon, R. Humphry-Baker, J.-H. Yum, J. E. Moser, M. Grätzel, and N.-G. Park, Lead iodide perovskite sensitized all-solid-state submicron thin film mesoscopic solar cell with efficiency exceeding 9%, *Sci. Rep.* **2** (2012) 1–7.

[127] F. Scholz, *Electroanalytical methods: Guide to experiments and applications*, 2010.

[128] J. Rodriguez-Carvajal, PHYSICA Recent advances in magnetic structure determination neutron powder diffraction, *Phys. B* **192** (1993) 55–69.

[129] Q. Deng, J. Xue, W. Zou, L. Wang, A. Zhou, and J. Li, The electrochemical behaviors of $Li_2C_8H_4O_6$ and its corresponding organic acid $C_8H_6O_6$ as anodes for Li-ion batteries, *J. Electroanal. Chem.* **761** (2016) 74–79.

[130] L. Leonat, G. Sb, I. V. Br, and I. Cyclic, Cyclic Voltammetry for Energy Levels Estimation of Organic Materials, *U.P.B.Sci.Bull., Ser. B* **75** (2013) 111–118.

[131] X. Li, A. Lushington, Q. Sun, W. Xiao, J. Liu, B. Wang, Y. Ye, K. Nie, Y. Hu, Q. Xiao, R. Li, J. Guo, T. K. Sham, and X. Sun, Safe and Durable High-Temperature Lithium-Sulfur Batteries via Molecular Layer Deposited Coating, *Nano Lett.* **16** (2016) 3545–3549.